Dipartimento di Scienze Fisiche, della Terra e dell'Ambiente

Dottorato in Fisica Sperimentale

36° Ciclo

Coordinatore: Prof. Riccardo Paoletti

Study, Development and Optimization of Laser Resonant Photo-Ionization processes applied to species of interest for the Isolpharm-SPES project

Settore scientifico disciplinare: FIS/01

Candidato:
Omorjit Singh Khwairakpam

Firmato da
Omorjit Singh
Khwairakpam
IT
in data
10-10-2023

Tutore:
Prof. Emilio Mariotti

Co-tutore:
Ing. Daniele Scarpa

Anno accademico del conseguimento del titolo di Dottore di ricerca
2022-2023

Università degli Studi di Siena
Dottorato FIS/01
36° **Ciclo**

Data dell'esame finale
23/10/2023

Abstract

The principle of resonance laser photo-ionization is used to selectively ionize elements of interest in isotope separation online (ISOL) facilities. The work presents the study of two-step resonance photo-ionization of silver atoms in the context of selective production of exotic species (SPES) at INFN-LNL. Using a hot ablation plume of silver atoms in a time of flight mass spectrometer (TOF-MS), Doppler-suppressed and Doppler-broadened resonance frequency profile of the transition steps. It is shown that a Doppler-suppressed resonance profile can be achieved in a two-step resonant transition by introducing an angular separation as low as 8.5° between the two resonant laser beams. In the case of collinear injection of these laser beams, Doppler broadening is observed and the effect of the laser linewidth in a Doppler-broadened resonance profile is also studied.

A silver hollow cathode lamp has also been used to study the same resonant transitions. Two kinds of opto-galvanic signals i.e. slow signal and fast signal are used to detect the resonance in this case. Using the hollow cathode lamp, strong evidence of high-lying Rydberg states of silver around the energy value of 7.56 eV (60945.32 cm^{-1}).

First-time characterization of the SPES laser ion source (LIS) at ISOLDE Offline 2 is also presented. The SPES-LIS is a hot tubular tantalum cavity inside which laser beams with frequencies tuned to the electronic transitions of particular elements are made to interact with the vapor of the element. Important parameters such as thermal stability of the ion source, time structure of the ion beam, laser enhancement of the ion yield, and resonance laser ionization efficiency have been measured in relation to the production of the gallium ion beam. The effect of the electrostatic axial field on the movement of the ions along the length of the ion source is discussed. The dependence of the laser enhancement of the ion yield on the ion source temperature and the total ion current has been studied too. At a high ion source temperature of 2200°C, the laser enhancement of the ion yield at different total ion currents is found relatively stable compared to lower ion source temperatures.

A new TOF-MS has been designed and assembled in the online laser lab at the SPES facility. Two independent sources of atomic beam viz. an effusion cell and an ablation target system, are employed in the system. This new TOF-MS should aid in scheme developments for the photo-ionization of several elements and also provide the geometry for high-resolution laser resonant spectrometry.

Acknowledgement

This work has been possible thanks to the various forms of support I received before and during my PhD period.

I would like to start by thanking my family who supported and made it easy for me to start my journey to Europe 6 years ago. I would like to thank my friends and loved ones for being present at every turn which directly or indirectly influences my mental health and attitude towards things in general. I also take time to show my gratitude to all those strangers who shared a fraction of their life with me and showed me that life is something to be shared.

My supervisors Prof. Emilio Mariotti and Ing. Daniele Scarpa have been an immense support during the course of this work. They have shown me that it takes more than just being knowledgeful to groom a young mind. They have been present on a personal level and have always encouraged me wherever is required. I would also like to thank Dr. Alen Khanbekyan who has guided me and shared his experience with me in the initial phase of my work. I am very grateful towards Prof. Piergiorgio Nicolosi who has always provided very important insights to details during the experiments and data interpretation. The work on the designing of the new time of flight mass spectrometer could be fulfilled in the desired way thanks to the valuable help offered by Dr. Massimo Rossignoli.

I would like to extend my gratitude to the Department DSFTA of University of Siena and the SPES project of INFN-LNL for having supported me and provided me the opportunity to contribute to this research field. My gratitude also extends to my colleagues and friends at work who have created a professional and respectful environment in the work place. I am also very thankful to the security staff, the cleaning staff and the canteen staff at INFN-LNL. Their dedication and effort have kept the laboratory and its working members sound and healthy.

The period I have spent at CERN within the RILIS team in ISOLDE brought a lot of positive aspects to my research life. I am grateful to the whole RILIS team for taking time to include me in their work group and trusting me with certain responsibilities over the time. I express particular gratefulness towards

Dr. Valentin Fedosseev and Dr. Bruce Marsh for agreeing to have me in the RILIS team for more than 3 months and integrating me into the group from day one.

During the course of this PhD, severe hindrances were brought upon by the pandemic of Covid-19 on a personal and professional level. I express my condolences to everyone, known and unknown to me, for the loss they have suffered and the struggle they have endured.

Last but not the least, I would like to mention that as every other journey in life, there were ups and downs during the course of this PhD too. The important thing is to keep the hope alive, be grateful for the good things and believe in yourself.

It is more important to be a good person than to be "successful" in life.

Contents

List of Figures

List of Tables

Chapter 1

Introduction

Since the early days of quantum mechanics, understanding the behavior of atoms and their interaction with photons has been pivotal in shaping our comprehension of the fundamental principles governing the universe. Laser spectroscopy, as a powerful investigative method, has enabled researchers to probe the electronic, vibrational, and rotational states of atoms and ions with remarkable precision. By exploiting the unique properties of lasers, such as tunability, narrow line widths, and coherence, scientists have unlocked a plethora of opportunities to explore the characteristics and behavior of elements across the periodic table.

The primary objective of this thesis is to explore the intricacies of laser spectroscopy techniques employed for the study of photo-ionization processes in different elements. The process of photo-ionization, whereby an atom or ion absorbs photons and subsequently becomes ionized, plays a vital role in a myriad of scientific fields, from astrophysics to plasma physics, from atomic and molecular physics to environmental monitoring.

The thesis will encompass both theoretical foundations and experimental methodologies, providing a comprehensive overview of the principles governing laser-matter interactions and the analytical tools used to interpret the data. The initial chapters will lay the groundwork by introducing fundamental concepts and theoretical frameworks. Subsequent sections will delve into the experimental setup, techniques employed, and data analysis procedures.

During the course of this Ph.D., I have performed several works which include 1) a two-step resonant laser photo-ionization of silver atoms in an atomic ablation plume using a Time of Flight Mass Spectrometer (TOF-MS), 2) a study of opto-galvanic effect in a silver hollow cathode lamp via resonant excitations, 3) study and characterization of a laser ion source for Selective Production of Exotic Species (SPES) project [1] performed at CERN, and 4) designing and assembly

of a new TOF-MS for higher resolution laser spectroscopy.

The resonance photo-ionization study of silver in an ablation plume provides a detailed description of how the Doppler Broadening affects a resonance profile in a hot environment such as an ablation plume, and how this effect can be suppressed by carefully manipulating the interaction volume of the multiple laser beams and the atomic vapor. The effect of the linewidth of the laser profile on the total broadening of the resonance profile was also studied, by altering the pumping power of the dye lasers. A qualitative study on the transition probabilities from the state $4d^{10}5p\,^2P^o_{3/2}$ to the fine structure levels of $4d^{10}6d\,^2D$ (J=5/2 and J=3/2) of silver was also performed.

The analysis of the slow and fast opto-galvanic signals from the silver hollow cathode lamp, when resonant laser beams are introduced, provided strong evidence of a collection of high-lying Rydberg states of silver. These states are observed around the energy value of 7.56 eV, very close to the ionization potential of silver which is 7.58 eV. However, these states are yet to be identified.

In the SPES project at INFN-LNL, tubular hot cavities shined with resonant laser beams, also called laser ion sources, will be used to produce chemically pure ion beams. I have performed the characterization of the laser beam source in relation to the production of gallium ion beams at ISOLDE Offline 2, CERN. During this study, very important and significant results on ion beam time structure, laser enhancement of ion yields, and resonance laser ionization efficiency have been achieved. The influence of the electrostatic axial field on the movement of ions inside a resistivity-heated tubular hot cavity and transfer line has been quantitatively discussed. The effect of the total ion current, due to surface ionized species, on the selectivity or laser enhancement of the ion yield in the laser ion source has been investigated. The resonance laser ionization efficiency measurement of gallium in the SPES laser ion source resulted in a value of 27.2% which is indeed very satisfactory. This test was the first-time characterization of the SPES laser ion source and will serve as a benchmark for future activities.

Last, but not the least, I have designed and assembled a new TOF-MS in the online laser lab in the SPES facility. Several upgrades have been implemented in the new TOF with respect to the one already present in the offline laser lab. This new TOF-MS has been designed taking into account the possibility of a higher resolution laser spectroscopy, and an additional atom source which is an effusion cell. Several entry points for the entrance of the resonant laser beams are provided to provide an orthogonal intersection of the laser beams and the atomic beam to achieve Doppler-free spectroscopy.

Chapter 2

Motivation

SPES project

One of the most significant technological advancements in the last 30 years for interdisciplinary study in nuclear physics has been the development of radioactive ion beam (RIB) facilities [2]. Both the design of specialized facilities and the renovation of pre-existing machinery have been used to realize the development of new large infrastructures.

RIBs have already given researchers access to study opportunities that would not have been possible with stable elements. With the availability of RIBs, it is now possible to: (1) gain a deeper understanding of the characteristics of nuclei dating back to the time of their formation in the early universe [3]; (2) explore nuclear reactions outside of the stability region, which is crucial to stellar nucleosynthesis [4]; (3) ascertain the behavior of many-body systems [5].

The project "Selective Production of Exotic Species" (SPES) at Legnaro INFN Laboratory is dedicated to the creation and installation of a second-generation Isotope Separation On-Line (ISOL) facility. It is currently in the last stage of the construction process. The facility will use target material such as uranium carbide (UC_x). When it is bombarded by a primary proton beam (I=200 μA and E= 40 MeV), radioactive neutron-rich nuclei, in the mass range of 80-160 amu, will be produced with a predicted fission rate of 10^{13}/s [1].

Other target materials, including silicon carbide, which are currently being developed, will be used to produce neutron-deficient beams. The generated beams will be utilized for research in fundamental nuclear physics as well as for a variety of other purposes, such as the creation of radionuclides with potential medical uses and the production of neutrons for use in material science, nuclear technology, and medicine.

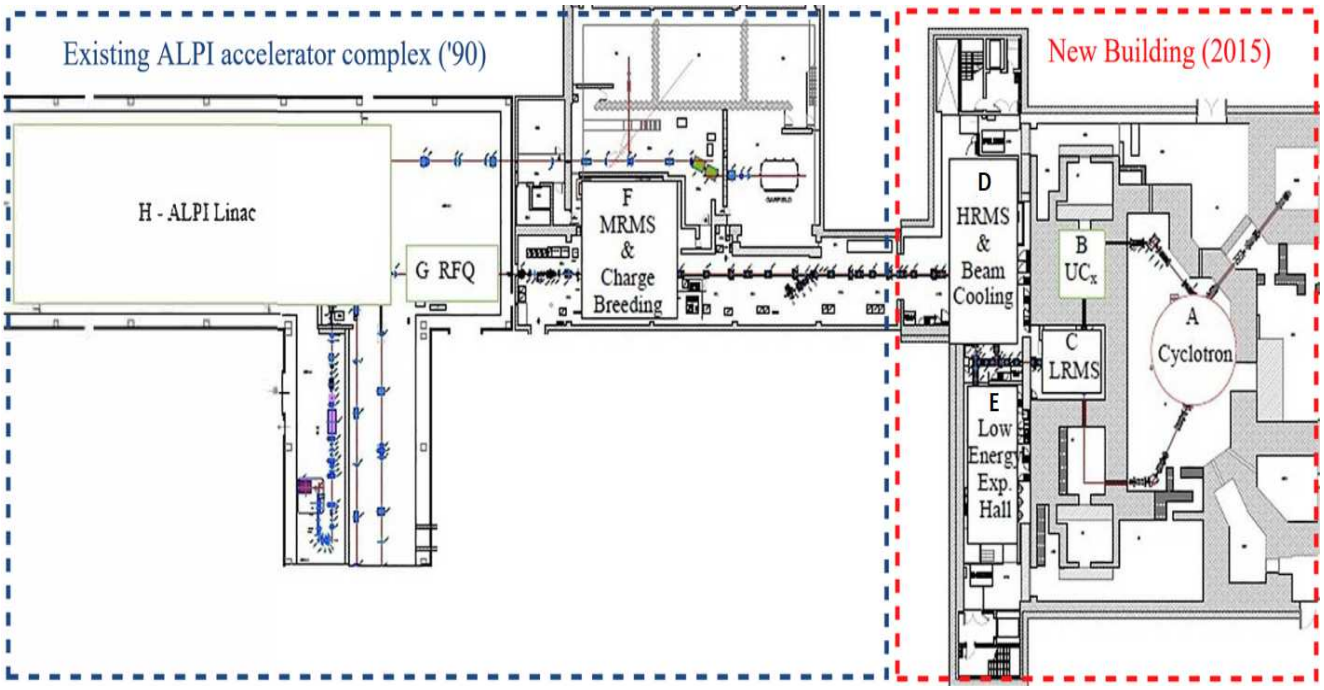

Figure 2.1: Layout of the SPES facility: A-cyclotron, B-UC_x production target bunker, C-Low Resolution Mass Separator (LRMS), D- beam cooling and High-Resolution Mass Separator (HRMS), E- Experimental hall for low energy (up to 40 keV) experiments, F-charge breeding and Medium Resolution Mass Separator (MRMS), G-RFQ, and H-ALPI linac.

Figure 2.1 shows the general layout of the SPES ISOL facility [1]. The driver cyclotron [A] releases a primary proton beam with energy ranging from 35 to 70 MeV (up to 70 kW of power). The beam is sent to the RIB production bunker, where nuclear reactions take place in the installed production target in the front-end apparatus [B]. The front end has all the equipment required for ionizing the desired element and the initial acceleration of the ion beam, and a Wien filter is used to perform the first mass separation of the generated species.

After being bent using the 90° magnet analyzer, LRMS: Low-Resolution Mass Separator [C], and passing through a variety of electrostatic devices, including electrostatic quadrupole triplets, electrostatic dipoles, and steerers, the obtained low energy (up to 40 keV) isobaric beam is then injected into a beam cooler, a device that can reduce the transverse and longitudinal beam emittance. The LRMS is also used as the entry point for the laser beam. The online laser laboratory is located on the first floor of the structure directly above the LRMS hall, shown in Figure 2.6.

A High-Resolution Mass Separator (HRMS) [D] is used to complete the second step of beam purification. The generated isotopically pure RIB can be sent

directly to users for low-energy experiments [E]. It could also be put into a charge breeder, a device designed to increase the beam charge state, and Medium Resolution Mass Separator (MRMS) [F]. The ALPI Linac and Radio Frequency Quadrupole (RFQ) [G] will be coupled to execute the post-acceleration [H]. Finally, a beam that is both isotopically pure and highly energetic (up to 40 MeV) may be delivered to the experimental area for high-energy nuclear physics investigations.

2.1 Front End/Target Ion Source (TIS)

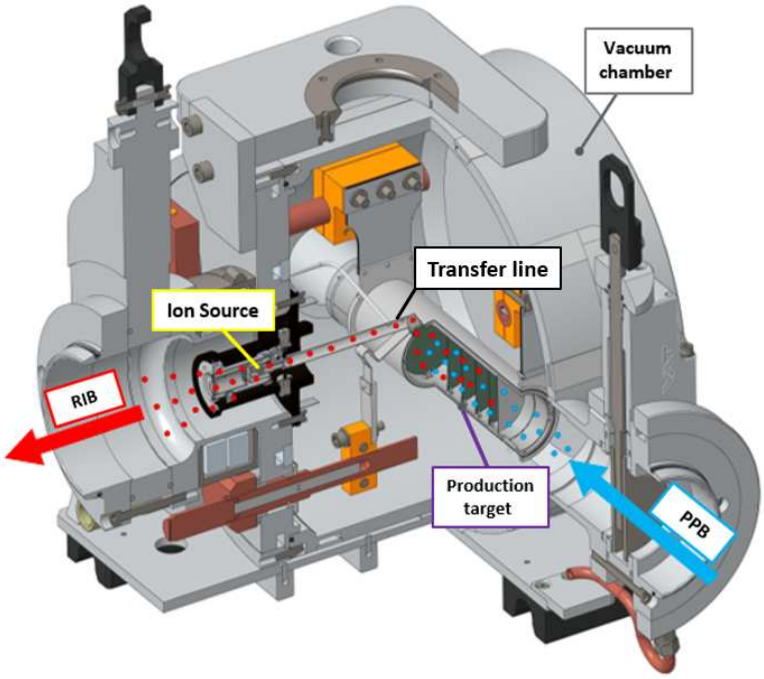

Figure 2.2: A detailed view of the SPES Front End. PPB and RIB represent the primary proton beam and radioactive ion beam respectively.

The Front end is undoubtedly one of the most important entities of the SPES facility. It consists primarily of the target, transfer line, and ion source. As clearly shown in Figure 2.2, the primary proton beam (PPB), around 40 MeV, is irradiated on the production target. This process produces hundreds of isotopes, stable and exotic, as a result of nuclear fission reaction as schematically presented in Figure 2.3.

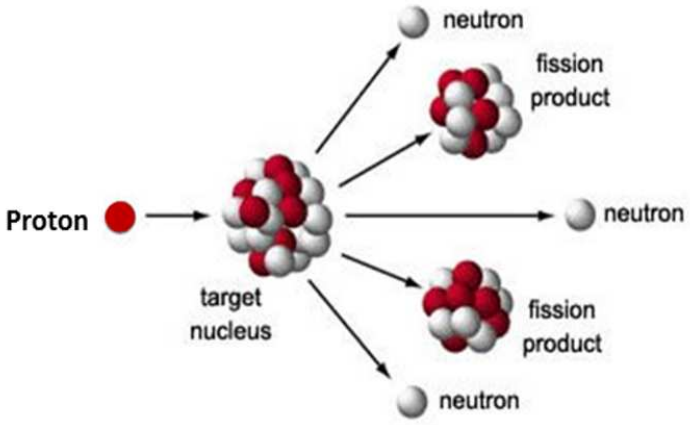

Figure 2.3: A schematic representation of the reaction happening inside the target, when irradiated by a proton beam.

These products diffuse and effuse through the target, which is maintained at a temperature of about 2000°C, to arrive at the ion source. The rapidity of this transport is dependent on the temperature and the material property of the target. Other factors that greatly influence the path length of these species to reach the ion source are the porosity or the grain structure of the target and the geometry of the target-ion assembly.

The detailed view of the different components inside a Front end is shown in Figure 2.4. The target consists of 7 discs of UC_x having a diameter of 40 mm each, followed by a proton dumper made of carbon. The 40 MeV proton beam, when passed through the discs of UC_x, not only creates nuclear fission reactions but also introduces a heating effect in the target system. The heating effect from the proton beam could take the target system to a very high temperature. The distances between the discs, as shown in Figure 2.4 a), are determined to maintain a uniform temperature profile of the whole target system when the proton beam passes through the target.

After passing through the last discs of the target assembly, the proton beam is very close to the Bragg peak. At this point, the proton beam meets the dumper (C) in Figure 2.4 and deposits all of its residual energy. This would mean that the dumper is much more intensely heated compared to the rest of the target. This is in fact why the dumper is left thermally not shielded as seen in Figure 2.4 b). The rest of the target, consisting of the 7 UC_x discs are well shielded with tantalum (Ta). It is also used as a heater when the target needs to be pushed to a higher temperature than the one achieved via the thermal effect of the proton beam. This is done through Joule heating in which calibrated values of current are applied to the Ta heaters. The nominal operating temperature of the target

is around 2000°C.

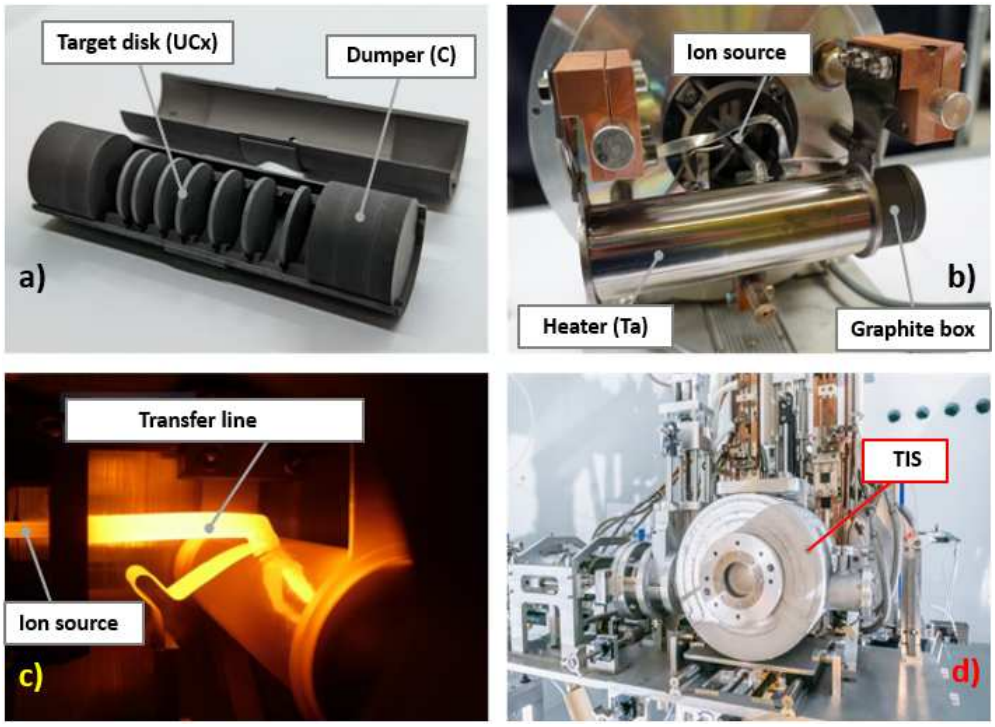

Figure 2.4: a) SPES target assembly with 7 discs of UC_x with 40 mm diameter each. b) Target assembled in the Front end with a Ta heater. c) Heating of the target, transfer line and the ion source. d) Closed Target-Ion Source (TIS) assembly with water cooling.

Roughly halfway along the length of the target, there is a circular hole of approximately 9 mm in diameter, which provides the exit of the fission products from inside the target. A transfer line, as shown in Figure 2.4 c), is fit into this hole. The transfer line is also maintained at a very high temperature, to avoid sitting of these products on the tube of the line. These products effuse through the transfer line to the ion source where they are ionized and extracted down the beam line. There are 3 main types of ion sources employed: surface, plasma, and laser. The principles and suitability of each ion source will be discussed in detail in Section 3.2. In the context of this thesis, the laser ion source is the motivation for most of the activities performed.

Figure 2.4 d) shows a complete assembly of the target system. This whole target system has features to be handled by dedicated robots as it will be highly radioactive once irradiated with the proton beam. As seen in the picture, the target container has circular indents. These are water-cooling pathways embedded inside the container itself.

2.2 Laser Ion Source (LIS)

A simple representation of a laser ion source (LIS), adopted from [6], is shown in Figure 2.5. The principle of a LIS is to shine a laser of precise wavelengths into the hot cavity of the ion source (same as that of surface ion source), where particular elements are resonantly ionized, with very high chemical selectivity. The incident laser beams are precisely tuned to the wavelengths corresponding to the electronic transitions of the element of interest. This process, called resonance laser photo-ionization, will be thoroughly discussed in Section 3.2.3.

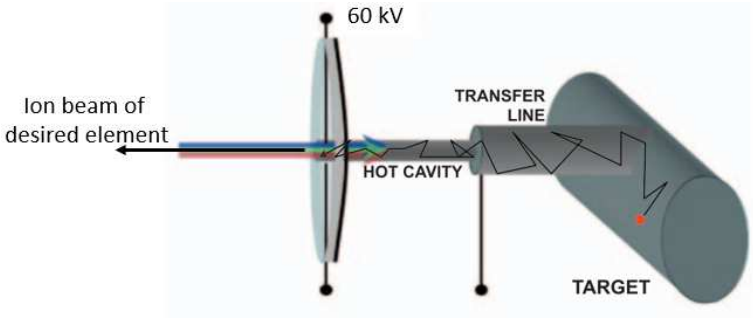

Figure 2.5: Working principle of a laser ion source

It is evident that the laser beams need to be transported all the way down to the ion source, with proper beam shape and focusing to interact with the atomic species present inside the ion source. One of the features of a laser ion source is the robustness of the system. The laser systems are placed at a considerably safe distance from the ion source/front-end assembly. In the case of the SPES project, the laser systems are placed 25 meters far away in an ISO8 class laser laboratory [1]. The lab is placed at level +1, just on the top of the combiner magnet room, while the ion source is placed at level -1, as laid out in Figure 2.6. Light over-pressure air is maintained inside the laboratory to avoid contaminating dust from the external environment. The air conditioning system ensures temperature stability of $\pm 1^{\circ}$C, and laminar air flux on each table is provided by filtering hoods on the roof.

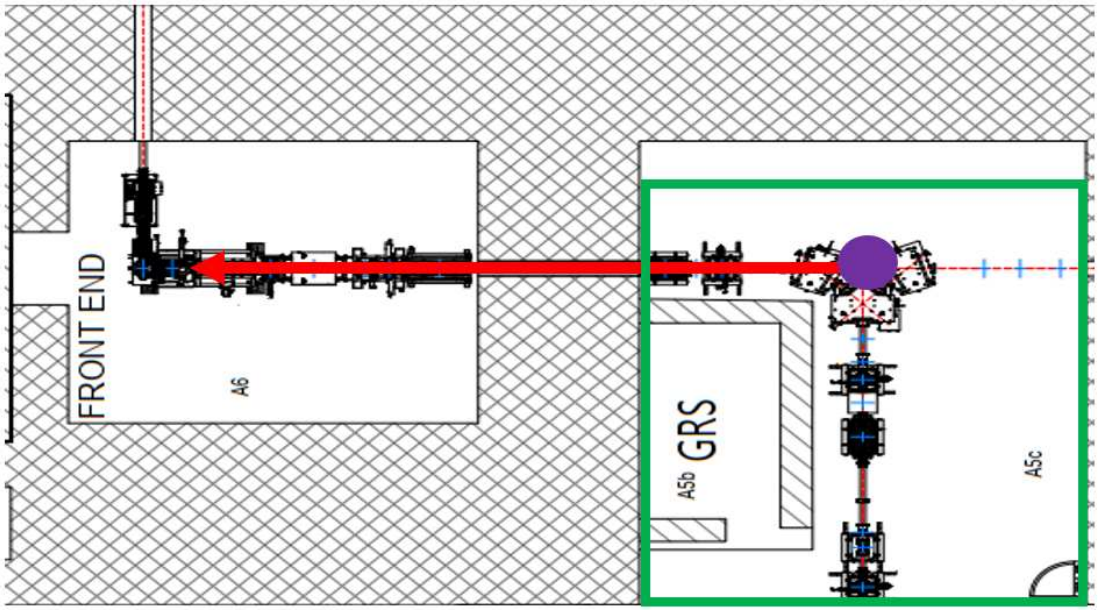

Figure 2.6: Layout of SPES building level -1 [Top View]; the green box represents the laser laboratory at level +1; the purple dot represents the *descending point for the laser beams*, while the red arrows represent the laser beam path through the vacuum beamline to the ion source.

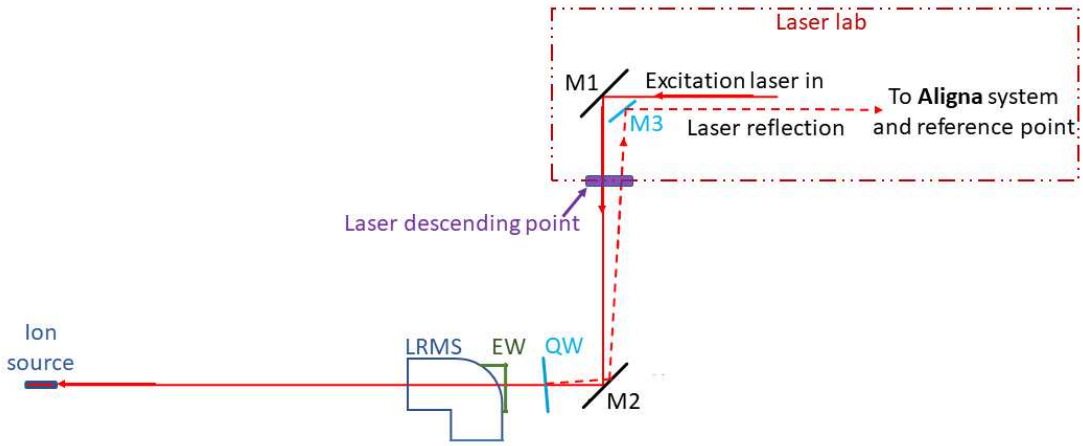

Figure 2.7: Schematic representation of laser alignment and stabilizing system [Side View]. LRMS represents the low-resolution mass separator magnet. EW represents the entrance window and QW is a slightly tilted Quartz window. M1, M2, and M3 represent the mirror systems.

A window is placed on the floor of the laser lab, which acts as the descending point of the laser beams, represented as the purple dot in Figure 2.6. The laser beams can reach the ion source by entering the beam line pipe using the vacuum

view-port access in the magnet chamber.

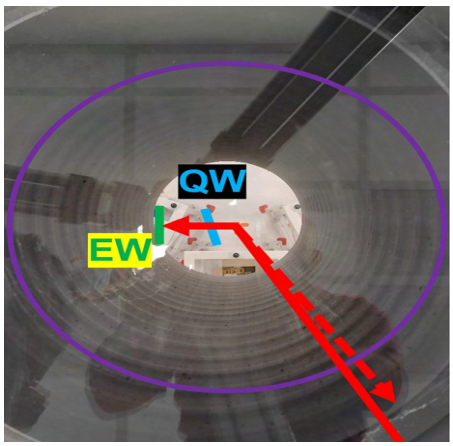

Figure 2.8: Laser descending point

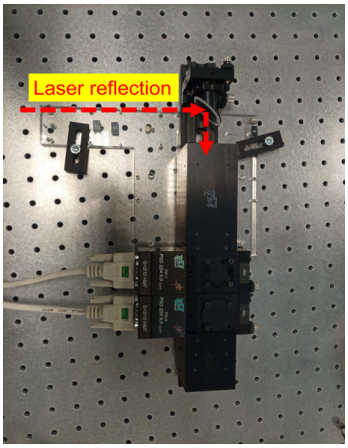

Figure 2.9: Aligna system

Figure 2.8 and 2.9, show the real-life images of the laser descending point and the Aligna system mentioned in the scheme represented in Figure 2.7. Aligna is a stabilizing system that employs the principle of position detection [7].

How the laser beams are aligned to the ion source

As shown in the scheme represented in Figure 2.7, the laser beams are transported from the laser lab through multiple optics. Mirror M1 provides the first reflection of the laser beam downwards through the descending point. This beam is reflected horizontally towards the direction of the ion source by mirror M2. Now, the laser beam passes through two windows - QW (a slightly tilted quartz window) and EW (an entrance window which lets the laser through the magnet and arrive at the ion source).

The window QW provides a very essential back reflection. If uncoated fused silica is used, the total reflection would be about 8% as each surface reflects ∼4% of the incident beam power. The back laser reflection goes back upwards after hitting mirror M2. A dedicated mirror M3 is placed in the path of the laser reflection to collect it and send it to the laser lab where it is used to monitor for a reference point and also for stabilizing the beam using a Aligna system.

Four different laser paths will be directed to the ion source from the laser lab. Each path will have a dedicated combination of M1, M2, and M3 with coatings suitable for different wavelength ranges. Also, an Aligna system for each path is placed for beam stabilization.

Why stabilizing system is required for the laser beams

In the case of an ideal alignment, the overlap between the ionization volume and the laser beam is maximum and matches the inner hollow cylinder volume of the ion source. Any misalignment reduces this overlap volume, a smaller interaction space for atoms and photons to be defined, and a decrease in the rate of ion production. If there is any fluctuation in the interaction volume over time, this is clearly reflected immediately in the ion current generated by the laser beams.

The SPES ion source is a 30 mm long tube with a 3 mm entry hole [8], and it is located roughly 20 meters away from the exit point of the laser beams from the laser lab. To hit this volume without any significant fluctuation, after a laser beam path length of around 20 meters, requires a very high pointing stability. There are always vibrations and mechanical disturbances in the facility that need to be taken into account. In other words, pointing stability better than 0.05 $mrad$ is required and this is provided using the Aligna system.

2.2.1 Advantages of LIS

A laser ion source (LIS) is generally preferred over other types of ion sources viz. surface and plasma ion sources. Some of the main advantages of using a LIS are:

- Almost 100% element selectivity: It means, when combined with the mass separation technique, gives a very high purity isotopic beam.
- High efficiency (tens of percents [9])
- Reduced isobaric contamination
- Easy beam diagnostics: The ion beam produced by the laser can be easily diagnosed and cross-checked by turning the laser on/off.
- The ionization region is simple and robust

Principles and application of the different ion sources will be further discussed in Section 3.2.

2.2.2 Choice of laser systems

Linewidth, power, repitition rate requirement

The availability of tunable laser light that can match the fully resonant excitation of upper atomic levels in a range from UV (about 250 nm) to IR (close to 1.0

μm) is the essential requirement of a laser ion source. The spectral linewidth is another limiting parameter in addition to the wide tuning range. A spectral linewidth of the order of 100 MHz would be necessary to resolve the energy levels of two distinct isotopes. On the other hand, this requirement is loosened to within the 1-10 GHz range due to the Doppler broadening caused by temperatures of roughly 2000° C, typical of the environment in the target/reaction chamber and ion source.

At 2000°C, the typical effusion time of the atoms through the hot cavity end is in the orders of 100 μs [10]. A repetition rate of at least 10 kHz is necessary for the presence of photon flux in this time frame. These requirements can be met by modern tunable laser sources, which can also deliver intensity values in the mW range (for the UV) to several W (in the visible and IR) sufficient for step-wise ionization of practically most elements.

Ti:Sa systems installed in SPES facility

In the SPES site, three Ti-Sa cavities operating at 10 kHz are already in place inside the laser lab. These cavities from *Sirah Credo* have double Ti-Sa crystal configuration, see Figure 2.10. The optical layout of the cavities is clearly shown in Figure 2.11, adopted from [1]. Each of the cavities is individually pumped with *Ascend* pump lasers from *Spectra-Physics*.

These laser systems have been specifically developed to meet the technical demands of SPES project. The two crystals are placed in a geometry that provides optimal waist size of the pump power propagation and consequently a higher output power. As shown clearly in Figure 2.11, the pump power goes through a 50-50 beam splitter and reaches the two crystals from opposite directions through the respective focusing lenses.

The wavelength selection is provided by a combination of birefringent filter and etalon system(s). The wavelength selection elements are mounted on an automated motion stage and are easily controlled through a software interface. One of the cavity-end mirrors is triple coated for high reflectivity at three different wavelength ranges. This is provided for power optimization over a large wavelength range and there is a manual switch system for the coatings. Each system is equipped with an intracavity Pockels cell which allows the synchronization of the laser pulses produced by the three Tisa cavities. Also, each unit has its own optical fiber coupling system which allows wavelength reading through a WS7 lambda-meter.

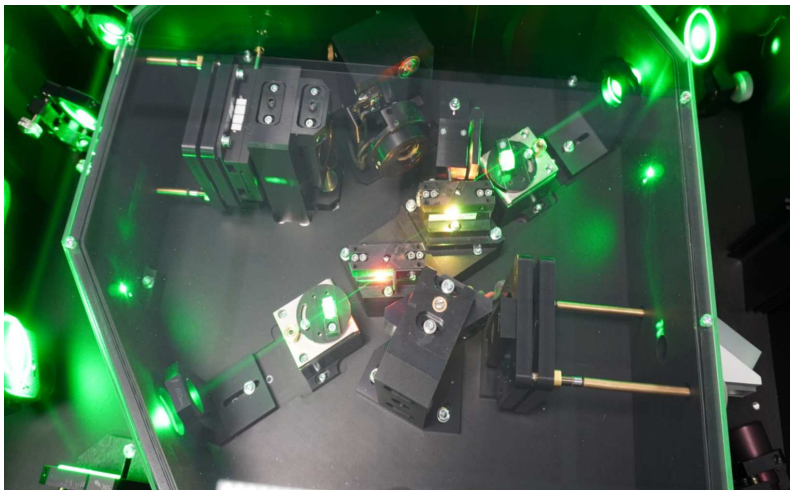

Figure 2.10: Sirah Credo Ti:Sa 10 kHz cavity

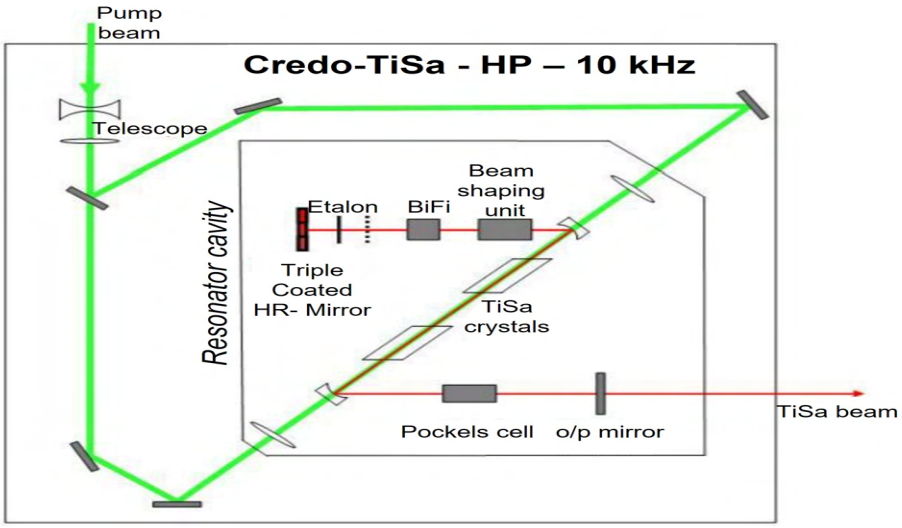

Figure 2.11: Optical layout of the Sirah Ti:Sa system, with a Z-shaped cavity.

The main parameters of the Ti:Sa systems are listed in Table 2.1, adopted from [1]. The λ_{Peak}, indicated in the table, is the wavelength value at which the system has the highest gain or maximum output power. For a Ti:Sa system, this value lies between 800-850 nm.

A tunability range of 690-950 nm is provided for the fundamental output of these systems. To be able to effectively use the Ti:Sa systems for ion production, a wider range of wavelength coverage is essential. The system is completed with a set of two higher harmonic generation units from *Sirah HHG*. These units allow the generation of second or third or fourth harmonics. The power measurement of these harmonics at 51 W of pump power for one of the Ti:Sa is shown in Figure 2.12.

Table 2.1: Table of main laser system parameters.

Parameter	**Value**
Pump Repetition Rate	10 kHz
Pump Power	57 W
Tuning Range	690 - 950 nm
Pulse Duration (τ_{FWHM})	30 - 50 ns
Repetition Rate	10 kHz
Output Power (λ_{Peak}@10 kHz)	6,8 W
Line-width	$<$ 6 GHz (One Etalon)
	$\sim$ 1 GHz (Two Etalons)
Beam divergence	$<$ 1,5 mrad
Beam diameter	1 mm Typ.

There is an evident gap in the wavelength range of roughly 480-680 nm. This gap can eventually be covered by wavelength mixing of the fundamental wavelengths with an appropriate wavelength (532 nm pump laser normally used). Alternatively, dye lasers can be used for this range of wavelengths. However, it is preferred to avoid dye laser systems as they can be potential hazards due to the use of alcoholic solutions.

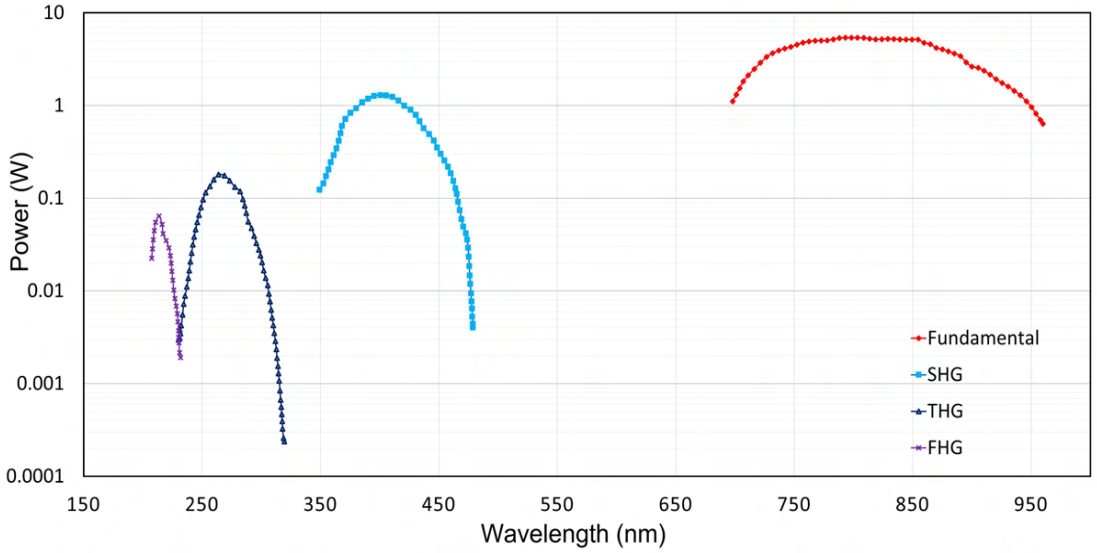

Figure 2.12: Power vs wavelength of the different harmonics of the Ti:Sa. SHG, THG and FHG represent second, third, and fourth harmonic generations respectively.

2.3 Isolpharm Project

The ISOLPHARM method is an innovative method to produce radioactive nuclides using the ISOL technique [11]. It will provide radionuclides that are difficult to be produced with traditional methods. Among many nuclides that can be produced, ^{111}Ag could be a promising radionuclide for internal radiotherapy. Its proof-of-concept production in a highly pure form with the ISOL technique and its targeted delivery for medicine are currently investigated inside the ISOLPHARM project. In the SPES UC_x target, more than 80 GBq of ^{111}Ag could be produced after 5 days of irradiation with a primary proton beam of 40 MeV energy and a current of 200 μA [12].

When produced in a nuclear reactor, the isobaric contaminants must be separated chemically in order to obtain a high-purity radioactive ion beam. For many radionuclides including ^{111}Ag, the presence of stable and unstable isobars cannot be effectively separated using the traditional method of chemical separation. In the ISOLPHARM technique, the radionuclide of interest can be selectively ionized and extracted by using methods like resonant ionization laser ion source.

Chapter 3

Theoretical Background

3.1 Atomic Level Structure

For an electronic transition between an upper energy atomic level k and a lower level i, the energy of the photon is given by

$$\Delta E = E_k - E_i = h\nu = hc\sigma = hc/\lambda \tag{3.1}$$

where ν, σ and λ are the frequency, wavenumber and the wavelength respectively. Frequencies are expressed in Hertz (1Hz= cycle/sec) while wavelengths are mostly expressed in nanometer (nm). The SI unit of wavenumber is the inverse meter but in practice, it is usually expressed in inverse centimeters, which is $1cm^{-1} = 10^{-2}m^{-1}$ and corresponds to $\simeq$ 29.98 GHz.

Atomic energies are often expressed in terms of electron volts (eV). We can convert 1 eV in terms of other physical quantities:

$$2.42 \times 10^{14} Hz$$

$$8065.54\ cm^{-1}$$

$$1239.84\ nm$$

$$11604.45\ K$$

$$1.6 \times 10^{-19} J$$

3.1.1 Energy Levels

The energy of an electron attached to an atom is determined by its position within the discrete energy level structure and is the result of several electron-electron and

electron-nucleus interactions. For a one-electron atom (hydrogen or hydrogen-like atoms), an atomic state is defined by the quantum numbers nlm_jm_s, where n is the principal quantum number, l is the electron orbital angular momentum and s is the intrinsic electronic spin. Magnetic quantum number m_l is the projection of the angular momentum l on the quantization axis.

The energy of the hydrogen atomic states is dependent only on the principal quantum number n and has a degeneracy with respect to l and m_l. Without relativistic corrections, the energy values are given by:

$$E_n = -R_y\left(\frac{Z}{n}\right)^2 \tag{3.2}$$

where R_y is the Rydberg constant (with reduced mass), R_y= 13.61 eV.

The allowed values of the quantum numbers are :

n= 1, 2, 3, ...

l= 0, 1, 2, ... , n-1

m_l= -l, -l+1, ... , l-1, l

m_s= $\pm\frac{1}{2}$

The Pauli exclusion principle prohibits atomic states from having two electrons with all four quantum numbers the same. Thus the maximum number of equivalent electrons permitted is $2(2l + 1)$. The degeneracy of an atomic level with an energy E_n is that given by,

$$\sum_{l=0}^{n-1} 2(2l+1) = 2n^2 \tag{3.3}$$

In the presence of external influences such as electric fields, magnetic fields, etc., or additional interactions within the atomic system itself such as ls-coupling, the degeneracy can be removed and we start observing splittings and shifts of individual levels.

If the ls-coupling is considered, the electronic state can be described with the configuration $nljm_j$, where j is the total angular momentum given by $l + s$ and m_j is the projection of the total angular momentum j on the z-axis. There are $2j + 1$ magnetic sub-states, m_j, which are degenerate in the absence of an external magnetic field.

3.1.2 Orbital Energies and Atomic Structure

From Equation 3.2, it is seen that the energy of atomic orbitals increases as the principal quantum number, n, increases. In any atom with two or more electrons, the repulsion between the electrons makes energies of sub-shells with different

values of l differ. Following the order of repulsion, the energy of the orbitals increases within a shell in the order $s < p < d < f$. The energy increases as we move up from $1s$ to the $2s$ and then $2p$, $3s$, and $3p$ orbitals. It shows that, for small atoms, the increasing n value has more influence on energy than the increasing l value. However, this pattern does not hold for larger atoms. The $3d$ orbital has higher energy than the $4s$ orbital and such overlaps continue to occur frequently as the number of electrons increases.

Figure 3.1 shows how the electrons are gradually filled in the order of the sub-shells depicted by the arrows in the diagram.

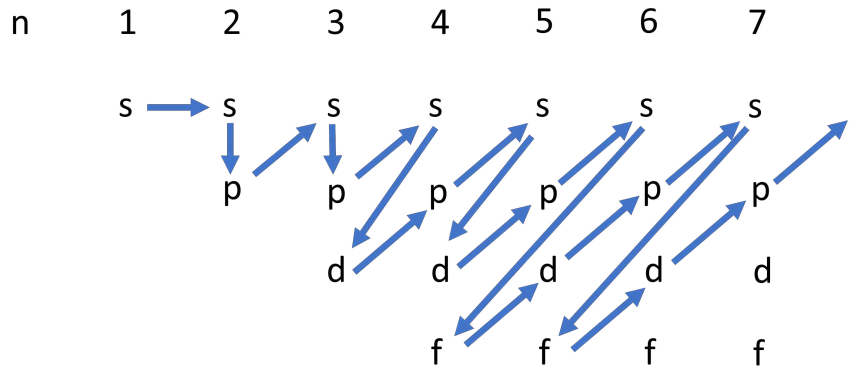

Figure 3.1: The arrow leads through each sub-shell in the appropriate filling order for electron configurations.

3.1.2.1 Multi-Electron Configurations and Coupling Schemes

When we are talking about atoms with multiple electrons, the system is much more complex than the trivial characteristic quantum numbers n, l, m_l, and m_s. Several interactions between the electrons come into play which are described using *resultant quantum numbers*.

LS Coupling (Russell-Saunders Coupling)

In the case of light multi-electron atoms (Z $<$ 30), the electron spin coupling between the electrons is larger compared to the individual electron spin–orbit interaction than it is for heavier atoms. LS (or Russell-Saunders) coupling is used to describe the atomic states.

The scheme introduces respective moments coupled to a total spin and angular momentum,

$$\vec{S} = \sum_i \vec{s_i} \tag{3.4}$$

$$\vec{L} = \sum_i \vec{l_i} \tag{3.5}$$

where $\vec{S}$ is the total spin given by spin-spin interaction, $\vec{L}$ is the coupling of the orbital angular momenta $\vec{l_i}$ of the valence electrons.

The total angular momentum vector J of the level is consequently given by,

$$\vec{J} = \vec{L} + \vec{S} \tag{3.6}$$

whose value lies in the range $|L - S| \leq J \leq |L + S|$.

A common way to name states in atomic physics is to use spectroscopic notation. It is essentially a standard way to write down the angular momentum quantum numbers of the valence electrons' state. It is denoted using the "term symbol":

$$^{2S+1}L_J^{(o)}$$

where o indicates the odd parity of the wave function. If o is not indicated, it represents an even parity. Parity is simply expressed as $(-1)^L$. The angular momentum L is designated as $S, P, D, F, ..$ for $L = 0, 1, 2, 3, ..$

In the term symbol, the term $2S + 1$ denotes the spin multiplicity which is derived from the number of possible fine structure states of J.

Two simple examples are discussed below:

1. $3d^7\ ^4F_{7/2}$
2. $3d^7(^4F)4s4p(^3P^o)\ ^6F^o_{9/2}$

In the first example, the seven $3d$ electrons couple to give the $^4F_{7/2}$ term. While in the second example, the seven $3d$ electrons couple to give a ^4F term and the $4s$ and $4p$ electrons couple the form the $^3P^o$. In this case, the ^4F is called grandparent term, and the $^3P^o$ as the parent term. The final $^6F^o_{9/2}$ term is one of the 9 possible terms obtained by coupling the grandparent and the parent term.

jj Coupling

For heavier elements, spin-orbit interaction of an individual electron is dominant over spin-spin interaction between the electrons. This mechanism predominantly occurs for elements with $Z > 60$ and for higher excited atomic states. The individual angular momenta is give by,

$$\vec{j_i} = \vec{l_i} + \vec{s_i} \tag{3.7}$$

These individual momenta couple to give the overall angular momentum defined as,

$$\vec{J} = \sum_i \vec{j_i} = \sum_i (\vec{l_i} + \vec{s_i}) \tag{3.8}$$

The spectra are expected to be more complex for this kind of coupling compared to LS coupling.

As a general observation, an intermediate coupling scheme is present with LS coupling at low excitation energies which gradually develops into jj coupling with higher excitation energies.

Hyperfine Structure (HFS)

The hyperfine structures result as a consequence of coupling of the total angular momentum $\vec{J}$ of the electron to the total nuclear spin $\vec{I}$.

As in the case of electrons, the nucleons have equivalent quantum numbers spin $\vec{s_i}$ and angular momentum $\vec{l_i}$. The total nuclear spin $\vec{I}$ is given by,

$$\vec{I} = \sum_{i=1}^{A} (\vec{s_i} + \vec{l_i}) \tag{3.9}$$

For nuclei with an even number of protons and neutrons, the value of $I = 0$ (in the ground state) as the pairwise anti-parallel orientation of the angular momenta is energetically favored.

Whereas in the case of an odd number of either the protons or the neutrons or both, a non-zero value of I is obtained which induces a magnetic moment $\vec{\mu}_I$. This nuclear magnetic moment $\vec{\mu}_I$ couples to the magnetic field $\vec{B}_J$ introduced by the total angular momentum $\vec{J}$ of the electron at the position of the nucleus. The coupling mechanism results in an energy shift given by,

$$\Delta_{HFS} = -\vec{\mu}_I . \vec{B}_J = \mu_I B_J \frac{\vec{I}.\vec{J}}{|I||J|} \tag{3.10}$$

The coupling between $\vec{I}$ and $\vec{J}$ can be defined by a new total angular momentum $\vec{F}$ which is defined as,

$$\vec{F} = \vec{I} + \vec{J} \tag{3.11}$$

The quantum values of $\vec{F}$ vary within the range $|I - J| \leq F \leq |I + J|$. The expression for the energy shift can now be re-written as,

$$\Delta_{HFS} = \mu_I B_J \frac{\vec{I}.\vec{J}}{|I||J|} = \frac{A}{2}[F(F+1) - I(I+1) - J(J+1)] \tag{3.12}$$

where A is the hyperfine coupling constant defined as $A = \mu_I B_J / IJ$. This parameter is a characteristic of the atomic level. The value of A can be obtained via laser spectroscopy, the nuclear magnetic moment μ_I can be derived eventually. It is especially valuable for the determination of an unknown nuclear spin.

3.1.2.2 Selection Rules

The selection rules for atomic transitions arise from momentum conservation and symmetry rules. Using these rules for electric dipole transitions of an atom is a guide to understanding whether a transition between the levels is allowed or not.

Table 3.1: Selection rules for allowed optical electric dipole transitions

	Electric dipole E1 (allowed)
Rigorous rules	1. $\Delta J = 0, \pm 1$ ($0 \not\leftrightarrow 0$) 2. $\Delta M_J = 0, \pm 1$ ($0 \not\leftrightarrow 0$, when $\Delta J = 0$) 3. Parity change
LS Coupling	4. $\Delta S = 0$ (not strict) 5. $\Delta L = 0, \pm 1$ ($0 \not\leftrightarrow 0$)
Hyperfine interaction	6. $\Delta F = 0, \pm 1$

3.1.2.3 Spectral Lines

Emission Lines

The total power radiated ϵ in a spectral line of frequency ν per unit source volume and per unit solid angle is expressed as:

$$\epsilon = \frac{h\nu A_{ki} N_k}{4\pi} \tag{3.13}$$

where A_{ki} (expressed in s^{-1}) is the atomic "transition probability" from level k to i and N_k is the number density (number/volume) of the excited atoms in the upper (initial) level k.

If we have a homogeneous light source of length l, the total emitted line intensity is given by:

$$I_{line} = l\epsilon_{line} = \int_0^\infty I(\lambda) d\lambda = \frac{hcA_{ki} N_k l}{4\pi\lambda_o} \tag{3.14}$$

where $I(\lambda)$ is the specific intensity at wavelength λ, and λ_o is the wavelength corresponding to the line center.

Absorption Lines

In the case of absorption, the so-called reduced absorption is given by,

$$W(\lambda) = [I(\lambda) - I'(\lambda)]/I(\lambda) \tag{3.15}$$

where $I(\lambda)$ is the intensity of the incident light with wavelength λ and $I'(\lambda)$ is the intensity of the light after passing through an absorbing medium.

The reduced line intensity from a homogeneous absorbing medium of length l can be obtained from,

$$W_{ik} = \int_0^\infty W(\lambda)d\lambda = \frac{e^2}{4\epsilon_o m_e c^2}\lambda_o^2 N_i f_{ik} l \tag{3.16}$$

where f_{ik} (an adimensional quantity) is the atomic absorption "oscillator strength", ϵ_o is the dielectric permittivity of vacuum and m_e is the mass of an electron.

Line Strengths

To define line intensities, transition probabilities A_{ki} and absorption oscillator strength f_{ik} are mainly used. Another quantity that is also very commonly used in this context is the "line strength S" which is defined as,

$$S = S(i,k) = S(k,i) = |R_{ik}|^2 = <\psi_k|P|\psi_i>^2 \tag{3.17}$$

where ψ_i and ψ_k are the initial and the final state wave functions. R_{ik} is the transition matrix element of the appropriate multipole operator P. R_{ik} takes into account the integration over spatial and spin coordinates of all N electrons of the atom or ion.

For an allowed electric dipole transition E1, the values of A, f and S are related as,

$$A_{ki} = \frac{2\pi e^2}{m_e c\epsilon_o \lambda^2}\frac{g_i}{g_k}f_{ik} = \frac{16\pi^3}{3h\epsilon_o\lambda^3 g_k}S \quad \text{[in SI units]} \tag{3.18}$$

$$A_{ki} = \frac{6.6702\times10^{15}}{\lambda^2}\frac{g_i}{g_k}f_{ik} = \frac{2.0261\times10^{18}}{\lambda^3 g_k}S \quad \text{[in atomic units]} \tag{3.19}$$

where g_i and g_k are statistical weights, obtained from the appropriate angular momentum quantum numbers.

For a spectral line, the value of g is given by,

$$g_x = 2J_x + 1 \tag{3.20}$$

While in the case of a multiplet,

$$\overline{g}_x = \sum_x (2J_x + 1) = (2L_x + 1)(2S_x + 1) \tag{3.21}$$

From Equation 3.19, it can be eventually derived that, for atomic units,

$$f_{ik} = \frac{2}{3}\frac{\Delta E}{g_i} S \tag{3.22}$$

3.2 Ionization Processes

Several elements and their isotopes, stable and radioactive, will be ionized and extracted in the SPES facility. Figure 3.2 highlights the elements of interest so far for the project. The elements are assigned different colors, for visual understanding, depending on the type of ionization process that will be used.

The alkali metals are very effectively surface-ionized due to their low ionization potential (IP). For most elements having an IP between 5-9 eV, they can be efficiently ionized using lasers with a satisfying purity. More than 80% of elements in the periodic table have IP in this range [13] and thus laser ionization is a very useful and dominating technique. For elements having IP beyond 9 eV, ionization via electron bombarding is used, which is also termed as plasma ion source.

3.2.1 Surface Ionization

When an atom interacts with a surface at a high temperature, it can lose or gain an electron, becoming a positive or negative singly charged ion. This physical phenomenon is called surface ionization. The result depends on the ionization potential (IP) of the atom and the work function ϕ of the surface material. In ISOL facilities, surface ionization sources made of high ϕ materials are efficiently used to produce positive ion beams for elements with IP lower than 7 eV [14].

In a hot cavity, ions are also created due to surface ionization from the hot wall of the cavity itself. The Saha-Langmuir equation [15] can be used to describe the relative proportion of the ionic density n_i to the atomic one n_o in thermal equilibrium. This is also termed the degree of surface ionization α,

$$\alpha = \frac{n_i}{n_o} = \frac{g_i}{g_o} exp\left(\frac{\phi - W_i}{k_B T}\right) \tag{3.23}$$

where ϕ is the work function of the cavity material, W_i is the ionization energy of the element of interest, g_i, and g_o are the statistical weights of the ionic and atomic ground states, k_B is the Boltzmann constant and T is the absolute temperature.

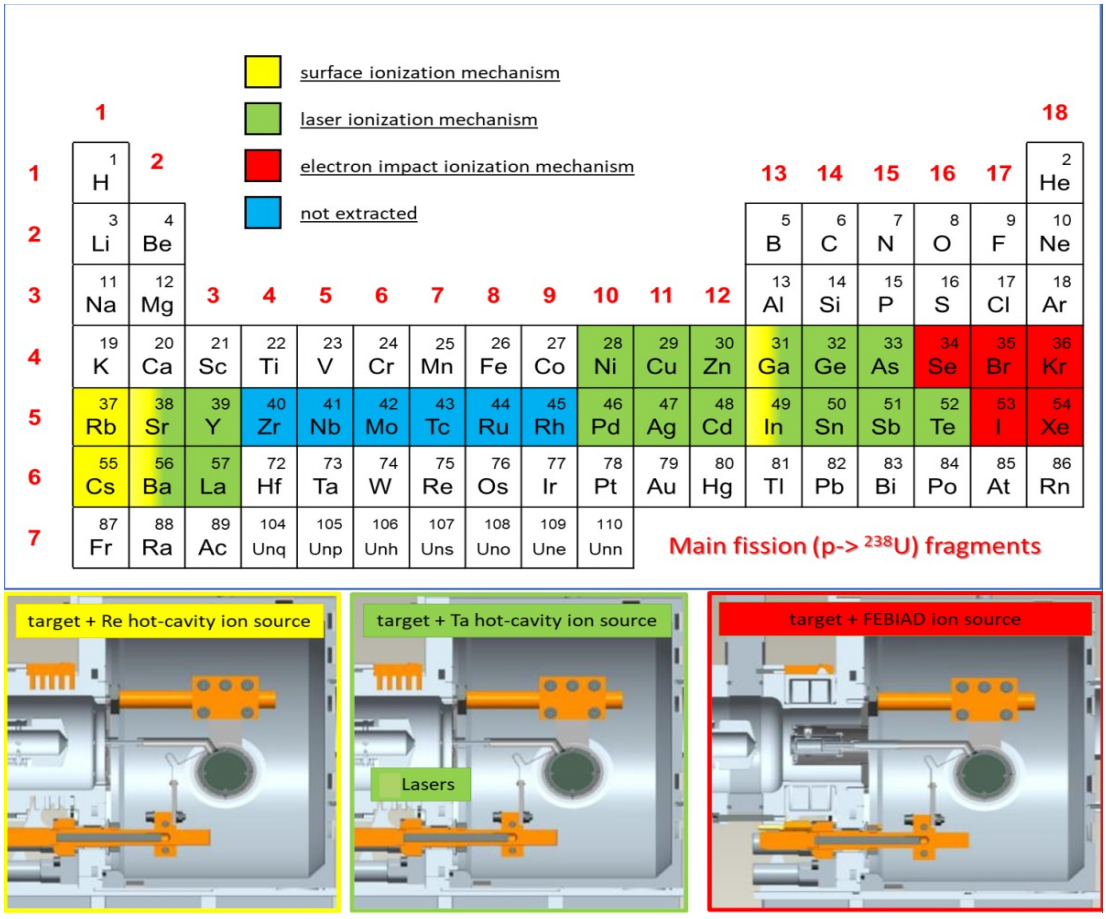

Figure 3.2: Atomic elements and their corresponding suitable ion sources for SPES project. The surface ion source is represented in yellow, the laser ion source is represented in green, and the plasma ion source is represented in red.

When the excitation level of the element (atom) or its ion is comparable with the thermal energy k_BT, the ratio of the statistical weights g_i/g_o in the above expression is replaced by the ratio of the partition functions Q_i/Q_o [16, 17]:

$$Q_x = g_x + \sum_j g_{jx} exp(-E_{jx}/k_BT) \tag{3.24}$$

where E_j is the excitation energy of a particular state of the atom ($x = o$) or the ion ($x = i$).

In such a case, the degree of ionization α can be expressed as

$$\alpha = \frac{Q_i}{Q_o} exp\left(\frac{\phi - W_i}{k_BT}\right) \tag{3.25}$$

The surface ionization efficiency β can be expressed in terms of α with a simple relation given by,

$$\beta = \frac{n_i}{n_i + n_o} = \frac{\alpha}{1 + \alpha} \tag{3.26}$$

In a hot cavity, the experimental values of α and β are observed to be significantly higher than given by the equations above. This is explained by an amplification factor N induced in the hot cavities as a consequence of multiple collisions inside the hot cavity wall [18]. This will be discussed in detail in the section 5.1.

Competition between surface and laser ionization in a hot cavity

When we talk about laser ion sources, it is quite a simple introduction of laser beams into the hot cavity of the surface ion source. Even if the lasers are more than capable of ionizing an atom in the initial ground state, it is quite necessary that the atoms remain in the gaseous state without getting deposited on the walls of the cavity. In order to limit the atom-wall interaction time, a sufficiently high temperature is maintained in the cavity for laser ion sources as well.

If the temperature of the cavity is too high, it is very likely that more surface ions are produced, which means fewer neutral atoms available for laser interaction. To preserve atoms in a neutral state for effective laser ionization, the relation encourages low temperatures. On the other hand, ideally, a sample should be fully vaporized, had all of its molecules dissociated, and had a low wall sticking time in order to extract short-lived radioactive species. As a result and practical compromise, materials having work functions ϕ between 4 and 4.5 eV, such as tantalum or tungsten, are typically employed for construction. Low work function materials would be ideal for minimizing the surface ionization process, but these

compound materials are delicate, and inadequately resistant to mechanical stress. Higher temperatures have other negative effects on these materials and undergo rapid degradation over time [19].

3.2.2 Electron Impact Ionization

By bombarding an atom with projectiles, such as electrons with sufficient kinetic energy above the atom's ionization potential, one can also cause one electron to detach from the atomic shell.

A common plasma ion is the Forced Electron Beam Induced Arc Discharge (FEBIAD) ion source. A cathode is heated up by the Joule effect, allowing thermionic emission of electrons on the surface facing the anode grid. The anode is maintained at a much higher voltage in terms of hundreds of Volts and the electrons from the cathode are drifted towards the anode where a plasma is eventually confined. A small axial magnetic field is provided in the anode region which induces a spiral motion in the electrons [20]. This increases the rate of electron bombardment on the species present in the volume.

When neutral atoms are introduced in this volume, the valence electrons are knocked off due to this bombardment by the plasma electrons and ionization of these elements is achieved. It is not difficult to guess that this process is non-selective and has a very large spectrum of elements, including noble gases.

3.2.3 Resonance Laser Ionization

One of the fundamental requirements for the study of radioisotopes at ISOL facilities is the possibility of producing isotopically clean ion beams with minimal isobaric interference. The laser ion source is commonly the preferred choice since it offers the best elemental selectivity, which neither the surface nor the plasma ion sources can deliver [21]. For many elements, it is also the most efficient ionization method at online isotope separators and RIB facilities such as ISOLDE [22] or TRIUMF [23]. The step-wise photo-ionization method [24, 25] serves as the foundation for the resonance ionization laser ion source (RILIS). It exploits the unique electronic energy level structures of the elements, where it selectively promotes an electron beyond the ionization potential.

The wavelength-tunable lasers allow us to precisely match the frequency of the photons to the transition energy of the valence electron(s) of a particular element. When the photons are guided into a vapor of several elements, they will predominantly excite the electrons of the atoms of the targeted element. The valence electron is successively promoted by laser photons through the energy level

structure of the atom leading finally to either high-lying Rydberg states below the ionization potential (IP), auto-ionizing states, or directly into the continuum through the so-called non-resonant excitation.

The atomic transition between two bound states 1 and 2 can be characterized by an absorption cross section,

$$\sigma_{12} = \frac{g_1}{g_2} \frac{\lambda_{12} A_{21}}{4\pi^2 \Delta\nu_t^{12}} \tag{3.27}$$

where g_1 and g_2 are the degeneracy of the levels 1 and 2 respectively, λ_{12} is the wavelength of the incident laser, A_{21} is the Einstein coefficient and $\Delta\nu_{12}$ is the spectral width of the transition between states 1 and 2 in the laser atom interaction region.

Saturation of an atomic transition can be achieved with sufficient energy density of the laser pulse. Use of short laser pulses for resonant excitation minimizes the losses due to the spontaneous decay of excited atomic states. If the laser has a pulse duration $t_L < \tau_2$ (τ_2 is the decay time of the excited state 2), the "laser pulse energy density" required to saturate the resonant transition between the bound states 1 and 2 could be expressed as,

$$\epsilon_{12}^{sat} = \frac{h\nu_{12}}{2\sigma_{12}} \frac{\Delta\nu_L^{12}}{\Delta\nu_t^{12}} \tag{3.28}$$

where h is the Planck constant, ν_{12} is the frequency of the laser light and $\Delta\nu_t^{12}$ is the spectral line width of the laser.

For allowed electric dipole transitions between bound atomic states, the absorption cross-sections are typically in the range of $\sim 10^{-10} - 10^{-15}$ cm^2. For these transitions, saturation can be achieved with nanosecond lasers with an energy density in the range of $\sim 10^{-6} - 10^{-3}$ J cm^2. Transition to the ionization continuum has much lower absorption cross-section and therefore, are very difficult to saturate.

The RILIS technique is employed in many leading ISOL facilities such as CERN-ISOLDE [26, 27], GANIL [28], GSI [29], IRIS-PNPI [30], JG Mainz [31], JYFL [32], KU Leuven [33], RIKEN [34] and TRIUMF-ISAC [35]. In Letokhov's book Laser Photoionization Spectroscopy [24], the theory of resonance ionization is covered in detail with a focus on the resonance ionization spectroscopy method.

Producing an isotopic of high purity with RILIS technique

Figure 3.3: Principle of production of an isotopic beam with RILIS technique. The red-filled circle (with green cross-hairs) represents the isotope selected.

As discussed above, the RILIS technique is very element selective and can ionize atoms of just one particular element in the atomic vapor. When this technique is combined with a mass separation technique such as a dipole magnet or Wein filter, the atomic beam can be squeezed down to an isotopic level with very high purity, as laid out in Figure 3.3.

Different pathways of photo-ionization

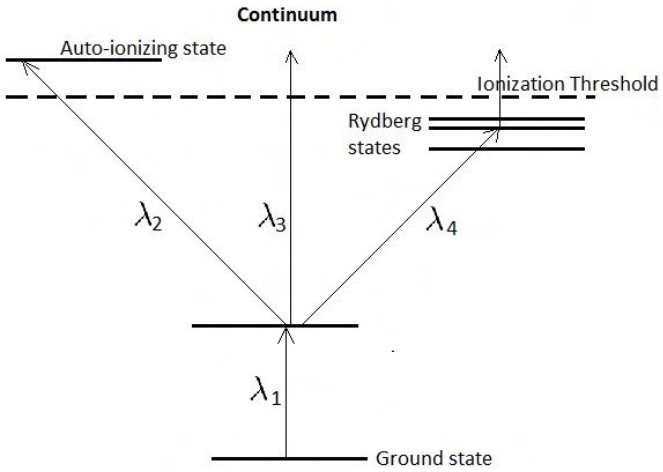

Figure 3.4: A simplified representation of different pathways of photo-ionization

In a laser ion source, an atom can be ionized via three typical multi-photoionization schemes, as shown in Figure 3.4. In all schemes, the atoms are initially excited to a discrete energy state well below the ionization threshold, IP, by the absorption of photons of wavelength λ_1. It should be noted that λ_1 is an over-simplification and could easily be a combination of multiple resonant steps to arrive at this discreet level.

The last transition that causes the ionization of the atom can be categorized as one of the following:

- Auto-ionizing states (λ_2)
- Non-resonant ionization (λ_3)
- Rydberg states (λ_4)

These pathways have different cross-sections and are roughly presented in Figure 3.5, adopted from [13].

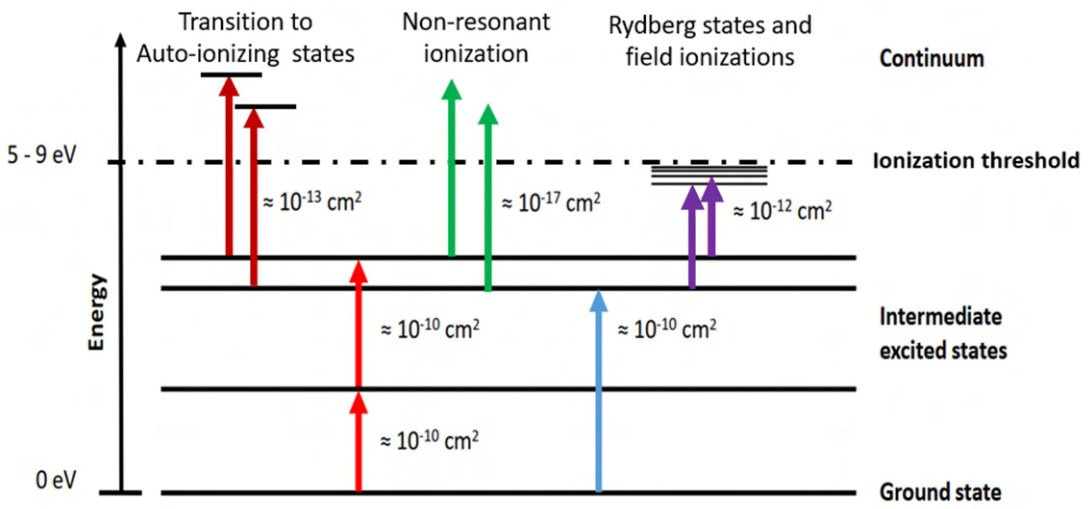

Figure 3.5: Cross sections of the different transitions are indicated roughly in orders of magnitude.

The resonant steps have higher cross-sections compared to other kinds of transitions. Clearly, a non-resonant ionization is the most unfavorable when it comes to cross-section value but several schemes employ this step if auto-ionizing states or Rydberg states of these elements are not well-known experimentally. The low value of the cross-section is compromised by usually using a high-power laser, in terms of several watts, for the non-resonant transition. The wavelength of this

laser could be any value that can provide photons higher than the energy gap to cross the ionization threshold.

It is important to note that these cross-section values drop roughly by two orders of magnitude in a hot environment due to different velocity components of the atoms.

3.2.3.1 Auto-Ionizing States (AIS)

For many elements, a complex energy-level structure exists above the ionization potential. Excited states within this region are known as auto-ionizing states. These states are the result of the excitation of two atomic electrons whose combined excitation energy is greater than the ionization potential (IP) of the atom. If the total excitation energy is higher than the IP, de-excitation may occur via a "non-radiative process" in which the excitation energy of one electron is transferred to the other, resulting in ionization. The typical lifetime of these decay channels is very short, in the order of 10^{-15} to 10^{-10} seconds, resulting in a large natural linewidth of several GHzs.

This state corresponds to a discrete level up till we ignore electron interaction. However, due to the interactions between the electrons, this state decays, resulting in the transfer of one electron into a lower state and the excess energy taken by the second electron, which releases the first.

3.2.3.2 Non-Resonant Photo-ionization

In this process, the ionization of atoms is achieved by non-resonant photon absorption from a suitable high-lying excited state to cause a transition to the continuum. This form of transition has a small cross-section (in terms of 10^{-17} cm^2). This transition consequently requires a greater photon flux than the stronger resonant transitions of previous excitation steps in the ionization scheme.

The final step power for a laser ion source installation is typically delivered using the laser with the maximum power available at a wavelength that allows the excited atom to reach the ionization potential. This could be a Nd: YAG laser with a second harmonic emission at 532 nm, depending on the laser configuration. Such a laser would be suitable if the previous transitions of the photo-ionization scheme excite the atom to within 18797 cm^{-1} from ionization threshold.

For a non-resonant transition step, the rate of photo-ionization is directly proportional to the number of photons available. So for a given laser wavelength of the non-resonant step, higher power assures higher ion current. Also, if the energy gap is within reach, using the fundamental emission of Nd:YAG i.e. 1064

nm could provide twice the number of photons compared to 532 nm at the same power. This scenario should also be considered for the choice of the laser.

3.2.3.3 Rydberg States

Rydberg levels are a series of high-lying excited states with a high and successively increasing, principal quantum number. The ionization potential of an atom may be precisely calculated by observing numerous Rydberg series members and the study of the energy level gap between them.

The energy gap between these levels and ionization potential is given by the Rydberg formula,

$$\Delta E_n = IP - \frac{R_y}{[n - \delta(n,l)]^2} \tag{3.29}$$

where IP is the ionization potential, R_y is the Rydberg constant (with reduced mass) and $\delta(n,l)$ is the quantum defect. The quantum defect accounts for the corrections to the Coulomb potential by the core electrons. The inner electrons of a multi-electron atom do not completely screen their associated nuclear charge.

Transitions to the high-lying and abundant Rydberg levels can have huge photon absorption cross sections (in terms of 10^{-13} cm^2), comparable to the auto-ionizing states. Rydberg levels can have long lifetimes (a few microseconds) and increase approximately as the cube of the effective quantum number [36]. These levels are very susceptible to external effects because of their long lifetimes and their proximity to the ionization potential in terms of energy. The Rydberg atoms can be, thus, ionized with the mechanisms such as: electric field, collision and thermal excitations.

3.3 Transition Line Shapes and Broadening Effects

3.3.1 Natural Linewidth

The uncertainty principle suggests that for particles with extremely short lifetimes, there will be significant uncertainty in the measured energy. As a consequence, the energy level above ground state with energy E and lifetime ζ has uncertainty in energy,

$$\Delta E.\zeta \geq \hbar/2 \tag{3.30}$$

The short-lived states have large uncertainties in energy. A photon emitted in a transition from this level to the ground state will have a range of possible

frequencies,

$$\Delta\nu_{nat} \sim \frac{\Delta E}{h} \sim \frac{1}{4\pi\zeta}; \quad [\hbar = h/2\pi] \tag{3.31}$$

If an atomic state n has spontaneous decay to all lower energy levels n', the decay rate is given by,

$$\gamma = \Delta\nu_{nat} = \sum_{n'} A_{nn'} \tag{3.32}$$

The line profile for transitions to the ground state is of the form,

$$\phi(\nu) = \frac{\gamma/4\pi^2}{(\nu - \nu_o)^2 + (\gamma/4\pi)^2} \tag{3.33}$$

Thus for an unsaturated atomic transition, the resonance profile is given by a Lorentzian profile with the natural linewidth γ of the transition.

The full width at half maximum (FWHM) of the Lorentzian profile is,

$$\Delta\nu_{nat-FWHM} = 2\gamma = \frac{1}{2\pi\zeta} \tag{3.34}$$

Typical lifetimes of the atomic levels are in the range of several nanoseconds and hence, natural linewidth falls in the range of 10 to 100 MHz.

For a two-level system, the natural linewidth of the transition can be simply related to the atomic transition probability A_{ki} using the equation,

$$\zeta = \frac{1}{A_{ki}} \tag{3.35}$$

If radiation is present, stimulated emission rates are added to the spontaneous ones. Away from the center, the decay is very much slower compared to the Gaussian profile. Generally, the natural linewidth is not directly observed as other broadening mechanisms usually dominate.

3.3.2 Doppler Broadening

Random motions of atoms in a gas depend on temperature. Doppler broadening is the result of the velocity distribution of atoms in a vapor due to the vapor temperature. The velocity distribution follows a Maxwell–Boltzmann distribution.

The velocity distribution $dN(v_x)$ has the dependency as the following,

$$dN(v_x) \propto exp\left(- \frac{mv_x^2}{2k_BT} \right) dv_x \tag{3.36}$$

where m is the mass of an atom, k_B is the Boltzmann constant and T is the temperature of the vapour.

However, for the modulus of the velocity vector, $dN(v)$ has an extra factor of v^2,

$$dN(v) \propto v^2 exp\left(- \frac{mv^2}{2k_B T} \right) dv \tag{3.37}$$

The velocity version 3.36 gives the thermal broadening, as we only care about the motions along the line of sight. Moving atoms experience a Doppler shift of the incident laser radiation and, the shifted frequency is given by:

$$\nu = \nu_o (1 \pm \frac{v_x}{c}) \tag{3.38}$$

where ν_o is the initial frequency, v_x is the velocity of the atoms in the line of sight and c is the speed of light.

The broadening of the resonance profile from different velocity classes with the incident radiation at different Doppler shifts results in a Gaussian profile described by,

$$\phi(\nu) = \frac{exp - [(\nu - \nu_o)/\Delta\nu_D^2)]}{\Delta\nu_D \sqrt{\pi}} \tag{3.39}$$

where $\Delta\nu_D$ is the Doppler width given by

$$\Delta\nu_D = \frac{\nu_o}{c} \sqrt{\frac{2k_B T}{m}} \tag{3.40}$$

The correspondent full width at half maximum (FWHM), $\Delta\nu_{D-FWHM}$ is given as,

$$\Delta\nu_{D-FWHM} = 2\sqrt{2ln(2)}\Delta\nu_D = \nu_o \sqrt{\frac{8k_B T ln(2)}{mc^2}} \tag{3.41}$$

The Doppler broadening FWHM, calculated from Equation 3.41, for different masses at different wavelengths and temperatures are shown in Figure 3.6. It is quite clear that the Doppler broadening of the linewidth increases with higher temperatures and lighter atoms. The Doppler broadening restrains the linewidth of the resonance profile in the GHz regime and is an extremely limiting factor on the resolution of spectroscopic investigations in hot environments. As the natural linewidths are in the order of a few tens of MHz, the presence of such a broadening effect in terms of GHz must be avoided for high-resolution spectroscopy.

However, if we are working in a hot environment and the goal is to achieve maximum ionization efficiency of the atoms in the said environment, laser systems with spectral bandwidth comparable to the Doppler broadening could be employed. This should allow us to address all the velocity classes of atoms. Using lasers of linewidth around 10 GHz is quite common for the purpose of ion production in laser ion sources to capture Doppler-shifted atoms and ensure higher ion production. However, the use of a much larger linewidth increases the chance

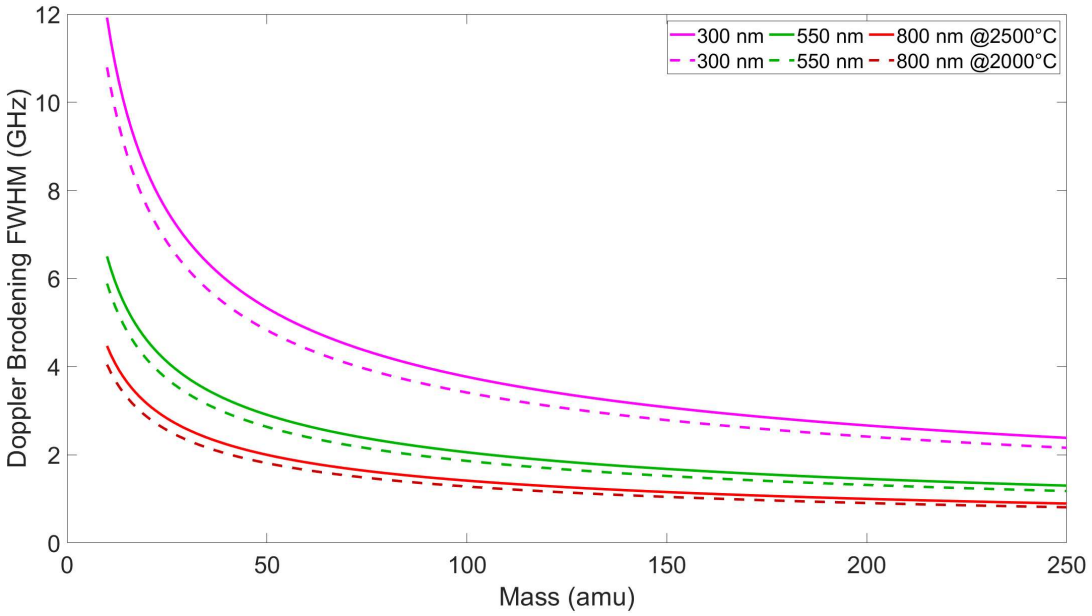

Figure 3.6: Doppler broadening dependence on mass at different wavelengths and temperature.

of probing other nearby atomic lines of other elements, which could compromise the chemical selectivity of the laser ion source.

3.3.3 Power Broadening

When the intensity of the laser approaches or exceeds the saturation intensity of the atomic transition, an additional broadening can be observed. This is known as the power broadening.

Let us consider a two-level system with a center frequency of transition ν_o and Lorentzian natural line profile with FWHM linewidth $\Delta\nu_{nat-FWHM} = 2\gamma$.

Below the saturation intensity, the linewidth is narrow and resembles the natural linewidth of the atomic transition. As the intensity increases and approaches the saturation intensity, the population of the excited state converges towards its maximum value of 50% (in the case of a two-level system).

If the laser intensity is above the saturation intensity, the Lorentzian linewidth increases proportional to the laser intensity. Saturation parameter S_o can be defined as,

$$S_o = \frac{\text{Intensity of the laser}}{\text{Saturation intensity of the transition}} \tag{3.42}$$

The frequency-dependent absorption coefficient $\alpha(\nu)$ has an increase in the

value with respect to the unperturbed absorption coefficient $\alpha_o(\nu_o)$ at resonance ν_o, as the following equation.

$$\alpha(\nu) = \alpha_o(\nu_o)\frac{\gamma/4\pi^2}{(\nu-\nu_o)^2 + (1+S_o)(\gamma/4\pi)^2} \tag{3.43}$$

This results in a new Lorentzian profile with a FWHM linewidth given by,

$$\Delta\nu_{sat-FWHM} = 2\gamma\sqrt{1+S_o} \tag{3.44}$$

It is important to note that the broadening depends on the parameter S_o, which implies also the overall laser power and the focusing of the laser in the interaction region.

3.3.4 Pressure Broadening

The natural linewidth arises because excited states have a finite lifetime. Collisions of atoms with other atoms or molecules randomize the phase of the emitted radiation. If frequent enough, collisions result in a reduction of the effective lifetime of the excited state and hence a larger uncertainty for the emission frequency. This mostly occurs if the atoms of interest are inside a buffer gas maintained at a certain pressure. It causes an increase in the Lorentzian linewidth as represented in Figure 3.7. The resultant broadening of the linewidth is affected by the nature, density, and temperature of the buffer gas.

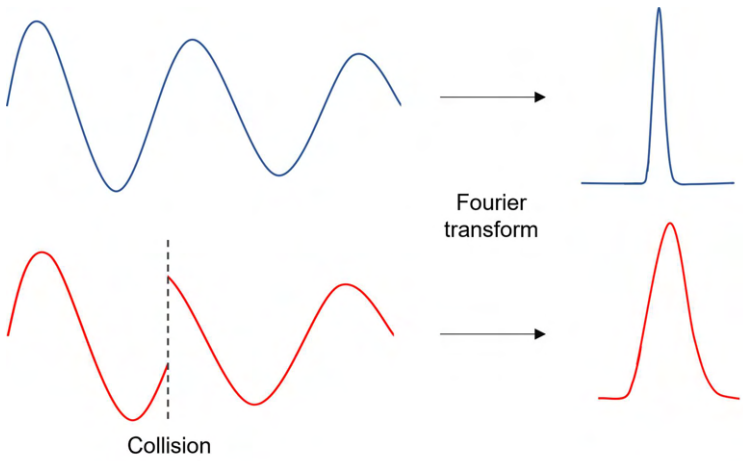

Figure 3.7: Collisions leading to a random phase of the emitted radiation and eventually a broadening of the Lorentzian profile

3.3.5 Voigt Profile

If the centered Lorentzian distribution and Gaussian distribution with profile parameters γ and σ respectively are indicated by L(ν;γ) and G(ν;σ) respectively, the convolution of these two profiles is given by a Voigt profile as,

$$V(\nu;\sigma,\gamma) = \int_{-\infty}^{\infty} G(\nu';\sigma)L(\nu-\nu';\gamma)d\nu' \tag{3.45}$$

where ν' is the shift from the line center.

It is often used in analyzing data from spectroscopy where different contributions to the line profiles are present. The tails of the Lorentzian profile fall off slower than the Gaussian profile, so the core remains roughly Gaussian, while the wings look like a Lorentzian profile.

Full Width at Half Maximum (FWHM) of a Lorentzian profile is $f_L = 2\gamma$ and of a Gaussian profile is $f_G = 2\sqrt{2ln(2)}\sigma \approx 2.355\sigma$.

The FWHM of a Voigt profile can be calculated to an accuracy of 0.02% using the following relation [37]:

$$f_V \approx 0.5346 f_L + \sqrt{0.2166 f_L^2 + f_G^2} \tag{3.46}$$

3.4 Tunable Laser Sources

3.4.1 Principle of a Laser

Laser stands for "Light Amplification by Stimulated Emission of Radiation." It is a device that produces a coherent and low-divergence beam of light through the process of stimulated emission. The principles of laser operation can be summarized as follows:

1. Stimulated Emission: The laser operates based on the principle, which was first proposed by Albert Einstein in 1917. According to this idea, when an atom or molecule in an excited state interacts with an incoming photon matching a decay transition, it can undergo that energy jump to a lower energy state, emitting a second photon that is identical to the stimulating photon in terms of frequency, phase, and direction [24].

2. Population Inversion: In order to achieve laser action, a population inversion is necessary. This means that more atoms or molecules should be in an excited state than in a lower energy state. This can be achieved through different methods, such as optical pumping or electrical excitation, and needs at least a three-level scheme.

3. Pumping Mechanism: The gain medium in a laser needs to be energized to achieve population inversion. This is typically done by providing energy through a process called pumping. Pumping can be achieved using various methods, such as optical pumping (using an external light source), electrical pumping (passing an electric current through the gain medium), or chemical reactions.

4. Optical Feedback: A laser typically consists of an active medium (such as a crystal, gas, or semiconductor), a mechanism to achieve population inversion, and an optical cavity. The optical cavity consists of two mirrors, one of which is partially reflective. The partially reflective mirror allows a small fraction of the emitted light to escape, while the remaining light is reflected back into the cavity. This creates a feedback loop that allows the light to undergo multiple passes through the active medium, resulting in amplification.

5. Gain Medium: The active medium in a laser is responsible for providing the gain required for amplification. Different types of lasers use different gain media. For example, solid-state lasers use crystals or glasses doped with ions, gas lasers use gases such as helium or neon, and semiconductor lasers use semiconductor materials.

6. Coherence: One of the defining characteristics of laser light is its coherence. Coherence refers to the property of light waves being in phase with each other, both in time and space. In a laser, the stimulated emission process automatically leads to the production of coherent light, where the waves have a constant phase relationship. This coherence is also related to the possibility for a laser beam to be focused on a small spot and to have a well-defined wavelength.

7. Monochromaticity: Laser light is highly monochromatic, meaning it consists of a narrow range of wavelengths. This is due to the fact that the stimulated emission process produces light with a well-defined frequency determined by the energy difference between the excited state and the lower energy state.

3.4.1.1 Dye Lasers

Dye lasers are a type of tunable laser that utilize organic dye molecules as the gain medium. These lasers are capable of emitting a wide range of wavelengths, making them versatile tools in scientific research, spectroscopy, and various industrial applications. The working principle of dye lasers involves the excitation of dye molecules, their energy transfer, and the process of stimulated emission. The dye molecules must possess specific properties to function effectively as the active medium, such as a broad absorption spectrum to absorb a wide range of pump wavelengths and an emission spectrum that overlaps with the desired output wavelength [38].

One of the most significant advantages of dye lasers is their broad tunability range (from ultraviolet to infrared regions). They can cover a wide range of wavelengths by selecting appropriate dyes and tuning the cavity length or employing different optical elements [39]. Dye lasers have the potential to achieve relatively high conversion efficiencies when pumped by appropriate light sources. This high efficiency is crucial for practical applications.

3.4.1.2 TiSa Lasers

Titanium-Sapphire lasers, also known as Ti:Sa lasers, are a type of solid-state laser that utilizes a crystal made of titanium-doped sapphire as the gain medium. It was introduced by Moulton in the 1980's [40]. It is highly regarded for its ability to generate ultrafast pulses, high output power, and tunability over a broad range of wavelengths. Ti:Sa lasers have a very broad tuning range in the visible and near-infrared spectrum, typically covering wavelengths from around 650 to 1100 nm, with a peak around 800 nm. This tunability is achieved by adjusting the cavity length and the tuning element in the laser resonator. Ti:Sa lasers are typically pumped by another laser, such as a frequency-doubled Nd:YAG laser or a green laser, as the pumping transition absorbs in the range of 370-670 nm. The pump source provides the necessary energy to excite the titanium ions in the sapphire crystal, resulting in laser emission.

The gain medium of the laser is a single crystal of synthetic sapphire (Al_2O_3) that has been doped with titanium ions (Ti^{3+}). The titanium ions provide the necessary energy levels for laser amplification. The ground state of the Ti^{3+} is coupled to the field and vibrational modes of the sapphire lattice. This coupling introduces a splitting into two continuous vibrational energy bands of sapphire. The two bands can be exploited to host a four-level scheme with rapid vibrational (non-radiative) decay within the bands and a longer-lived lasing transition in between them.

Chapter 4

Photo-Ionization Study of Silver

Due to its therapeutic qualities, the ^{111}Ag isotope is of great interest to the ISOLPHARM project [11]. It decays through a convenient β^- process with a half-life of 7.45 days and an average energy of $\sim$ 360 keV, which equates to a medium tissue penetration depth (1.8 mm).

According to NIST [41], silver has an ionization potential (IP) of 61106.45 cm^{-1} (around 7.6 eV), which can be successfully exceeded by RILIS employing precise laser wavelengths that represent the transitions between the electronic states of the atoms. There are a few well-known methods for photo-ionizing silver that have been employed in facilities including IGISOL[42], TRIUMF-ISAC[43], and ISOLDE[44].

4.1 Possible Resonant Schemes of Silver

These atomic transitions can be combined in various ways to excite the ground-level valence electron beyond the IP. Table 4.1 lists a few options that may offer the route for the resonant photo-ionization of silver [45]. As is visually demonstrated in Figure 4.1 [45], the electron has not yet crossed the IP after the two resonant transition steps. Yet, by absorbing a photon from any of the earlier excitation phases, the electron can be pushed beyond the IP from the highest excited level. With a third non-resonant laser that produces photons with sufficient energy to cross the gap, higher ionization efficiencies could be achieved.

Table 4.1: Possible resonant photo-ionization schemes of silver (wavelength values indicated in vacuum); ground state configuration of Ag is $4d^{10}5s\ ^2S_{1/2}$

First Transition λ (nm)	First Excited level (Term; J)	Second Transition λ (nm)	Second Excited level (Term; J)
		362.514	$4d^{10}8d(^2D;5/2)$
		371.026	$4d^{10}9s(^2S;1/2)$
328.163	$4d^{10}5p(^2P^o;3/2)$	381.205	$4d^{10}7d(^2D;5/2)$
		421.402	$4d^{10}6d(^2D;3/2)$
		466.983	$4d^{10}7s(^2S;1/2)$
		546.707	$4d^{10}5d(^2D;5/2)$
		368.357	$4d^{10}7d(^2D;3/2)$
		384.186	$4d^{10}8s(^2S;1/2)$
338.387	$4d^{10}5p(^2P^o;1/2)$	405.666	$4d^{10}6d(^2D;3/2)$
		447.734	$4d^{10}7s(^2S;1/2)$
		521.059	$4d^{10}5d(^2D;3/2)$

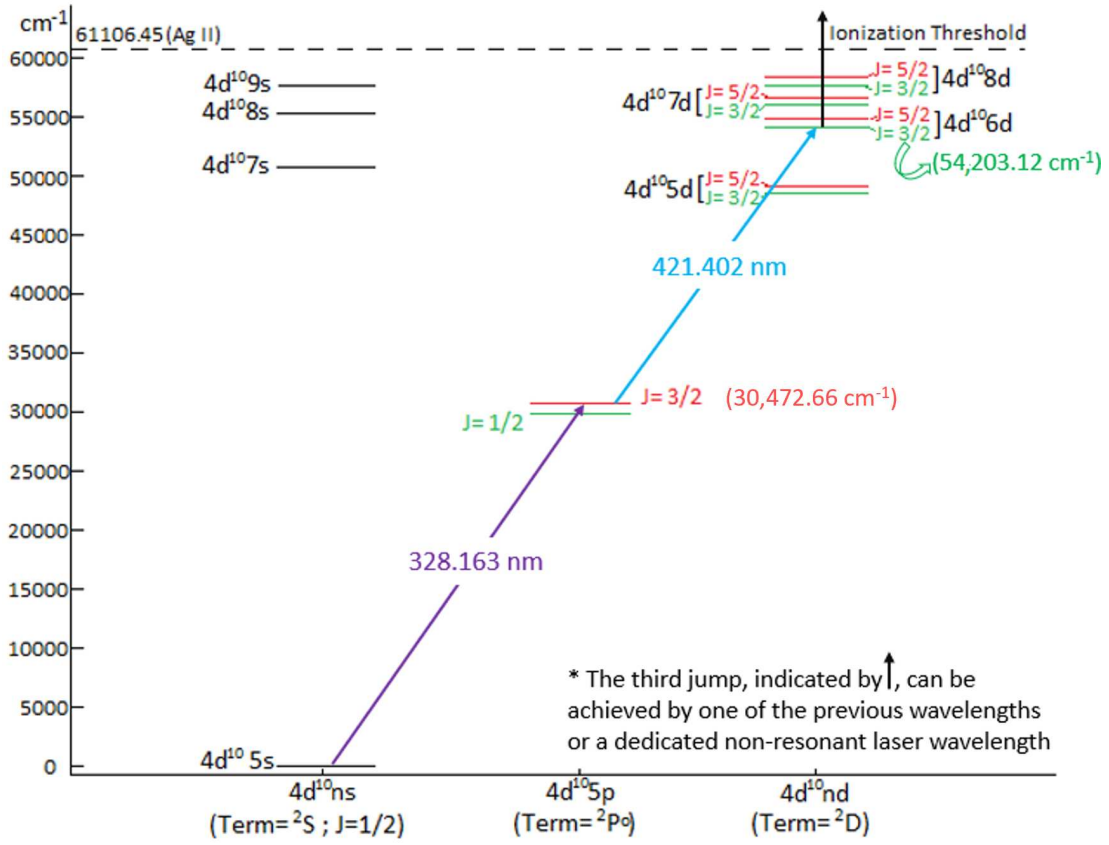

Figure 4.1: Simplified level scheme of silver and applied excitation path. Wavelength values indicated in vacuum.

4.2 Experimental Set-Up

Figure 4.2 shows a schematic sketch of the experimental apparatus that will be described in detail in the following sub-sections.

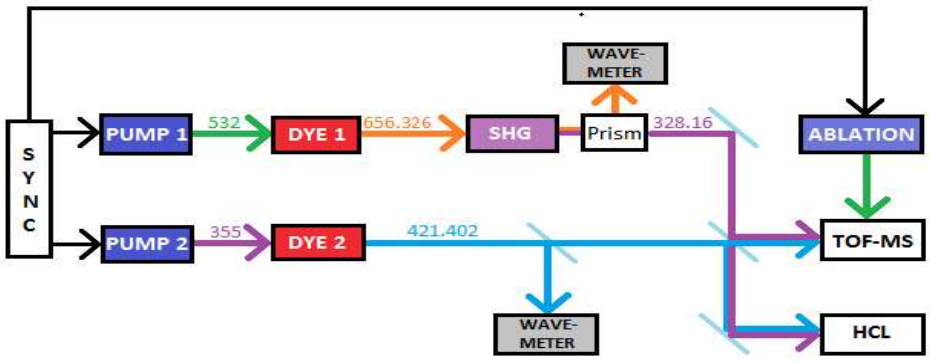

Figure 4.2: Experimental set-up for the laser photo-ionization study of silver. PUMP 1 and PUMP 2 represent the pump Nd:YAG lasers while DYE 1 and DYE 2 represent the dye lasers respectively. SHG is the Second Harmonic Generation crystal, HCL is the Hollow Cathode Lamp and TOF-MS represents the Time of Flight Mass Spectrometer.

4.2.1 Parameters of the Dye-Laser Systems Used

Using dye lasers, both transitional wavelengths are produced. The first step is provided by a Quantel TDL50 dye laser pumped with 532 nm (1.1 W @ 10 Hz) beam from a Quantel YG 580 laser. The used dye solution is Sulforhodamine 640 (0.3 g/L for oscillator and 0.075 g/L for amplifier) with methanol solvent [46]. This dye laser is tuned at 656.326 nm, then the resulting laser beam is frequency doubled with a Second Harmonic Generation (SHG) crystal which produces UV light at 328.163 nm.

A focusing lens can be used to focus the fundamental beam inside the SHG to obtain more power of the UV light. If it is the case, a convenient lens has to be employed later after the SHG to shape the beam in the interaction region. In our case, there was sufficient UV light, so a focusing lens was not employed before the SHG. After the frequency is doubled, the fundamental (656.326 nm) and the second harmonic (328.163 nm) are spatially separated by passing through a prism. The fundamental beam is directed to a High Finesse WS7 wavemeter, which continually monitors the wavelength.

Table 4.2: Parameters of the excitation dye lasers

Laser	**Fundamental**			**SHG**			**Power**	**Pulse length**
	λ (nm)	$\Delta\lambda$ (pm)	$\Delta\nu$ (GHz)	λ (nm)	$\Delta\lambda$ (pm)	$\Delta\nu$ (GHz)	(μW)	(ns)
TDL50	656.326	3-3.5	2.1-2.4	328.163	1.1-1.2	3.0-3.3	20-30	20
FL2002	421.402	1-1.1	1.7-1.9	-	-	-	500-550	20

The second step is provided by a Lambda Physik FL2002 dye laser pumped with 355 nm (0.5 W @ 10 Hz) from a Quantel YG 980. The used dye solution is Stilbene 420 (0.25 g/L both for the oscillator and the pre-amplifier) with methanol solvent [46], and the system is tuned at 421.402 nm. The 2 pump lasers and the ablation laser are synchronized and, therefore, it is possible to optimize experimentally the time delay between the laser pulses. Normally, the time delay is in terms of a few nanoseconds.

A few important parameters of the dye laser systems used for the experiment are listed out in Table 4.2.

It must be noted that the resulting peak amplitude and the FWHM values of the resonance profiles fitted with Voigt function in Section 4.3 and 4.4 are derived with a high level of confidence and a relative error of less than 7%, mainly due to the noisy character of the data.

4.3 Using TOF-MS

In Figure 4.2, TOF-MS stands for Time of Flight Mass Spectrometer which has been set up in the SPES offline laser lab. The details of this system are discussed in [47] and a picture is shown in Figure 4.3. The system is maintained at high vacuum in the range of 10^{-7} mbar and has a flight length of 1.90 m. A Micro Channel Plate (MCP) detector is employed for the collection of the ions.

The TOF-MS is coupled with an Nd:YAG ablation laser (1064 nm) which is directed onto a solid target, and placed inside the TOF-MS housing, to create a vapor of atoms. The excitation lasers are sent orthogonally into the ablation plume and the ions, created as a consequence of photo-ionization in the interaction volume, are directed towards the MCP with the finely tuned ion-optics system, as shown in Figure 4.4.

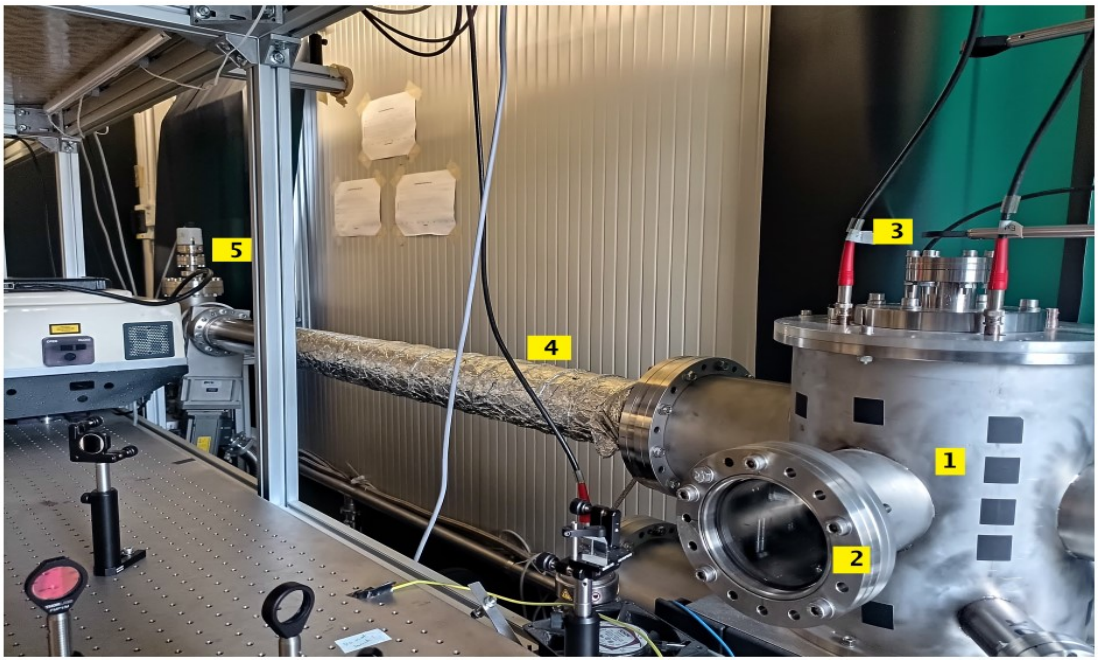

Figure 4.3: The TOF-MS in the SPES offline laser lab. As indicated, 1 is the reaction chamber inside which the target and the extraction electrode system are present. 2 is the entrance window of the excitation lasers and 3 is the entrance window for the ablation laser. 4 is a 1.90-meter-long tube that provides the flight of the extracted ions to the MCP, indicated as 5.

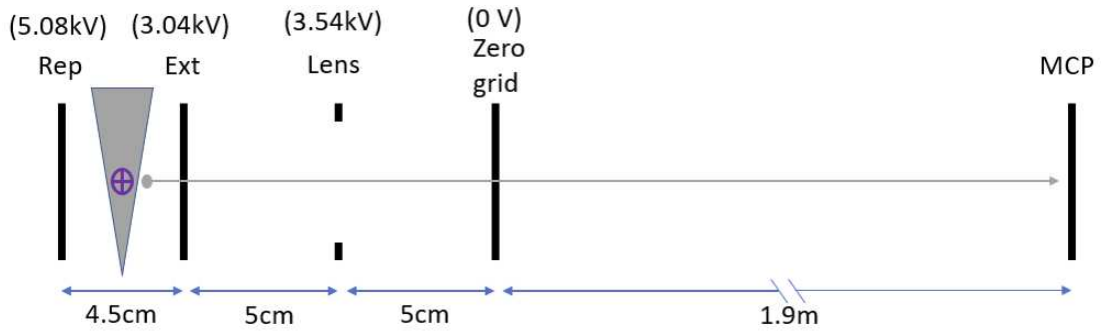

Figure 4.4: A schematic representation of the ion-optics inside the TOF-MS. The four electrodes are: a repeller plate (Rep), an extraction grid (Ext), an electrostatic lens, and a zero voltage grid are indicated. The grey triangle (not in scale) represents an upward expanding conical plume of silver and the purple cross-mark indicates the excitation lasers incident orthogonal to the vertical axis of the plume. The grey dot represents a laser-ionized silver ion which is guided to the MCP with the ion optics.

A SIMION® [48] simulation of the ion path was performed to have an estimate of the optimal electrode voltages and the time of flights of the ions in the given configurations.

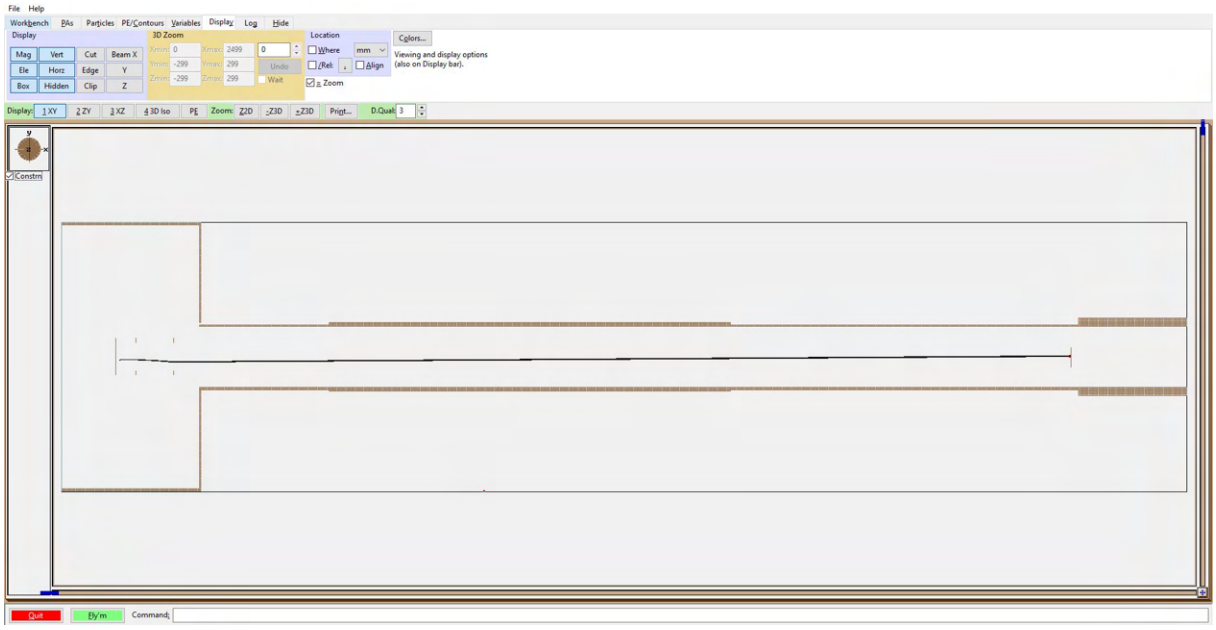

Figure 4.5: SIMION® simulation of the flight of the silver ions with the ion-optics at the indicated electrode voltages in Figure 4.4.

4.3.1 Target and Ablation Technique

The targets used in this experiment were disc-shaped silver targets (5 mm in diameter, 1 mm thick). They were purchased from *Carlo Erba Reagents S.r.l.* The target is 99.9% pure silver composed of the natural abundance 51.83% (^{107}Ag) and 48.17% (^{109}Ag).

Figure 4.6: Solid target of 99.9% pure silver

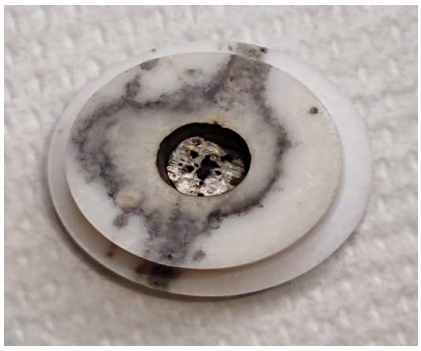

Figure 4.7: Teflon target holder with the silver target

A Quantel YG 980 ablation laser with 20 ns pulses up to 2 J energy at 1064 nm and a 10 Hz repetition rate is used to create an atomic plume from the solid silver target. The ablation pulse is fired on a silver target 30-35 μs before the first excitation laser. This provides an optimal time for the ablation plume to be generated before the excitation lasers arrive at the interaction region. The beam is focused just enough to cover the surface area of the solid silver target. The power of the ablation laser used is 0.8-0.9 W with a spot size of $\sim$ 4.9 mm (power density $\sim$ 4.2-4.7 W/cm^2) on the target surface. The resulting plume is conically expanding with a vertical central axis.

High power of the ablation laser results in the generation of a significant amount of ions in the plume, which is not desirable as we are looking for interaction below the first ionization energy. It also has the potential risk of damaging the MCP as these ablation ions will be deposited on the MCP continuously with high intensity. Therefore, a sufficiently low ablation laser energy level was maintained during the whole experiment.

4.3.2 Experimental Conditions and Results

The signal collected from the MCP was sent to a Tektronix oscilloscope (model: MSO 5204B). The oscilloscope has 4 main working channels which allowed us to see the ablation pulses, the two excitation laser pulses, and the MCP signal. The

data acquisition, the readings of the lambda-meter, and the automatic wavelength scan of the excitation lasers TDL50 and FL2002 are operated through a Matlab program.

4.3.2.1 Isotopic Identification

The TOF signal of silver as collected on the MCP is shown in Figure 4.8. The silver target consists of two isotopes of silver, ^{107}Ag and ^{109}Ag which are detected separately with a satisfying time resolution. In the configuration of the ion-optics described in Figure 4.4, ^{107}Ag and ^{109}Ag are arriving on the MCP at 2.672 μs and 2.698 μs, respectively.

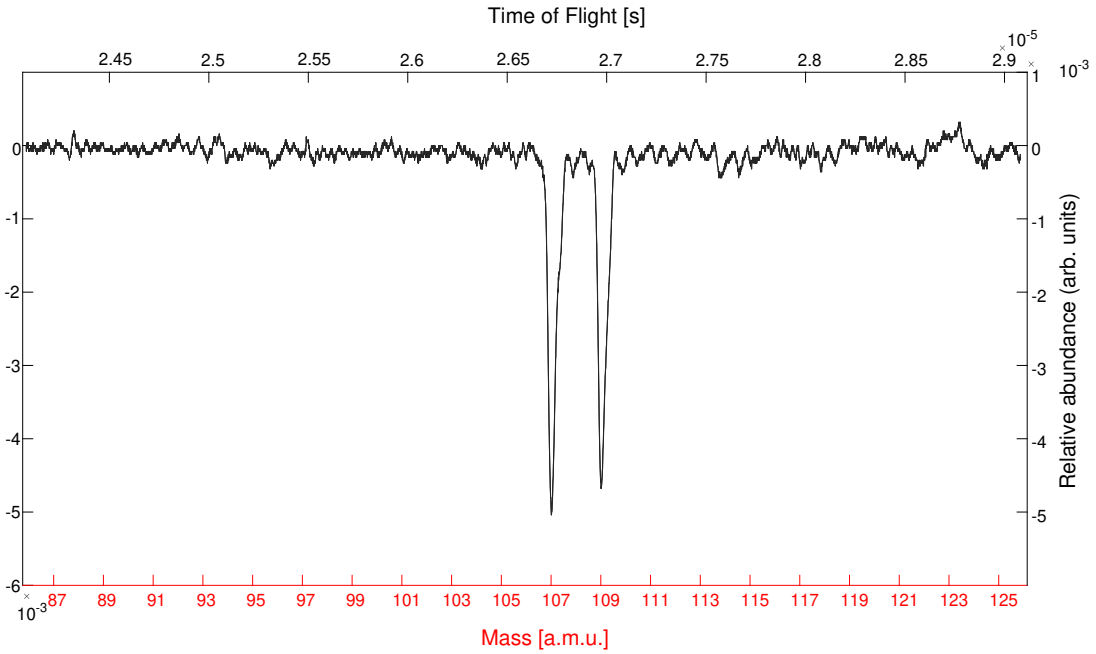

Figure 4.8: Detected TOF signal of silver. The signal is plotted against time (upper x-axis) and against mass (lower x-axis).

4.3.2.2 Doppler-suppressed scheme test

The Doppler broadening arises due to the different velocity components of the atoms in the hot ablation environment. So naturally the key to avoid Doppler broadening is to avoid different velocity components in the given environment. This can be done by probing just a tiny volume inside the plume which will nearly contain single velocity components, if properly interrogated by the lasers.

Both the excitation lasers are directed into the ablation plume in the plane orthogonal to the vertical central axis of the plume. This suggests that only

the horizontal components of the atomic velocities are affected by the Doppler effect. When compared to collinear injection, injecting the excitation lasers non-collinearly to one another unquestionably reduces the volume of the interaction zone by a large factor. In order to choose a group of atoms with almost zero horizontal velocity close to the central axis of the plume, smaller laser beam widths are crucial since they provide a smaller interaction volume. The higher angular separation of the excitation lasers ensures this selection even further.

The size of the laser beams is not small enough to be focused down to achieve the desired small interaction volume. A higher-focusing lens could have provided a smaller depth of focus but an alternative approach is to physically trim the beams before the lenses are used. Iris, with very small apertures, was placed before each focusing lens to achieve this.

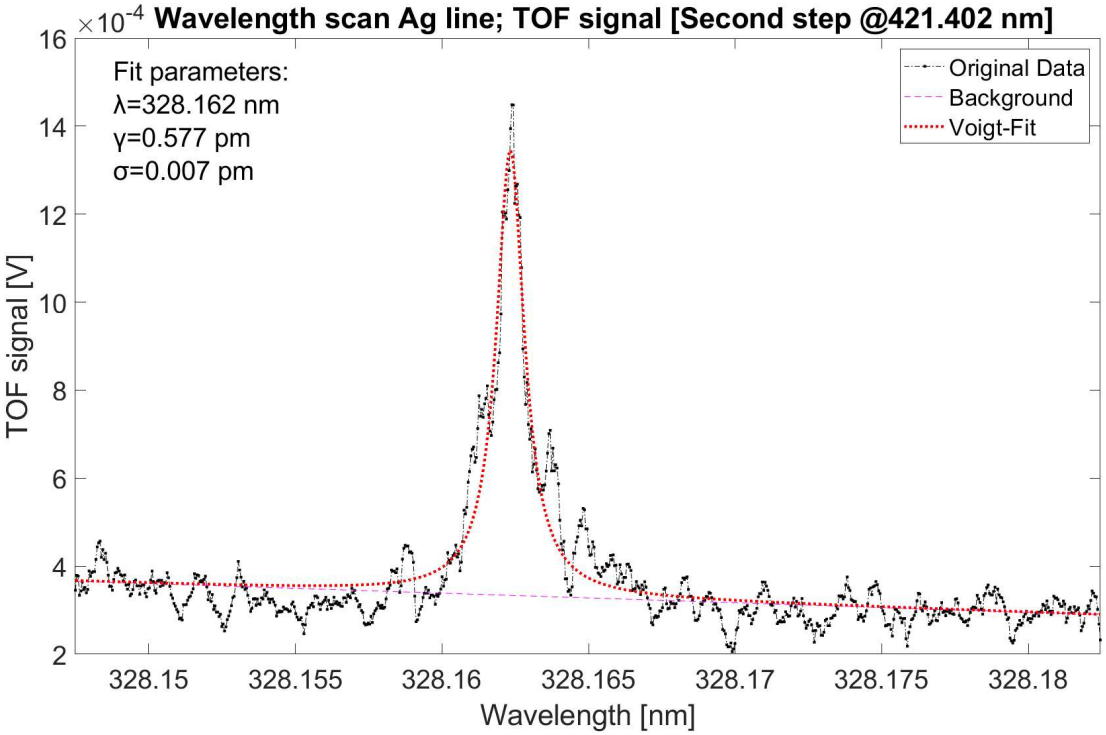

Figure 4.9: 1st transition step Doppler-suppressed wavelength scan $4d^{10}5s^2S_{1/2} \rightarrow 4d^{10}5p\ ^2P^o_{3/2}$. Scanning range = 28 pm (77.9 GHz)

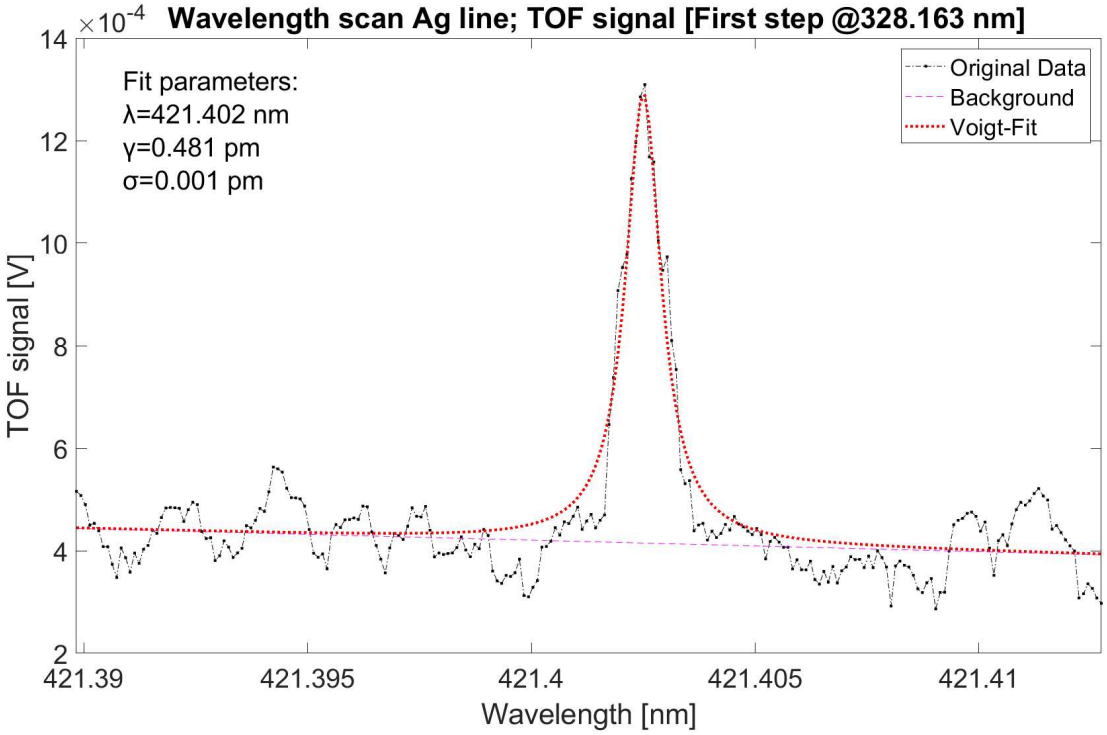

Figure 4.10: 2nd transition step Doppler-suppressed wavelength scan $4d^{10}5p^2P^o_{3/2} \rightarrow 4d^{10}6d\ ^2D_{3/2}$. Scanning range = 22 pm (37.2 GHz)

Consequently, the diameters of the laser beams used to attain the desired interaction volume are 0.6-0.8 mm and 1.0-1.2 mm for the 1st step and the 2nd step transition lasers, respectively.

The angular separation between these laser beams is maintained at $\sim$ 8.5 (eight and a half) degrees and in this configuration, a very small intersection volume, $\sim$ 0.5 mm^3, is achieved inside the ablation plume. This precise selection of the tiny interaction volume allowed us to have a Doppler-suppressed scan of the transition lines in the ablation plume.

Figure 4.9 and Figure 4.10 show clear resonance of the 1st step and the 2nd step at 328.163 nm and 421.402 nm, respectively. The resonance profiles reflect very narrow linewidths of $\sim$ 1.2 pm (3.3 GHz) and $\sim$ 1.0 pm (1.7 GHz). The respective laser profiles with corresponding linewidths (see Table 4.2) are reproduced, showing practically no effect of Doppler broadening.

4.3.2.3 Effect of Laser Linewidth on Doppler Broadening

An effort was made to investigate the Doppler-affected scenario and the impact of the linewidths of the excitation laser lights for the subsequent portion of the experiment.

To study this case, a larger interaction volume containing a higher distribution of the atomic velocities is necessary. The experimental condition changes for these measurements are: a) nearly collinear injection of the excitation lasers and, b) larger beam diameter of the 1st step laser, increased to 1-1.5 mm, from the previous value of 0.6-0.8 mm. These changes create a significantly much larger interaction volume bringing Doppler broadening into the picture.

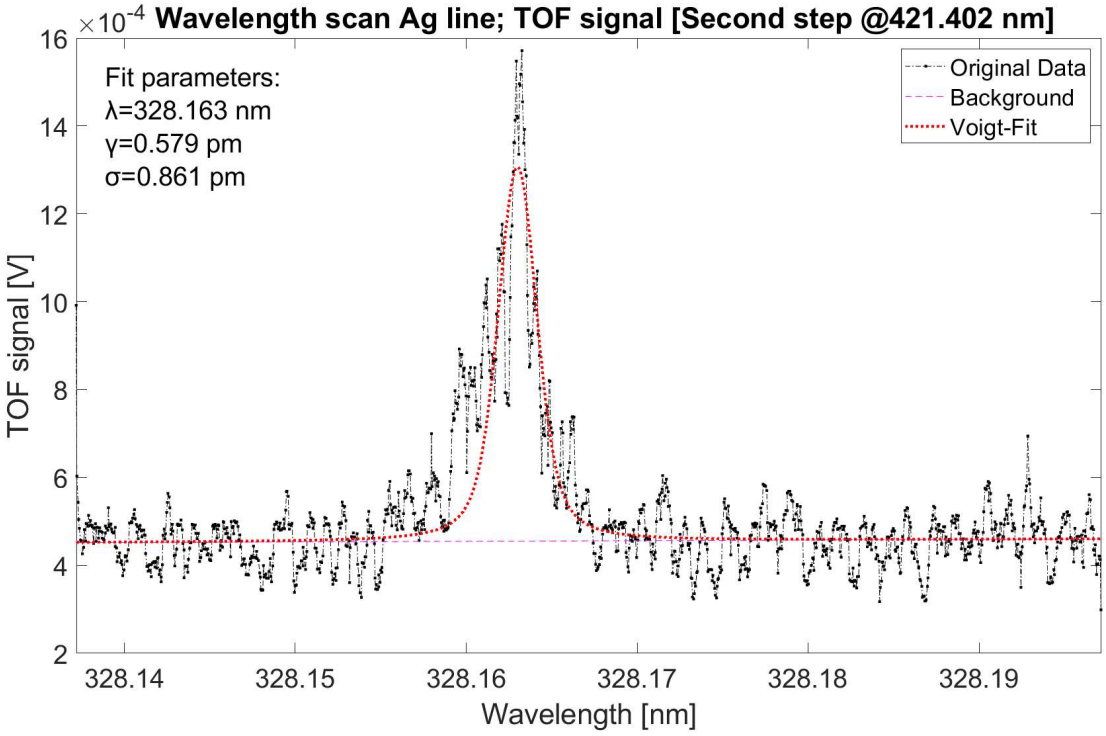

Figure 4.11: 1st step Doppler broadening; scanned with 2nd step laser operating as single-mode laser @421.402 nm. Scanning range = 68 pm (189.3 GHz)

The wavelength scan of the first transition step affected by Doppler broadening is shown in Figure 4.11. As can be seen, the Gaussian contribution has increased to 0.861 pm compared to 0.007 pm in the Doppler-free case shown in Figure 4.9, thereby increasing the linewidth of the resonance profile to $\sim$ 2.7 pm (7.5 GHz) from $\sim$ 1.2 pm (3.3 GHz). This is the frequency range within which Ag^+ ions can be produced in a Doppler-affected scenario, using these laser wavelengths with the given linewidths (see Table 4.2).

The drawback of using lasers with narrow linewidths to produce ions in a hot environment is that many atoms, which are subjected to the Doppler effect, are lost. Large linewidth lasers are utilized for ion production in laser ion sources (LIS) to prevent this loss.

To study this scenario, the pumping power in the dye oscillator of the 2nd dye laser was increased to push the gain of the cavity far beyond the gain threshold. This allowed additional modes to resonate effectively in the oscillator cavity. The pumping power was increased to such a level that not only the extra modes were created in the oscillator cavity but these modes were also power-broadened to provide a practically continuous wide laser profile with an effective linewidth of $\sim$ 10-15 pm corresponding to $\sim$ 16.9-25.3 GHz.

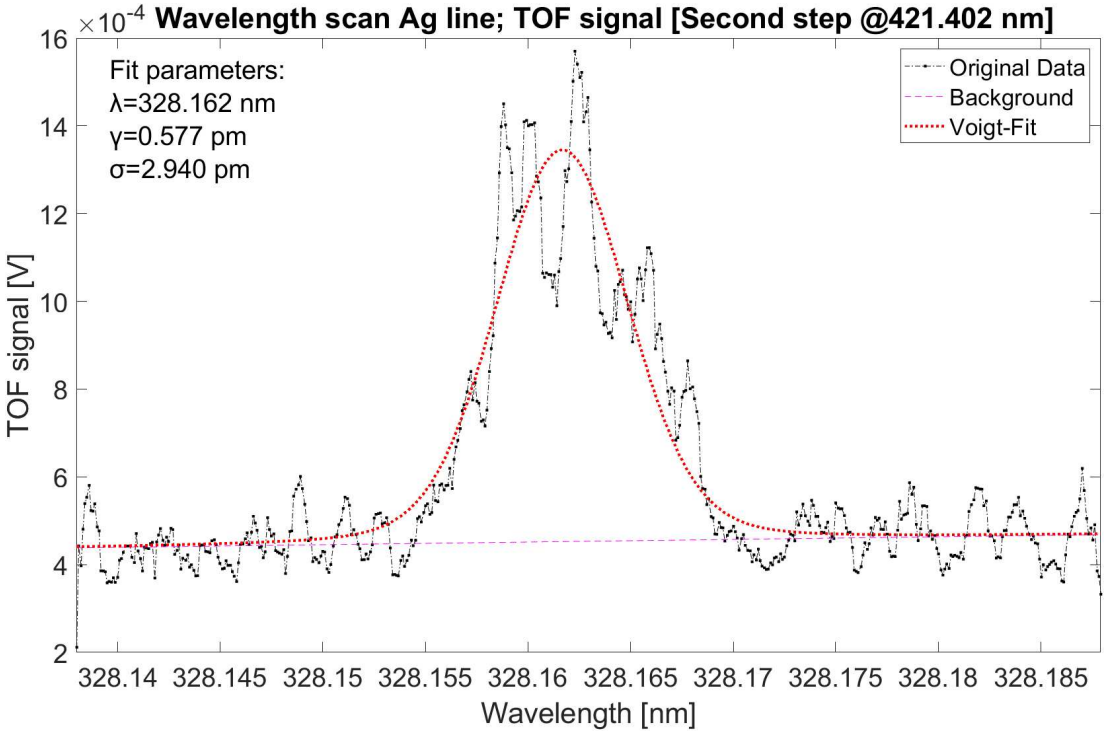

Figure 4.12: 1st step Doppler broadening; scanned with 2nd step laser operating as multi-mode laser with central frequency @421.402 nm. Scanning range= 50 pm (139.2 GHz)

At this stage, by carefully observing the intensity of the ion signal collected on the MCP, the amplification of the laser beam, coming out of the oscillator cavity, was decreased to retain a similar power to the central mode. This procedure was performed to emphasize the effect of the spectral linewidth of the excitation laser light. With this setup, the overall laser power of the 2nd dye laser was 850-900 μW.

The resonance profile of the first-step wavelength scan with the second-step laser retained in multi-mode is shown in Figure 4.12. The linewidth of the profile shows a significant increase to $\sim$ 7.5 pm corresponding to $\sim$ 20.9 GHz. The area under the curve has grown to $\sim$ 3.5 times in comparison to Figure 4.11 showing

a proportional change in the number of ions collected. In other words, the first-step laser would generate an equivalent number of ions by simply operating at its resonant wavelength of 328.163 nm if it had a linewidth of about 20.9 GHz. This is a resounding qualitative confirmation that a broad linewidth of the excitation lasers can cause increased ion production in a hot environment where the Doppler effect is dominantly present.

To capture Doppler-shifted atoms and ensure increased ion production, lasers with linewidths of 10 GHz are frequently used in laser ion sources. However, the use of a much larger linewidth increases the chance of probing other nearby atomic lines of other elements, which could compromise the chemical selectivity of the laser ion source.

4.3.2.4 Fine Structure of the Level $4d^{10}6d\ ^2D$ (J=5/2 and J=3/2)

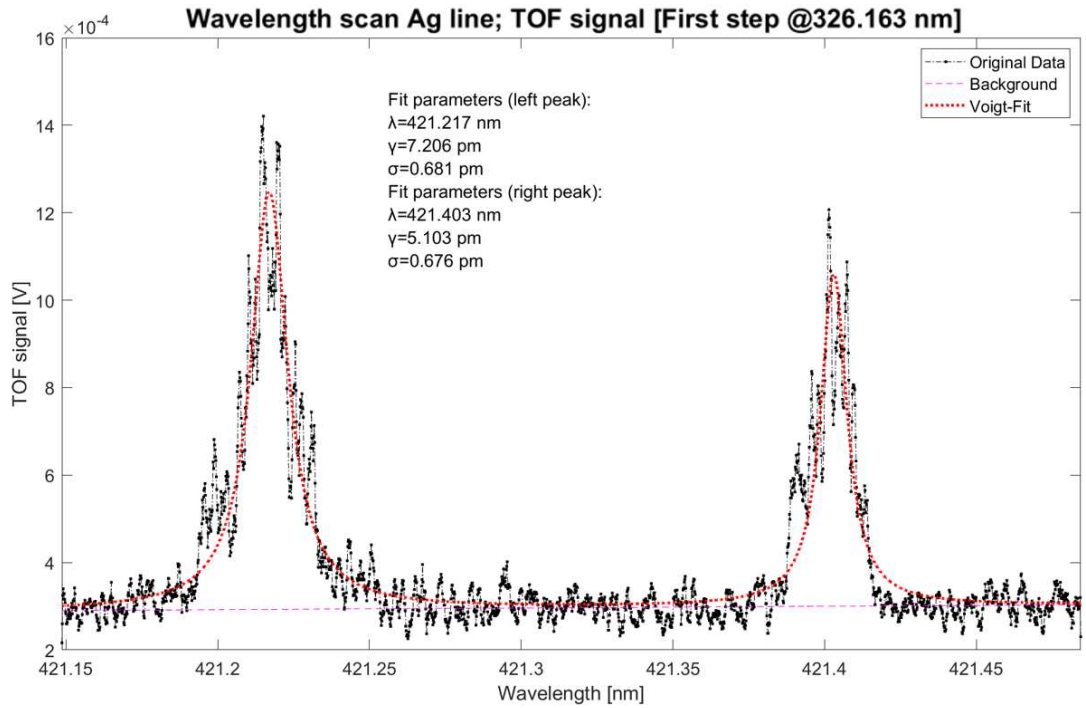

Figure 4.13: Fine structure of $4d^{10}6d\ ^2D$ [J=5/2 (left peak) and J=3/2 (right peak)]. Scanning range= 330 pm (557.4 GHz)

The fine structure split of the Ag-level $4d^{10}6d\ ^2D$ is well depicted in Figure 4.13. The scan reveals resonance peaks at 421.217 nm and 421.402 nm, which, on the left and right, correspond to transitions to J=5/2 and J=3/2 respectively. The fine structures show a split of roughly 186 ±2 pm corresponding to 314 ±3 GHz,

in agreement with the National Institute of Standards and Technology (NIST) database value of 185 pm corresponding to 312.5 GHz [41].

Qualitatively, the left peak has higher intensity and could point to a higher transitional probability of the line. According to this measurement, the 2nd step transition to J=5/2 would be the preferred choice for the production of Ag^+ ions in the SPES facility. However, a quantitative comparison of the relative intensities of the two transitions cannot be made since the stability of the intensity of the ablation plume is not well determined.

The results discussed in Section 4.3 have been published under MDPI-Applied Sciences [45].

4.4 Using Hollow Cathode Lamp (HCL)

For the measurements with the HCL, the laser parameters are the same as indicated in Table 4.2, except that the power of the lasers were much lower, around 10-20% of the values indicated in 4.2.

The primary requirement of a hollow cathode lamp (HCL) is to generate a complete spectrum of the element which has to be studied. HCLs are designed to provide the spectral emission of different elements, characterized by high spectral purity and decent intensity. A HCL usually consists of a glass tube containing a hollow cathode, a ring-shaped anode, and a buffer gas, usually a noble gas. The glass tube has a window made of synthetic silica or UV glass or borosilicate glass.

Compared to parallel plate electrodes, using a hollow platter increases the current density by around 10 times and thus allows for enhancement of the emission intensity and a lower voltage drop in the lamp. The buffer gas is ionized by the voltage across the anode and cathode. The process creates a plasma and the electric field accelerates the buffer gas ions into the cathode surface. The kinetic energy of ion impact causes the cathode material to sputter away from the cathode surface into the vapor phase.

The same electric field causes the electrons to move toward the anode. These electrons collide with the sputtered metal atoms and promote them from the ground state to an excited level. When these excited atoms return to the ground state (which normally takes a very short time in terms of nanoseconds), they emit the monochromatic light characteristics of the metal atoms.

In an ideal situation, the line profile of the emitted radiation exhibits no spectral line broadening other than natural broadening. However several broadening mechanisms are present and observed during the actual operation of the lamp. Broadening mechanisms like Doppler broadening, self-absorption line, pressure broadening, Zeeman effect and Stark effect broadening are present. Self-absorption is an effect when a photon emitted by an atom may be absorbed by a different atom before it escapes from the source. The major broadening mechanisms in a hollow cathode lamp are Doppler broadening and self-absorption lines with distortion.

4.4.1 Silver HCL

A silver HCL is used to study the photo-ionization scheme of silver using the opto-galvanic effect. Figure 4.14 and 4.15 shows the silver HCL in the state “off” and “on” respectively.

The specification of the silver HCL are given below:

- Cathode element: Ag
- Buffer gas: Ar
- Maximum current: 4mA
- Primary emission line: 328.163 nm

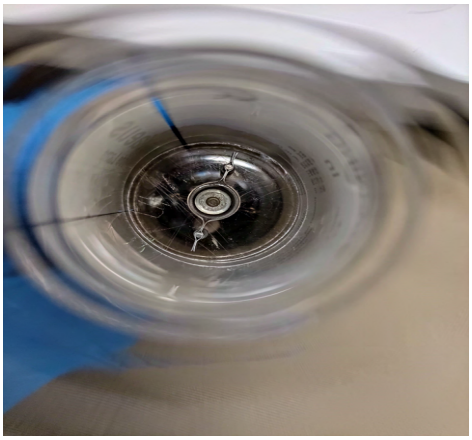

Figure 4.14: Silver hollow cathode lamp turned off

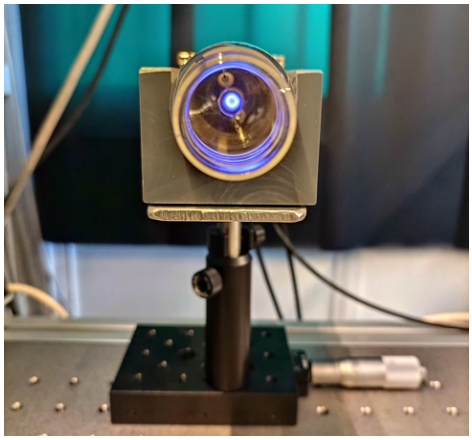

Figure 4.15: Silver hollow cathode lamp turned on

4.4.2 HCL and Opto-Galvanic Effect

Illumination of a gas discharge with resonant radiation causes perturbations of the steady-state populations of two or more levels. Since the collisional ionization rates from various levels are typically not equal, changes in the steady-state populations of bound levels will also affect the discharge's ionization balance. This in turn results in a modification of the electrical characteristics of the discharge. The opto-galvanic effect (OGE) has been described in several ways:

1. a change in the electric field per unit pressure
2. a change in the discharge current
3. a change in impedance of the gas discharge

Depending on the kinetics of the levels whose populations are perturbed by the laser, the OGE can correspond to an increase or decrease in discharge current. An increase in the discharge current and a drop is observed if the resonant laser excites the atom from a level with a low probability of ionization to a level with

a higher probability of ionization. On the other hand, if the laser excites the atom from a level with a high probability of ionization to a level with a lower probability of ionization, the opposite effect is observed on the OGE signal.

With opto-galvanic detection, an optical transition can be easily observed without the use of any traditional optical detectors because the gas discharge serves both as a spectroscopic sample and a detector. The effect was used for spectroscopy purposes for the first time in 1976 [49]. The OGE signal can be considered proportional to the intensity of the resonant radiation [50]. The change in the discharge properties due to interaction with the resonant laser radiation is small. Therefore analysis of the OGE signal is a good alternative to the absorption spectroscopic technique particularly in the detection of weak transitions [51]. Plotting the intensity of OGE signals against the wavelength values can provide the resonance profile of the element.

It may be challenging to provide a complete set of rate equations for all the levels and processes involved in the discharge, which makes it difficult to provide a detailed quantitative description of the opto-galvanic effect. However, a qualitative explanation of the OGE signals is fairly straightforward.

Most refractory elements can be investigated most effectively in a hollow-cathode discharge, where ions interacting with the cathode remove atoms off the cathode by sputtering, making the material accessible to gas-phase optical spectroscopy. Opto-galvanic spectroscopy offers the simplest method for examining these materials as they are already a part of a gas discharge.

For determining spectroscopic data, opto-galvanic spectroscopy offers a significant alternative to fluorescence or absorption studies. Absorption spectroscopy is only possible on samples with an optical density high enough to have a detectable absorption of the incident energy. The fluorescence studies, on the other hand, could be used to study samples with low absorption. However, there are certain limitations to this technique as well. Some of the limitations include:

1. If there are multiple decay channels and there is just one convenient wavelength that can be detected.

2. If the decays primarily occur through non-radiative processes.

3. If the fluorescence is at a wavelength difficult (like deep UV) for optical detection.

The opto-galvanic spectroscopy overcomes these difficulties and provides a sensitive technique for studying optical transitions and determination of the transition frequencies.

Based on the mechanism of the origin of the OGE signal, two kinds of signals are observed in a hollow cathode lamp when resonant radiation is irradiated [52]. They are termed "slow signals" and "fast signals".

Slow signals

The steady-state population of bonded atomic or molecular levels changes as a result of the laser radiation being absorbed in the discharge. Even if laser photons from a pulsed beam do not directly ionize the atoms, they still alter population levels. A perturbation to the steady-state situation results in a net change in the discharge current, or alternatively, a change in the discharge impedance, because various levels have different ionization cross-sections or ionization probabilities.

The energy excess is then redistributed by the collisions, leading to slower ionization events and, ultimately, modifying the characteristics of the discharge in a period of time less than that elapsed between two successive laser pulses. The measured electrical signal lasts for a few microseconds (μs) and is usually negative.

Fast signals

When atoms or molecules are excited by a laser to higher electronic states, the equilibrium between the electronic temperature and the atomic excitation temperature is disturbed. The superelastic collisions between the laser-excited atoms and the electrons in the discharge, however, immediately tend to re-establish the equilibrium. In this process, a large amount of extra energy is released, which often causes the electron temperature of the discharge to rise. Therefore, the conductivity or impedance of the discharge increases as a result of the resonant excitation of the atoms by the laser.

A fast electric signal is generated when a direct ionization in the discharge is caused by the laser pulse. The fast signal has a duration in the order of nanoseconds (ns) since it exhibits the same temporal behavior as a laser pulse. Unlike the slow signal, the fast signal is usually positive.

4.4.3 Wavelength Scan with Slow Signal

The slow signals acquired from the silver HCL are shown in Figure 4.16. In this case, the signals last roughly 15-20 μs. Plotting the intensity (magnitude) of these slow signals against the wavelength gives us the resonance profile for the corresponding transition steps.

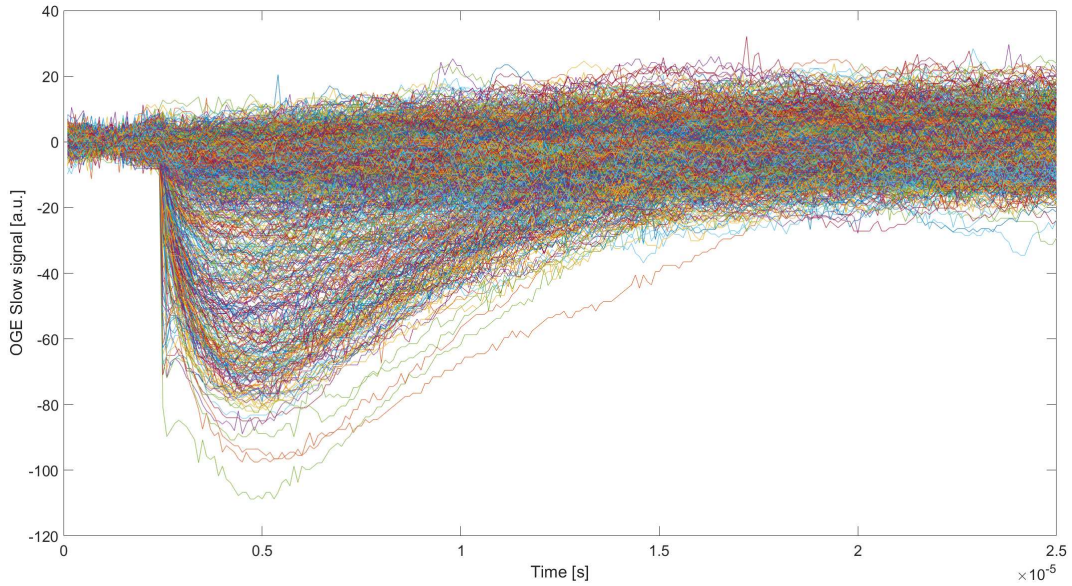

Figure 4.16: Slow signal acquired from the silver HCL.

4.4.3.1 Irradiating just the first transition laser

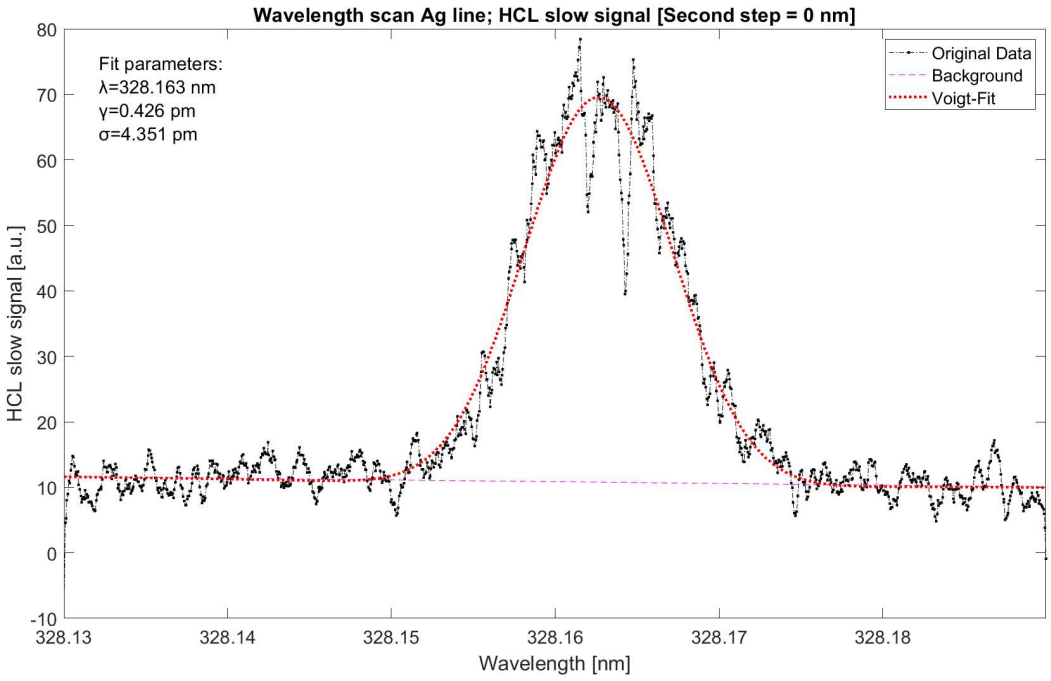

Figure 4.17: 1st transition step wavelength scan $4d^{10}5s^2S_{1/2} \rightarrow 4d^{10}5p\ ^2P^o_{3/2}$. Scanning range= 167 GHz.

Figure 4.17 shows the resonance profile of the first-step transition of silver using a laser of wavelength value 328.163 nm. The resonance exhibits a very wide profile with a linewidth of approximately 30 GHz. Doppler broadening is not sufficient to explain the broadness of this profile.

4.4.3.2 First transition laser and the second transition laser together

Now, keeping the first laser at the resonance wavelength of the first transition, the second laser is added to the interaction region spatially and temporally. What it does is, it creates a more intense slow signal when the second laser is in resonance with the system.

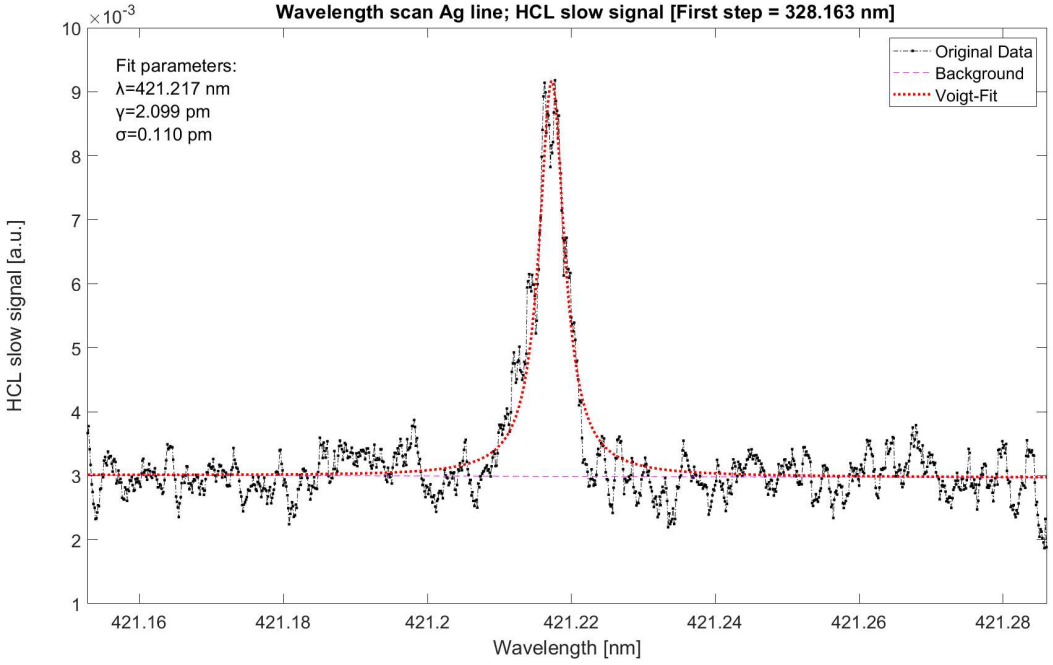

Figure 4.18: 2nd transition step wavelength scan $4d^{10}5p\,^2P^o_{3/2} \rightarrow 4d^{10}6d\,^2D_{5/2}$. Scanning range=220 GHz.

Having set the first transition laser fixed at 328.163 nm, a wavelength scan is performed with the second laser. Taking the slow signal of the first transition laser as the reference point, the intensity (of the slow signal) versus the wavelength of the second laser is measured. The result is plotted in Figure 4.19, which shows a very clear resonance at 421.217 nm for the second transition. The resonance profile is roughly 7 GHz wide, which could be the consequence of Doppler broadening inside the HCL.

4.4.4 Wavelength Scan with Fast Signal and Evidence of High-lying Rydberg States

The fast signals, as described previously, have a temporal behavior like the laser pulses (20 ns for the laser systems used in this experiment). Figure 4.19 shows the acquired fast signals from the silver HCL. Unlike the slow signals which show every resonance effect, fast signals are created as a result of direct ionization processes only.

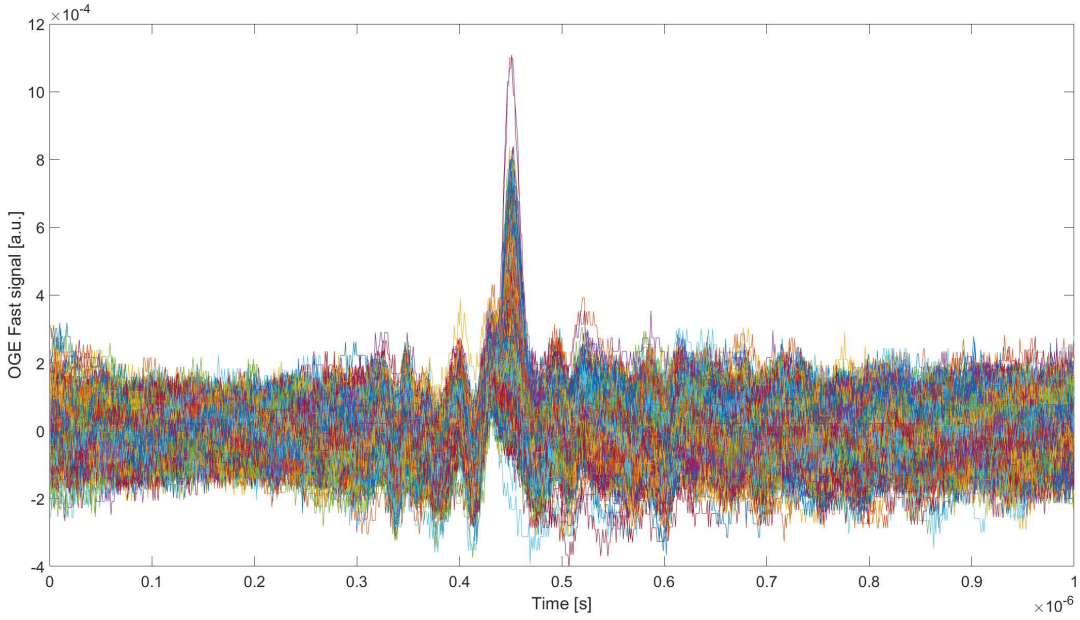

Figure 4.19: Fast signal acquired from the silver HCL.

Plotting the intensity of the fast signals against the laser wavelength gives us the resonance profile around the first transition wavelength, shown in Figure 4.20. The resonance profile has a width of approximately 35 GHz.

In the silver HCL, the prominent emission line is also at 328.163 nm, which means that there is already an abundant amount of atoms in the corresponding excited state $4d^{10}5p\ ^2P^o_{3/2}$. So there is a possibility that apart from the ground state silver atoms, these excited atoms are also absorbing the laser photons. If this is the scenario, it means that there are resonance transitions to levels with an energy value twice the energy of a 328.163 nm photon. Another possibility is the double absorption of the laser photons at 328.163 nm.

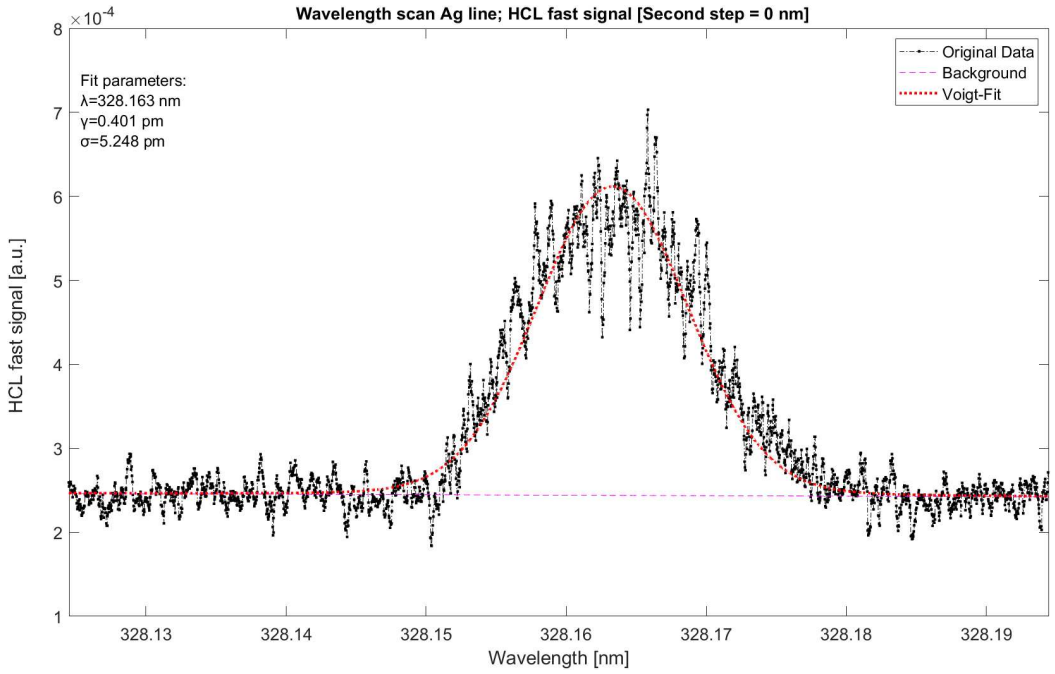

Figure 4.20: 1st transition step wavelength scan $4d^{10}5s^2S_{1/2} \rightarrow 4d^{10}5p\ ^2P^o_{3/2}$. Scanning range=195 GHz.

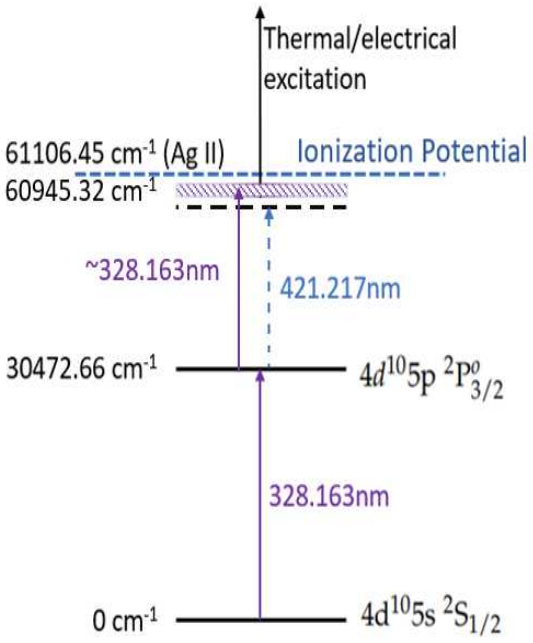

Figure 4.21: Simplified resonant scheme of silver with dense Rydberg states (purple dashed region).

As the energy of a photon at 328.163 nm is equivalent to 3.78 eV (30472.66

cm^{-1}), there is the possibility of the existence of levels around 7.56 eV (60945.32 cm^{-1}). These energy levels would be then very close to the IP of silver whose value is 7.58 eV (61106.45 cm^{-1}). Such energy levels are termed as Rydberg states.

As the fast signals are observed just with the one laser at 328.163 nm, it means that silver ions are created in the HCL. This is possible as the Rydberg states are highly affected by the electric field around the cathode. Once the electrons are populated in the Rydberg states, they can cross the IP with thermal/electrical excitation inside the HCL.

The results discussed in Section 4.4 have been presented in 6th International Conference Frontiers in Diagnostic Technologies and published as a proceeding with JINST [53].

The dye laser used in this experiment had a linewidth of around 3 GHz. Using lasers of finer linewidth should allow us to distinguish these Rydberg states.

Chapter 5

SPES Laser Ion Source test at Offline 2-ISOLDE, CERN

5.1 Hot Cavity RILIS

A very efficient and widely implemented use of laser ion sources is a hot cavity RILIS, pioneered at PNPI Gatchina and CERN [54, 55]. This type of ion sources is particularly attractive because it combines the intrinsic elemental selectivity of resonance laser ionization, high ion production efficiency (typically >10%), as well as robustness of construction required for production of radioactive ion beams at ISOL facilities [22, 30, 55, 56, 57].

In this technique, typically, pulsed laser beams are overlapped in time and in space along the axis of the hot cavity of a tubular surface ion source. A "thermal plasma" is formed in the hot cavity as a result of the presence of ionized atoms and the thermionically emitted electrons from the heated walls. This plasma has a negative potential with respect to the wall of the cavity and thus confines the ions inside the volume of the hot cavity [18, 58].

In section 3.2.1, the calculation of surface ionization efficiency from a hot surface is discussed. However, in a hot cavity, the observed surface ionization efficiency is much higher than the values calculated using Equations 3.25 and 3.26.

This is due to the multiple atom-wall collisions in the hot cavity which provides a larger chance for the atoms to be ionized. Once the ions are formed, they are trapped by the thermal plasma and therefore protected until the point of extraction. This is an effect of the hot cavity. This enhancement in the ionization efficiency value is interpreted in terms of an amplification factor N [18], which in turn consists of the mean number of wall collisions and effective ion survival

factor. Therefore, for a hot cavity the effective ionization efficiency value β_c can be calculated as,

$$\alpha_c = \alpha \cdot N \tag{5.1}$$

$$\beta_c = \frac{\alpha_c}{1+\alpha_c} = \frac{\alpha \cdot N}{1+\alpha \cdot N} = \frac{\beta \cdot N}{1-\beta(1-N)} \tag{5.2}$$

The electron density n_{es} along the walls, which induces the negative potential for ion confinement in the volume of the cavity, is expressed by the Richardson equation:

$$n_{es} = 2\left(\frac{2\pi m k_B T}{h^2}\right)^{3/2} exp\left(\frac{-\phi}{k_B T}\right) \tag{5.3}$$

From Equations 5.1, 5.2 and 5.3, it can be clearly deduced that a cavity material of lower work function ϕ will provide lower surface ionization and, at the same time, better ion confinement at a given temperature compared to materials of higher ϕ due to the increased thermionic emission of electrons. Materials of lower work function are, hence, favorable for higher performance of hot cavity RILIS [59], provided sufficient robustness at desired operation temperatures.

The SPES laser ion source is made of tantalum which has a lower work function value of 4.28 eV, compared to other materials such as tungsten (4.54 eV) and rhenium (4.96 eV), which can also operate at high temperatures above 2000 K and are typically used for surface ion sources. The work function values are taken from [60].

SPES Laser Ion Source (SPES-LIS)

As with most hot cavity laser ion sources, the SPES-LIS also works by introducing frequency-tuned laser beams into the volume of the ion source from the ion extraction side. The SPES-LIS is based on the surface ion source reported in [61]. It is a 33 mm long tubular hot cavity made of tantalum, with an internal diameter of 3.1 mm and an external diameter of 5.1 mm. The ion source is connected to the transfer line, whose other end is connected to the production target. The transfer line is a tantalum tube, approximately 70 mm long, and has an internal diameter and external diameter of 8 mm and 8.8 mm, respectively. For this offline test, no target container was present and the atom samples were introduced at the beginning of the transfer line via two independent resistively heated tantalum capillaries.

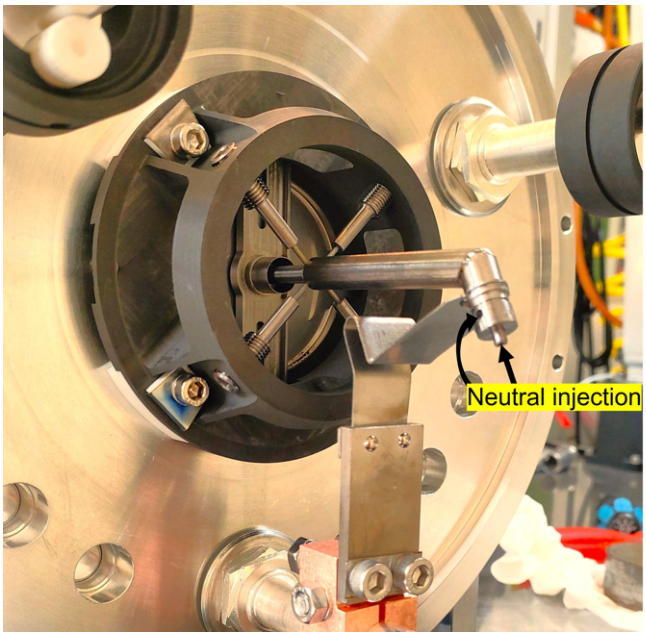

Figure 5.1: The SPES Laser Ion Source, the transfer line, and the hot-cavity alignment system.

An important feature of the SPES-LIS is the "hot-cavity alignment system". It is a circular graphite frame around the junction point of the ion source and the transfer line. It has four centering pins, made of tungsten, ensuring an axial alignment of the hot cavity as shown in Figure 5.1.

This alignment system helps in mitigating the effects of thermal expansion. Having the hot cavity and the transfer line aligned in this way is expected to positively influence the laser ion production by maintaining a mechanically stable laser-atom-interaction volume. In the absence of such a system, the interaction volume could be reduced if there is a tilting of the ion source or the transfer line due to thermal deformation.

5.2 Experimental Set-up

The experiment was performed at the ISOLDE Offline 2 facility [62, 63, 64] in CERN, Geneva. A simplified schematic representation of the experiment is shown in Figure 5.2. The hot cavity laser ion source was installed on a high-voltage platform at a potential of 30 kV. The collimated laser beams entered the beamline under vacuum through a quartz window in the vacuum chamber of the mass-separator dipole magnet. An electrically controlled shutter is placed in front of the window to facilitate the blocking and unblocking of the laser beams during

the experiment.

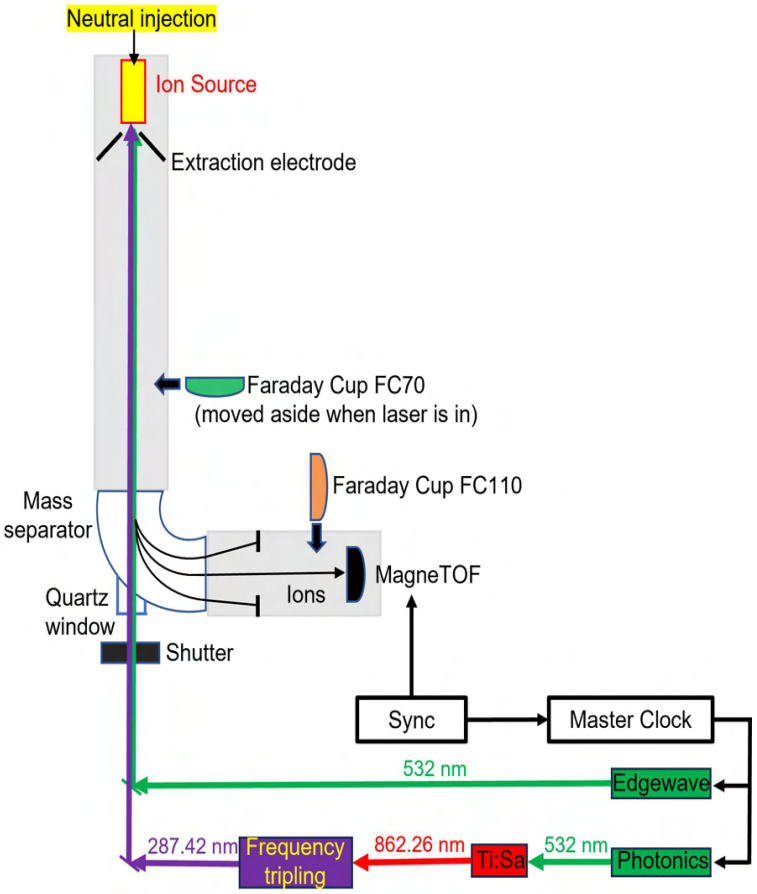

Figure 5.2: Schematic representation of the laser system, the laser ion source and the mass-separator, and the MagneTOF^{TM} detector used for time-structure measurement.
For laser enhancement and ionization efficiency measurements, a Faraday cup is used in place of the MagneTOF^{TM}.

The laser beams were focused through the extraction electrode orifice into the ion source. The ions generated in the ion source are extracted anti-collinearly with respect to the laser beam. The singly charged ions are accelerated to 30 keV in a 90-degree field sector dipole magnet. The isotope-purified beam after the magnet is directed either to a MagneTOF^{TM} detector [65] or a Faraday Cup, depending on the measurement which is being conducted.

An additional Faraday Cup is available before the mass separator magnet, in order to read the total ion current from the ion source in the "laser off" condition.

5.2.1 Modes of Measurements

In order to characterize the laser ion source, three different kinds of measurements were performed: ion beam time structure, laser enhancement of ion yield, and ionization efficiency.

Time Structure Profiles

The lasers utilized for resonance ionization are typically pulsed at repetition rates of 10 kHz, with pulse lengths in the tens of ns range. This rate ensures that each atom interacts with at least one laser pulse during the time it resides inside the cavity. It is considered to be a good compromise between achieving enough pulse energy to saturate atomic transitions and the number of laser-atom interactions for a typically achievable value of average power. The simultaneous creation of ions all along the ion source volume by a laser pulse leads to a periodic modulation of the extracted ion beam, governed by the source-internal extraction mechanisms. Therefore, the resulting time structure of the ion beam can give information about the ion source environment.

To obtain such time structures, a MagneTOF^{TM} detector in single ion counting mode is used to investigate the isotope beam after mass separation. The readout is synchronized with the trigger of the laser pulses. The single ion counts on the detector were used to create a histogram of ion arrival times with respect to the trigger of the laser pulses, as registered by a Cronologic TimeTagger4 acquisition module, described in [63]. To avoid time-overlap of the extracted bunches, a laser repetition rate of 5 kHz was employed, thus the temporal window for each profile is 200 µs. Multiple hundred thousand laser pulses and the produced ions are registered to obtain an averaged time structure for each operational setting of the ion source.

Laser Enhancement Ratios

For a hot cavity laser ion source, the production of ions through surface ionization is unavoidable. The ratio of the ions produced by the laser interaction (laser ions) compared to the ones produced by the surface ionization (surface ions) determines the selectivity of the laser ion source.

During these measurements, the isotope-specific (mass-separated) ion current value is recorded with the ionizing laser beams sent into the ion source cavity and repeated after blocking the lasers. The ratio of the former to the latter gives the laser enhancement ratio (LER). For these measurements, a Faraday Cup is

introduced just in front of the MagneTOF^{TM} detector to read the instantaneous isotopic ion current.

Ionization Efficiency

The measurements of ionization efficiency were performed using the procedure described in the following sections. A calibrated sample of a precisely known quantity of atoms is used to inject the atoms gradually into the ion source, while the ionization process is running, and produced ion current is continuously measured until the total exhaustion of the sample. At the end of the measurement, the total number of detected ions is deduced from the time-integration of the ion current measurements. The ratio of this number to the initial number of atoms in the sample gives the ionization efficiency value.

It is important to note that, for laser ion sources, the efficiency depends on a variety of factors: sample volatilization and atomization, the employed ionization scheme, the extraction, transport, and detection efficiency. All of these factors can independently change, giving rise to overall efficiency differences when employing the same laser ionization scheme at different mass separator facilities.

5.2.2 Sample Preparation

The samples were introduced into capillaries made from tantalum. By attaching these capillaries to the back of the transfer line and gradually heating them, a supply of neutrals into the ion source is ensured.

Gallium (Ga) has two stable isotopes: ^{69}Ga and ^{71}Ga with natural abundances of 60.11% and 39.89%, respectively. A solution of gallium in 5% HNO_3/tr. HCl, of known concentration (1 µg of Ga/µL), was used to produce the Ga sample used for the measurement. Assuming 100% conversion to singly-charged ions, 1 µg of Ga atoms would correspond to the total charge of 380 nAh in both isotopes. The original solution of 1 µg of Ga/µL was diluted 100 times giving a new concentration of 0.01 µg of Ga/µL. A single drop (of 10 µL) would now contain 38 nAh of Ga. For efficiency tests, gallium samples of 76 nAh and 114 nAh were used, which correspond to 20 µL and 30 µL, respectively, of the final diluted solution.

Drops of the solution were put on a small piece of tantalum foil and left to dry. Once the solution was dried completely, the foil was folded and inserted into the narrow capillary of the sample reservoir. After the sample was inserted (just a few mm into the capillary), the capillary was tightly squeezed on one end and the other end was connected to the transfer line. Gradual heating of the tantalum

capillary leads to evaporation of the gallium sample and release of the gallium atoms into the ion source via effusion. The flux of atoms was regulated by the heating current using a dedicated power supply.

For the laser enhancement and time structure measurements, excess gallium samples (roughly 7600 nAh) were used. In this case, around 20 µL of the original concentration of the solution was used.

It is essential to understand how the laser ion confinement and the selectivity are affected by the presence of other ions (impurities) [58, 18]. For this purpose, an additional sample of barium (Ba) was attached to the transfer line. As barium is efficiently surface-ionized at high temperatures, it can be used to independently manipulate the ion load in the ion source.

5.2.3 Photo-Ionization Scheme of Gallium and the Laser System

The photo-ionization scheme used during this experiment in order to laser ionize the gallium atoms [66] is shown in Figure 5.3.

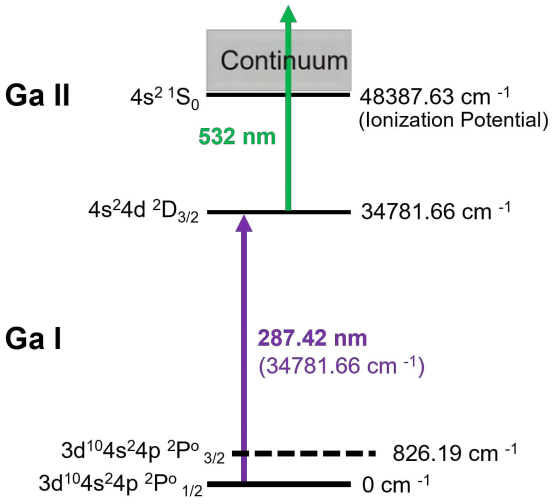

Figure 5.3: Photo-ionization scheme of gallium used for ionization from the atomic ground state. The dotted line indicates the first thermally excited state.

To produce the wavelengths required for the indicated scheme, titanium:sapphire (Ti:Sa) laser [67] was used and the generated fundamental light was subsequently frequency tripled to 287.422 nm. For non-resonant excitation into the continuum, a single mode frequency-doubled Edgewave PX200-2-GF-SLM laser (for the 532 nm) was used.

The Ti:Sa laser was pumped with a frequency-doubled Nd:YAG laser Photonics DM60 operated at a power of 11-11.5 W. A HighFinesse/Angstrom WS6-600 wavelength meter was used to continuously monitor the fundamental wavelength of the output of the Ti:Sa laser. The Ti:Sa laser was tuned to produce a fundamental IR laser output at 11593.89 cm^{-1} (862.264 nm). The output fundamental beam was sent to the frequency tripling unit where the desired, resonant laser beam at 34781.66 cm^{-1} (287.422 nm) was generated. After passing through a telescope of cylindrical lenses, the beam was sent to the ion source. The power of the UV beam was maintained at around 100 mW before the vacuum entrance window of the mass separator, which is sufficient for the saturation of the electronic transition.

The power of the green beam applied for the non-resonant step was around 20 W at the vacuum entrance window, except during the time structure measurement where power was reduced to limit the number of ions produced to stay within the safe operation regime of the detector. The green laser beam was sent to the ion source after passing through a telescope of spherical lenses. The delay of the green laser pulses with respect to the UV laser pulses was electronically adjustable and optimized according to the ion-current readout.

5.3 Measurement Sessions and Results

5.3.1 Thermal-Electrical Characterization

Before the SPES ion source system was mounted on the front-end high-voltage platform, calibration of the ion source temperature with respect to the heating current was performed. The ion source heating was obtained by applying a DC current from the beginning of the transfer line (where neutrals are injected, see Figure 5.1) up to the exit of the hot cavity.

Figure 5.4 shows the various calibration cycles performed and the temperature reading from an inner point of the ion source against the heating current. A filament pyrometer, aligned close to the mid-point of the hot cavity, was used to take the temperature readings. The ion source showed a very reproducible thermal behavior during the heating and cooling cycles of the measurement.

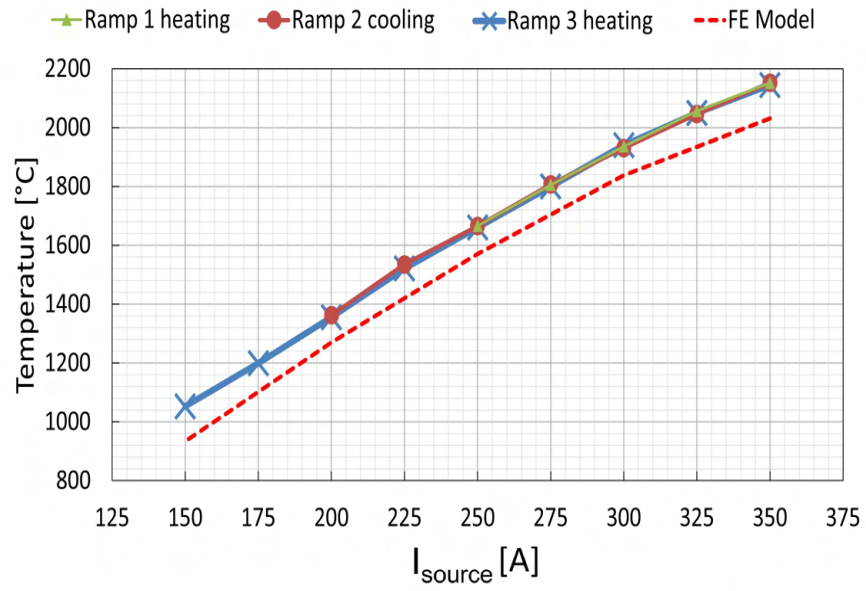

Figure 5.4: Experimental temperatures close to the mid-point of the hot-cavity and comparison to the Finite Element (FE) Model results, at different applied heating currents.

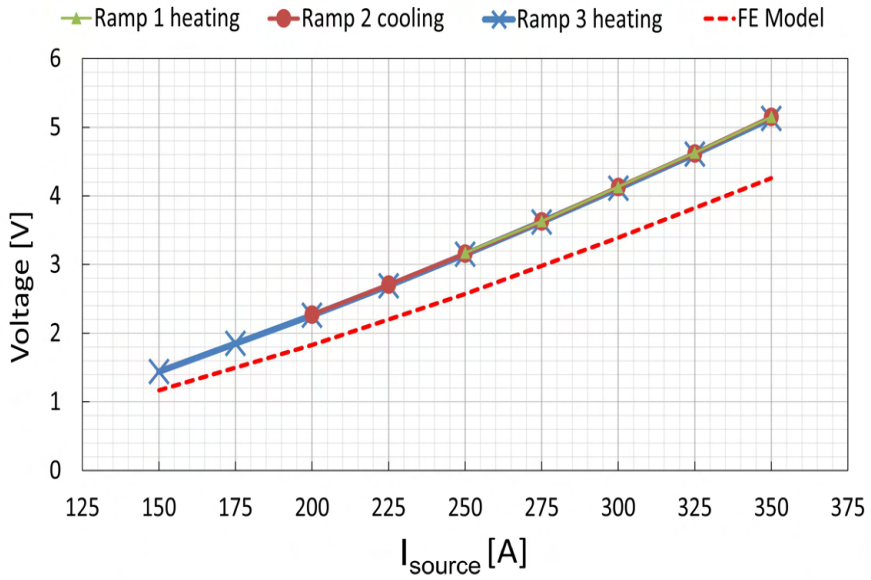

Figure 5.5: The electric potential difference values detected at the power supply and comparison to the Finite Element (FE) Model results, at different applied heating current.

For the same cycles of thermal calibration performed, the Electric potential difference values detected at the power supply were also noted, shown in Figure

5.5. In the conventional use of the ion sources, the polarity is applied in such a way that the beginning of the transfer line is maintained at a higher voltage potential and it gradually drops towards the exit of the hot cavity. This provides an axial field that favors the drifting of the ions, inside the ion source, towards the exit for extraction [55, 68, 69, 70].

Both in Figure 5.4 and 5.5, the measured values are higher than the values obtained from the Finite Element (FE) Model, developed and presented in [61]. This is explained by the fact that in the FE model, the simulations were performed considering an ideal contact between the surfaces. The temperature distribution and the potential gradient along the whole length of the transfer line and the hot cavity for the SPES ion source at different heating currents have been studied before and can be found in [61].

5.3.2 Time Structure of Gallium Ions

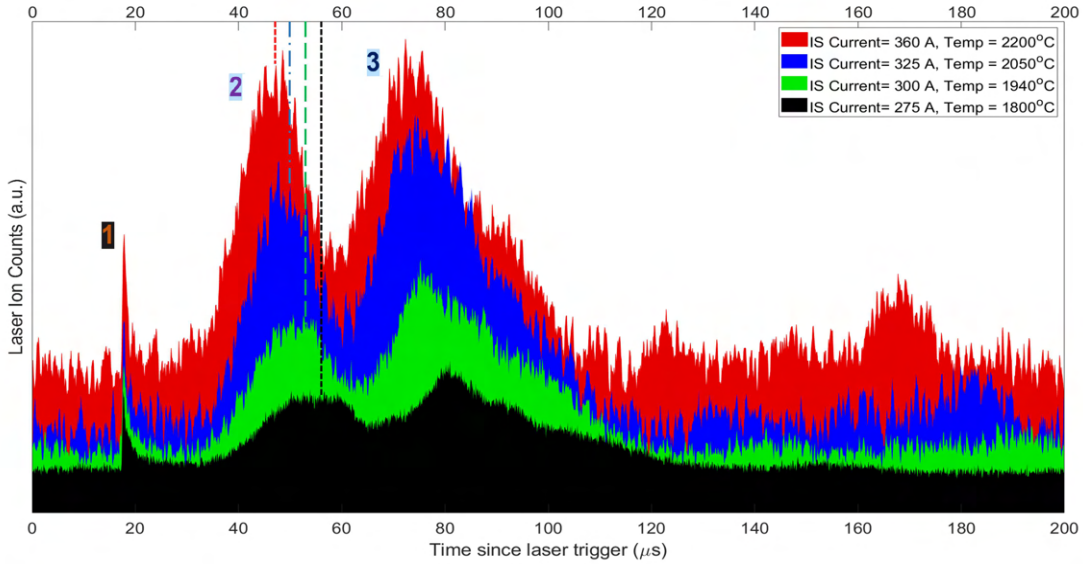

Figure 5.6: Time structures of ^{71}Ga ions at different ion source (IS) heating currents (temperatures). Temperatures 2200°C, 2050°C, 1940°C and 1800°C indicated in red, blue, green, and black respectively. Dotted lines indicate the centroids of the second peaks at different temperatures.

For ion beam time structure measurements, the separation magnet was tuned to the gallium isotope of mass 71 u. As described in Section 5.2.1, the ion beam of $^{71}Ga^{+}$ was directed onto a MagneTOF^{TM} detector. The average ion current was kept below 500 fA (corresponding to around 300,000 ions per second) as the detector was used in single ion counting mode. The power of the green laser

beam was reduced to around 10-20 mW, just enough to produce laser ions whilst staying below the safety limit of the operation mode of the detector.

The time structure measurements were performed for different ion source temperatures at 2200°C, 2050°C, 1940°C, and 1800°C, as shown in Figure 5.6. In all the time profiles, t=0 is given by the trigger of the laser pulse. Three main peaks are observed: first around 18 µs, second between 45-55 µs, and third between 70-85 µs.

The first peak is the pre-bunch of ions that are formed in the outermost part of the ion source, and extracted almost immediately by the penetrating extraction field. This region is indicated as "1" in Figure 5.7 and typically extends inwards by exactly the same value as the opening diameter of the ion source. This "fast extraction" peak was also observed and discussed in several RILIS studies [68, 70].

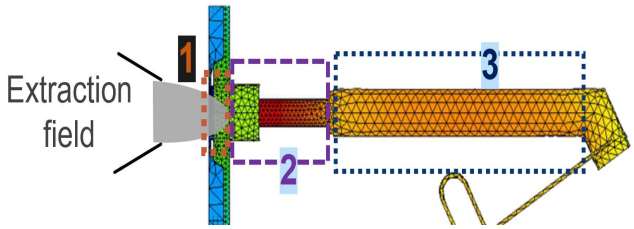

Figure 5.7: Different sections of the ion source assembly in relation to the ion bunches produced. Region 1 indicates the outermost part of the ion source which is penetrated by the extraction field. Regions 2 and 3 indicate the hot cavity and the transfer line, respectively.

The second bunch originates from the hot cavity of the ion source, indicated as region 2 in Figure 5.7. The third bunch is from the transfer line (region 3) connecting the hot cavity to the atom source (sample holder capillary in this particular case). It is clear that a large proportion of the extracted ions originates from the transfer line. This means the confining thermal plasma is present not only in the hot cavity but also in the transfer line.

Axial electric field and movement of the ions

Looking at the profiles at different temperatures, it can be clearly observed that apart from the first pre-bunch, all the other bunches are shifted in time. Considering just the second peak for simplicity, the centroids of the peaks at different temperatures are indicated with the dotted lines of the corresponding color in Figure 5.6. It is evident that the ions travel faster to the extraction zone (exit of the ion source) at higher temperatures. This effect can be explained simply by

the higher voltage gradient at higher temperatures, promoting a faster movement of the ions along the length of the ion source and transfer line volumes.

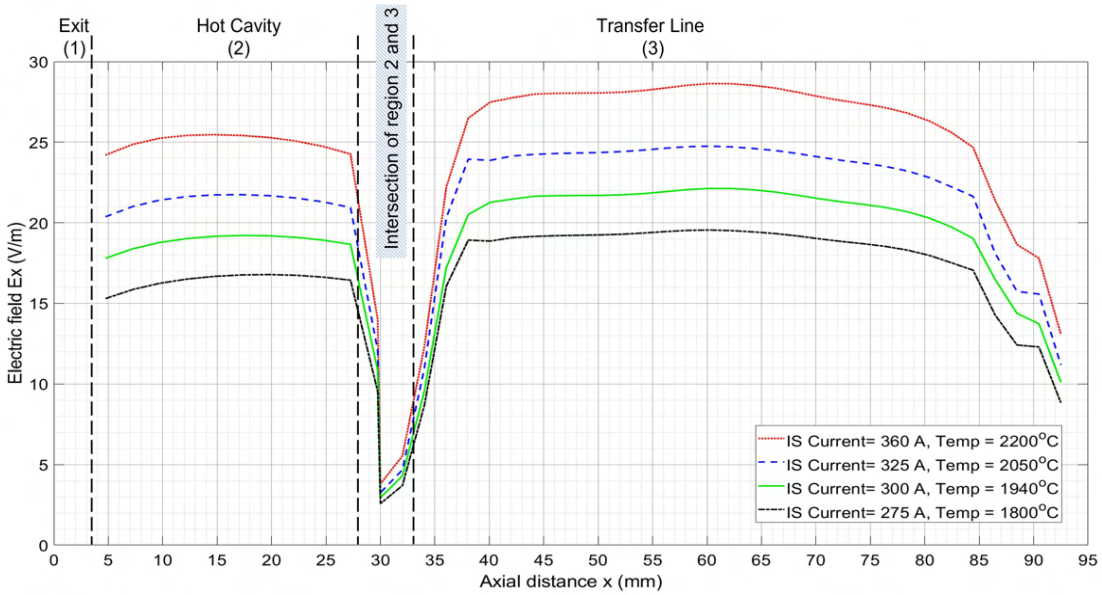

Figure 5.8: FEM simulation of the axial electric field along the length of the ion source (IS) at different heating currents (temperatures). Temperatures 2200°C, 2050°C, 1940°C and 1800°C indicated in red, blue, green, and black respectively.

If the axial electric field is responsible for the movement of the ions inside the ion source, we should be able to track the origin of the second bunch in the time structure back to the hot cavity, taking into account the acceleration acting on the ions by the axial field. A FEM simulation of the axial electric field for different heating currents (temperature) is shown in Figure 5.8. The axial electric field E_x has an increasing trend at the very beginning of the transfer line. It soon maintains a relatively constant value for the major part of the transfer line length, until it exhibits a sudden drop where the transfer line is connected to the hot cavity, due to a sudden increase in the cross-section which decreases the electrical resistance by a large factor. In the hot cavity, the axial field regains an almost constant value.

The electric field shows a slightly higher value in the transfer line compared to the hot cavity. This is due to the fact that the transfer line is thinner and has an effective cross-section of 10.6 mm^2 while the value in the hot cavity is 12.9 mm^2.

As it is known that the pre-bunch originates from the outermost part (close to the exit) of the ion source, this point can be used as a reference point for our

Table 5.1: Computation of the parameters related to the second bunch of ions in the time structure for different temperatures.

Temp. (°C)	T_1(μs)	T_2(μs)	T_{21}(μs)	Av. E_x (V/m)	L_{21_calc} (mm)	L_{10} (mm)	L_{20} (mm)
2200		46.08 ±0.15	28.24 ±0.20	24.99	13.53 ±0.19		16.63 ±0.19
2050	17.84 ±0.05	47.72 ±0.16	29.88 ±0.21	21.34	12.93 ±0.18	3.10	16.03 ±0.18
1940		49.23 ±0.20	31.39 ±0.25	18.82	12.59 ±0.20		15.69 ±0.20
1800		54.34 ±0.53	36.50 ±0.58	16.40	14.83 ±0.47		17.93 ±0.47

calculations. The idea is to calculate the distance the ions would travel under the influence of the axial electric field during the time interval between the first pre-bunch and the peak of the second bunch.

The acceleration a experienced by the ions with charge q and mass m in the axial electric field E_x is given by

$$a = \frac{qE_x}{m} \tag{5.4}$$

Two main approximations are used for the calculations:

1. Initial ion velocities (thermal) are considered to be zero, as they have an isotropic distribution in all directions.

2. As the value of the axial field E_x has a very low variance in the hot cavity at a given temperature, a mean value of E_x is assigned for the hot cavity.

If T_1 is the temporal position of the pre-bunch and T_2 is the position of the second bunch in the time structure, T_{21} indicates the time gap between them. Assuming zero initial velocity, the distance that the ions would have traveled during this time is given by,

$$L_{21} = \frac{1}{2} a T_{21}^2 \tag{5.5}$$

The deepest point inside the ion source that the extraction field of 30 kV can penetrate is 3.1 mm from the exit of the ion source. It corresponds to the pre-bunch at time T_1 and a value of $L_{10} = 3.1$ mm can be assigned to this point.

To find the origin of the second bunch of ions relative to the exit of the ion source, the value L_{20} can be simply evaluated as,

$$L_{20} = L_{21} + L_{10} \tag{5.6}$$

Table 5.1 shows the computed values of L_{20} (on the rightmost column) for different ion source temperatures. All the values of L_{20} are in agreement with the fact of the peak of the second bunch of ions originating from the mid-section of the hot cavity, whose total length is 33 mm. These values have been calculated by using the acceleration of the ions provided by just the axial electrical field, see Equation 5.4. This shows that the axial field across the ion source plays a very critical role for the forces experienced by the ions drifting along the central axis of the source.

For the ion source at temperature 2050°C (blue), a few smaller peaks start to appear after 100 µs (after the third main bunch). At 2200°C (red), two small peaks appear around 122 µs and 147 µs, along with a much more prominent peak

appearing at around 167 µs. These could be indications of slower ions formed deeper and at the very beginning of the transfer line. As seen from Figure 5.8, the axial electric field at the beginning of the transfer line is lower compared to the rest of the transfer line. This lower axial field should essentially cause relatively slower movement of the ions originating here. As the design of this ion source has an angular bend at the beginning of the transfer line, it could possibly hint that the ions formed in this zone, undergo velocity change continuously to find the main axis of the ion source. Further detailed ion trajectory simulation investigations are foreseen in future work to complement this semi-quantitative approach presented here, also with a special scope on ion confinement characteristics.

5.3.3 Laser Enhancement Ratio

Enhancement of the ion yield due to the laser effect was measured. For that, a Faraday Cup is inserted in front of the MagneTOF^{TM} detector. The separation magnet was tuned to the gallium mass of 69 u for slightly better statistics as the natural abundance of ^{69}Ga is higher compared to ^{71}Ga. The lasers were set at a 10 kHz repetition rate, the working condition in the online production of isotopes. As the atoms or the species have an effusion time in the order of 100 µs, a repetition rate of 10 kHz provides a condition in which we expect that all atoms will encounter at least one laser pulse during their effusion through the hot cavity.

Dependence on the power of the non-resonant step

The cross-section of a non-resonant transition step is, generally, two to four orders of magnitude lower than that of a resonant transition. With the typically available pulse energy (1-4 mJ) used for such transitions, saturation is not expected to be reached and the ionization efficiency is directly proportional to the laser power available for the non-resonant ionization step.

At the ion source temperature of 2200°C, the laser enhancement ratio was measured for various power of the green laser used for the non-resonant ionization, keeping the power of the UV fixed around 100 mW. The obtained values are plotted against the laser power, as shown in Figure 5.9. The measurement indicates that the non-resonant step is saturated at only 1 mJ (10 W). This is inconsistent with the typically observed behavior at the ISOLDE RILIS where this ionization scheme is regularly used. In this case, we suspect that a power-dependent thermal lensing effect is occurring. Beyond 10 W, local heating of the vacuum entrance window is causing a defocusing of the green beam at the

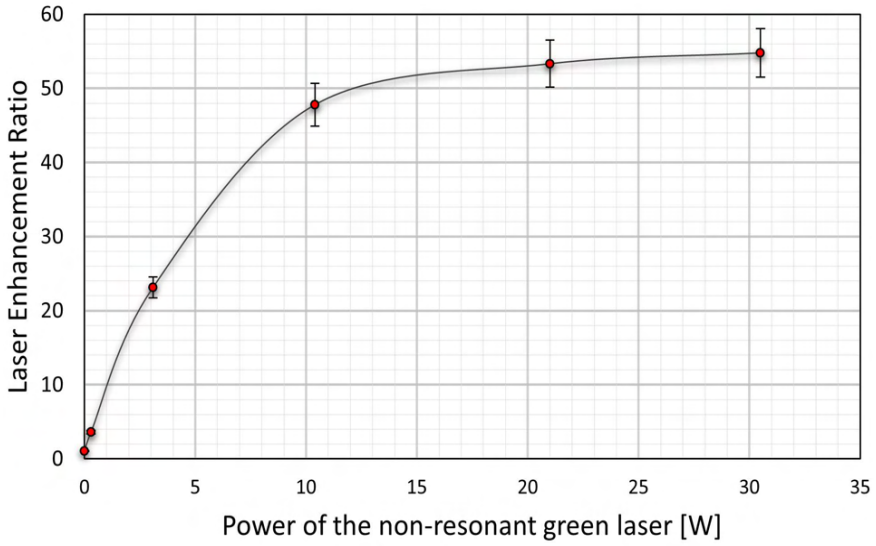

Figure 5.9: Laser enhancement ratio at different power of the non-resonant green laser (532 nm) and fixed UV power of 100 mW, at an ion source temperature of 2200°C.

position of the ion source, resulting in a reduced power delivery efficiency.

Nevertheless, from this measurement, it could be safely inferred that we could operate the green laser with around 20 W of power without losing efficiency in the current setup.

Dependence on the ion source temperature and the total ion current

To understand the selectivity of the laser ion source at different ion source temperatures and different total ion currents (ion load), laser enhancement ratios (LERs) were measured for various combinations of the mentioned parameters, shown in Figure 5.10. As indicated in Section 5.2.2, surface ionized barium was used to regulate the ion load in the ion source. The total extracted ion beam before mass separation serves as a measure for this quantity. During this measurement, the power of the UV and the green laser were maintained at 100 mW and 20 W, respectively.

As can be seen from Figure 5.10, the LER values remain nearly constant for the ion source temperature at 2200°C. The values vary in the small range of 52.0-57.5 up to an ion load of 1.1 µA. At 1800°C and 2050°C, the LER values show a declining trend as the total ion current increases, hinting at an effective decline of the laser ion confinement at these temperatures. At 1800°C, the LER value starts off with a high value of 480 at a total ion current of 80 pA and declines

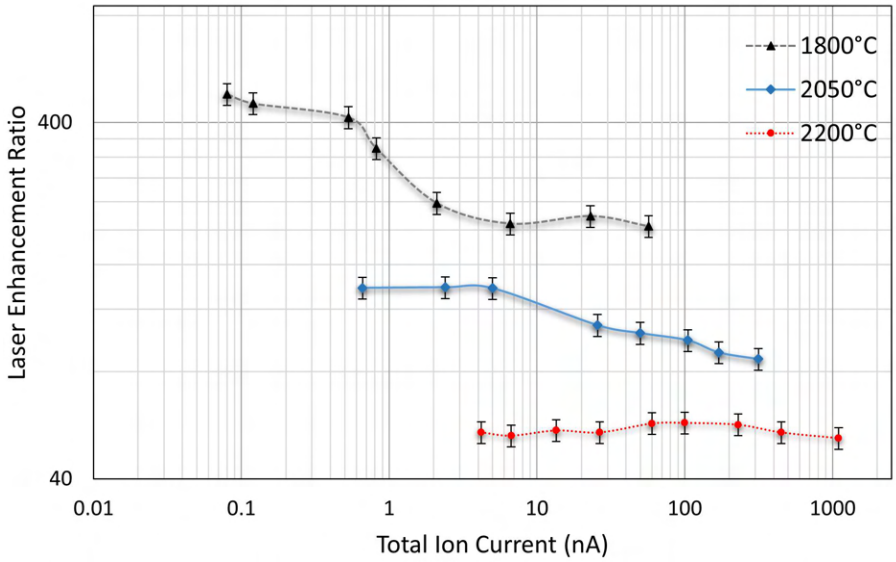

Figure 5.10: Laser enhancement ratio (LER) at different ion source temperatures and total ion current. The ion source temperatures 1800°C, 2050°C, and 2200°C are indicated in black, blue, and red curves, respectively.

quickly until a value of 204 at an ion current of 57 nA. Also in the case of 2050°C, the LER values decline from a starting value of 137 to a value of 87 while varying the total ion current from 660 pA to 315 nA.

The relative surface ionization efficiency values at different temperatures for ionization of gallium ($W_i = 6$ eV) with tantalum ($\phi = 4.28$ eV) ion source could be calculated using Equations 3.25 and 3.26.

$$\beta_{2200} : \beta_{2050} : \beta_{1800} \simeq 1 : 0.6 : 0.2 \simeq 5 : 3 : 1 \tag{5.7}$$

The ratio provided above is for single atom-wall collision and serves to explain qualitatively the dropping LERs with increasing ion source temperatures. In practice, the amplification factor N at different temperatures needs to be considered as well since the effective ion survival factor also increases with the rise in ion source temperature.

At the ion source temperatures of 1800°C and 2050°C, a declining trend in the value of LER is observed as the ion load is increased. This can be attributed to the temperature dependence of the thermionic electron density in the hot cavity (Equation 5.3). It follows therefore that, at higher temperatures, the cavity ion capacity (the ion density at which the confining potential for ions is compromised), is greater.

At 2200°C, the nominal working temperature of the SPES ion source, and the maximum proton beam intensity (200 µA) on the UC_x target, the total surface

ion current is expected to be around 200 nA. From Figure 5.10, it can be clearly confirmed that the selectivity of the laser ion source is not affected up to a total ion current of 1.1 µA, a value much higher than the expected maximum total ion current.

5.3.4 Ionization Efficiency Measurements

In this section, we report one measurement of surface ionization efficiency and three measurements of laser ionization efficiency, performed at an ion source temperature of 2200°C and ion load conditions up to 110 nA of the total beam, see Table 5.2.

Surface ionization efficiency

The surface ionization efficiency measurement was conducted with a sample size of 76 nAh and resulted in a value of 0.49% efficiency.

The theoretical surface ionization efficiency value for single atom-wall interaction can be calculated using Equation 3.25 and 3.26. At T = 2200°C, the value of β of gallium ($Q_i/Q_o = 0.22$, $W_i = 6$ eV) with tantalum ($\phi = 4.28$ eV) as ionizer material is calculated to be 0.007%. From the measurement, we find that the surface ionization efficiency value is $\beta_c = 0.49\%$, indicating an amplification factor of $N = 70.3$ (see Equation 5.2).

This measurement was done, also, to serve as a reference point to possibly co-relate the laser enhancement ratios and the laser ionization efficiency values.

Laser ionization efficiency

For the laser efficiency measurements, the laser powers used were: 100 mW (UV) and 20 W (green). The first two measurements were performed with sample sizes of 76 nAh and maintaining the isotope current of ^{69}Ga around 4-5 nA. The third one was performed with a sample size of 114 nAh and an isotope current of around 7-8 nA. From the tests, it can be deduced that, under ideal conditions in terms of ion load, the SPES laser ion source can provide a laser efficiency of around 27.2% using the indicated gallium scheme, laser powers, and 2200°C ion source temperature.

A number of laser enhancement ratios (LERs) were also measured during all these efficiency tests by turning the laser on/off for just a few seconds (see Table A.1). The mean value of the LERs is around 55.5. It is quite evident that if the surface ionization efficiency value of 0.49% is multiplied by the obtained mean

Table 5.2: Measured ionization efficiency values of gallium at ion source temperature 2200°C

Test no.	Type	Efficiency(%)	Mean Efficiency(%)
1	Surface	0.49 ±0.04	0.49 ±0.04
2	Laser	27.66 ±2.07	27.18 ±1.18
3	Laser	27.64 ±2.07	
4	Laser	26.23 ±1.97	

LER value of 55.5, we get a value of 27.2% which is very close to our obtained laser ionization efficiency value of 27.18%.

It must be noted that, at 2200°C, the zero level state $3d^{10}4s^24p\ {}^2P^\circ_{1/2}$ is only 45% populated assuming the Boltzmann distribution and the rest i.e. 55% population is in the state $3d^{10}4s^24p\ {}^2P^\circ_{3/2}$ (826.19 cm^{-1}). In the gallium-scheme used in this experiment, a first step transition at 287.42 nm, between the zero level state ${}^2P^\circ_{1/2}$ and first excited state $4s^24d\ {}^2D_{3/2}$, is used. If an additional laser at 294.36 nm is available, it is possible to make transitions to the neighboring excited state ${}^2D_{5/2}$ (34787.85 cm^{-1}) from the state ${}^2P^\circ_{3/2}$. As the second step is a non-resonant step, the green laser will promote the electrons into the continuum regardless of whether it finds the electrons in ${}^2D_{3/2}$ or ${}^2D_{5/2}$ state after the first resonant excitation. In this case, the laser ionization efficiency could be almost doubled, according to [71].

5.4 Discussion

The SPES laser ion source cavity has been characterized in terms of ion beam time structure, ion throughput for different operating temperatures, and ionization efficiency at 2200°C for the ionization of gallium atoms. The surface ionization efficiency and time structure measurements indicate that the transfer line plays an important role in the overall laser and surface ion production. At the nominal operating temperature of 2200°C, the cavity ion throughput (the ion rate at which no loss of laser ion performance is observed) exceeds 1 µA, an order of magnitude greater than has been measured for the standard ISOLDE RILIS cavity which has a passively heated transfer line without an axial extraction voltage gradient.

It is also observed that the ions are confined not only in the hot cavity but also in the transfer line, with a large fraction of the extracted ions originating inside the transfer line. It means that the confining plasma must also be present

in the transfer line.

The axial electrical field has been demonstrated to provide the drifting acceleration of the ions along the length of the ion source. This aspect is important for the transport of the positive ions in the direction of the ion source extraction.

The laser enhancement ratios (LERs) are found to be almost independent of the total ion load at an ion source temperature of 2200°C. This reflects a very stable laser ion confinement due to excess thermionic electrons created at this temperature and hints at maintaining also constant laser ion source efficiency in this regime. At ion source temperatures of 2050°C and 1800°C, the general behavior of LERs dropping with the increase in the ion load is observed.

A laser ionization efficiency of 27.2% is reported for gallium using a resonant 287.42 nm (100 mW) and a non-resonant 532 nm (20 W). Use of an additional laser beam at 294.36 nm would allow us to potentially further increase the ionization efficiency by 20-30%, by accessing electrons in the thermally populated state $3d^{10}4s^24p\ {}^2P^\circ_{3/2}$.

The SPES ion source has undergone several heating and cooling cycles during the calibration phase and during the measurement sessions, including power supply failures. The ion source continues to demonstrate very stable behavior, exhibiting very high thermal robustness. The ion source is also now validated for use at SPES for high-power targets where the steady-state ion rate is expected to be 200 nA.

The work has been submitted for publication to Nuclear Instr. and Methods in Physics Research Sec. B in July 2023 and is currently under review.

Chapter 6

New TOF-MS Assembly in the Online Laser Lab

6.1 New TOF-MS Assembly

In the SPES online laser lab, described in [1], three Ti:Sa laser systems are already installed and functional. A new time of flight mass spectrometer (TOF-MS) has been designed and assembled in the online laser lab. The purpose of this TOF-MS is to facilitate additional scheme development of different elements while the lasers are not in use for online RIB production and, also to be able to perform laser spectroscopy with a resolution higher than the one which can be achieved in the offline laser lab.

A detailed sketch of the online laser lab is shown in Figure 6.1. Three optic tables are placed inside the laser lab. Two Ti:Sa lasers coupled with harmonic generation units are placed on optic table 1. Optic table 2 supports a Ti:Sa cavity without a harmonic generation unit. All these Ti:Sa cavities are independently pumped with *Ascend* pump lasers from *Spectra Physics*, as described in Section 2.2.2. The Ti:Sa systems can provide laser beams of finer linewidth up to 1 GHz (see Table 2.1) compared to the dye laser systems in the offline laser lab which has linewidth in the range of 2-4 GHz. The new TOF-MS is placed in front of the optic table 3 which is kept free for other related experiments or activities.

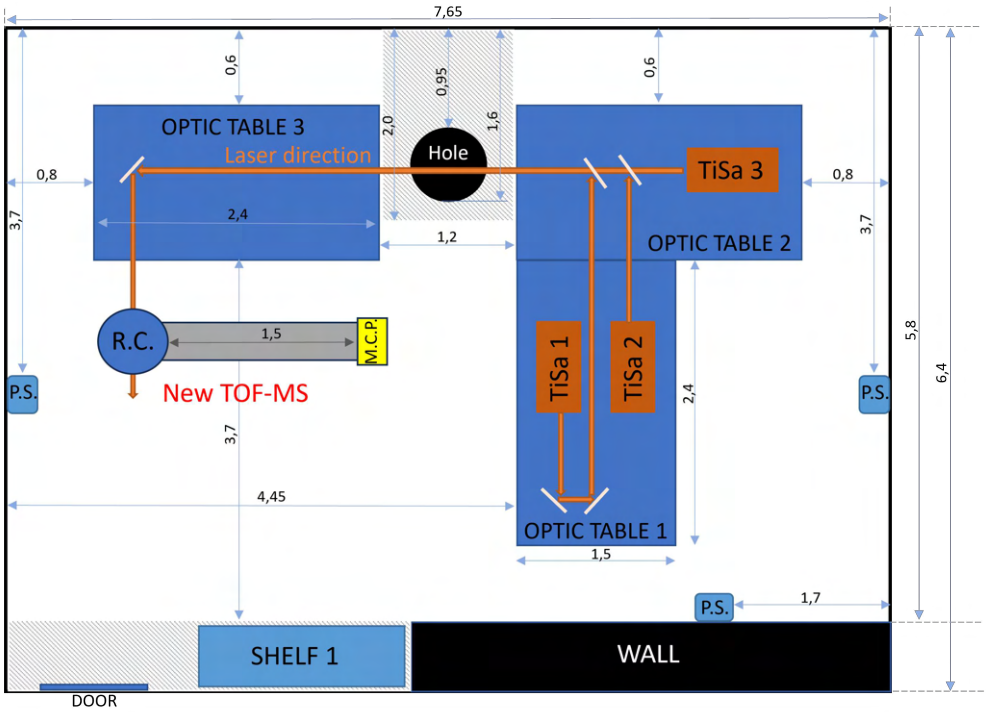

Figure 6.1: A sketch of the position of new TOF-MS in the online laser lab. All the dimensions are in meters. R.C. stands for reaction chamber, M.C.P. for the multi-channel plate detector and P.S. stands for power supply. The position of the three TiSa lasers and their intended optical beam paths are indicated. The grey region between optic tables 2 and 3 is dedicated to sending down laser beams through the hole for the online production of ion beams.

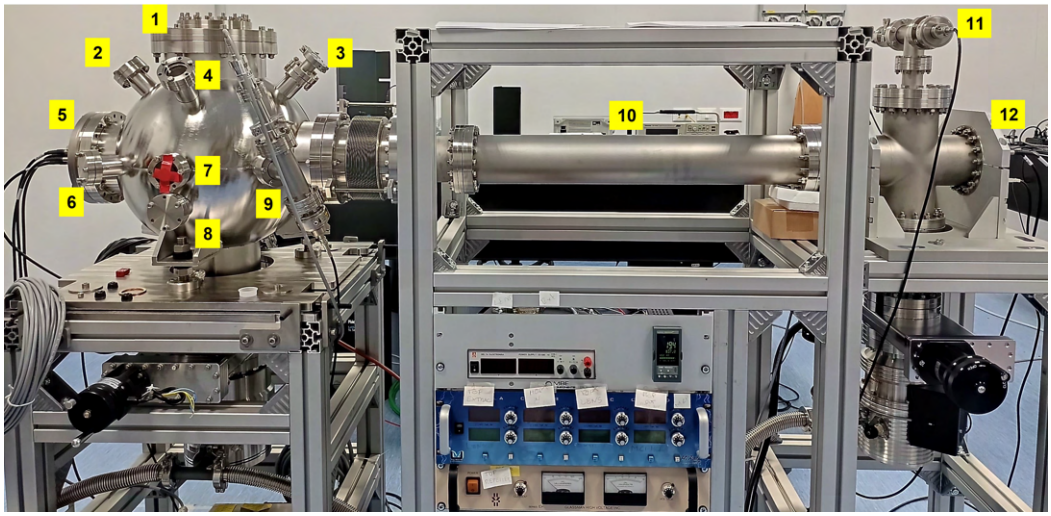

Figure 6.2: The assembled new TOF in the online laser lab at SPES facility.

The completely assembled new TOF-MS is shown in Figure 6.2. The reaction chamber is made of stainless steel and is spherical in shape with a diameter of 400 cm. It has several holes and cylindrical extensions placed in precise angles for specific purposes. These parts are labeled and explained in Table 6.1. Inside the chamber, an electrostatic ion optic system is placed for the extraction of ions created in the chamber. The reaction chamber is connected to a tube of length 1.5 meters for the flight of the extracted ions. A MCP detector is connected to the end of this tube to detect the ions.

Table 6.1: Description of the labeled parts in the TOF-MS. X' indicates a part placed on the exact opposite side of the sphere w.r.t. the position of X.

Label	Description
1	Entrance window of the ablation laser
2	View port/ Entrance window for orthogonal injection of laser beam relative to the atomic vapor from the effusion cell
3	Same as "2"
4	View port
4'	Effusion cell
5	Flange for the dis-mountable ion optic system
6	Control of the "laser screen"
7	Exit of the excitation laser(s)
7'	Principal entrance of the excitation laser(s)
8	Ablation target system
9	Two vacuum gauges of different ranges ($> 10^{-3}$ mbar and $< 10^{-3}$ mbar)
10	Ion flight tube
11	Same as "9"
12	MCP detector

6.2 CAD model of the new TOF-MS

The sectioned views of the CAD model of the TOF-MS are shown in Figure 6.3 and 6.4. The first represents the view with a vertical section plane passing through the axis of the system, while the second represents the view with a horizontal section plane.

In both the sectioned views, a series of four parallel plates/grids are seen attached to two white Macor® ceramics tubes along the axis of the system. These

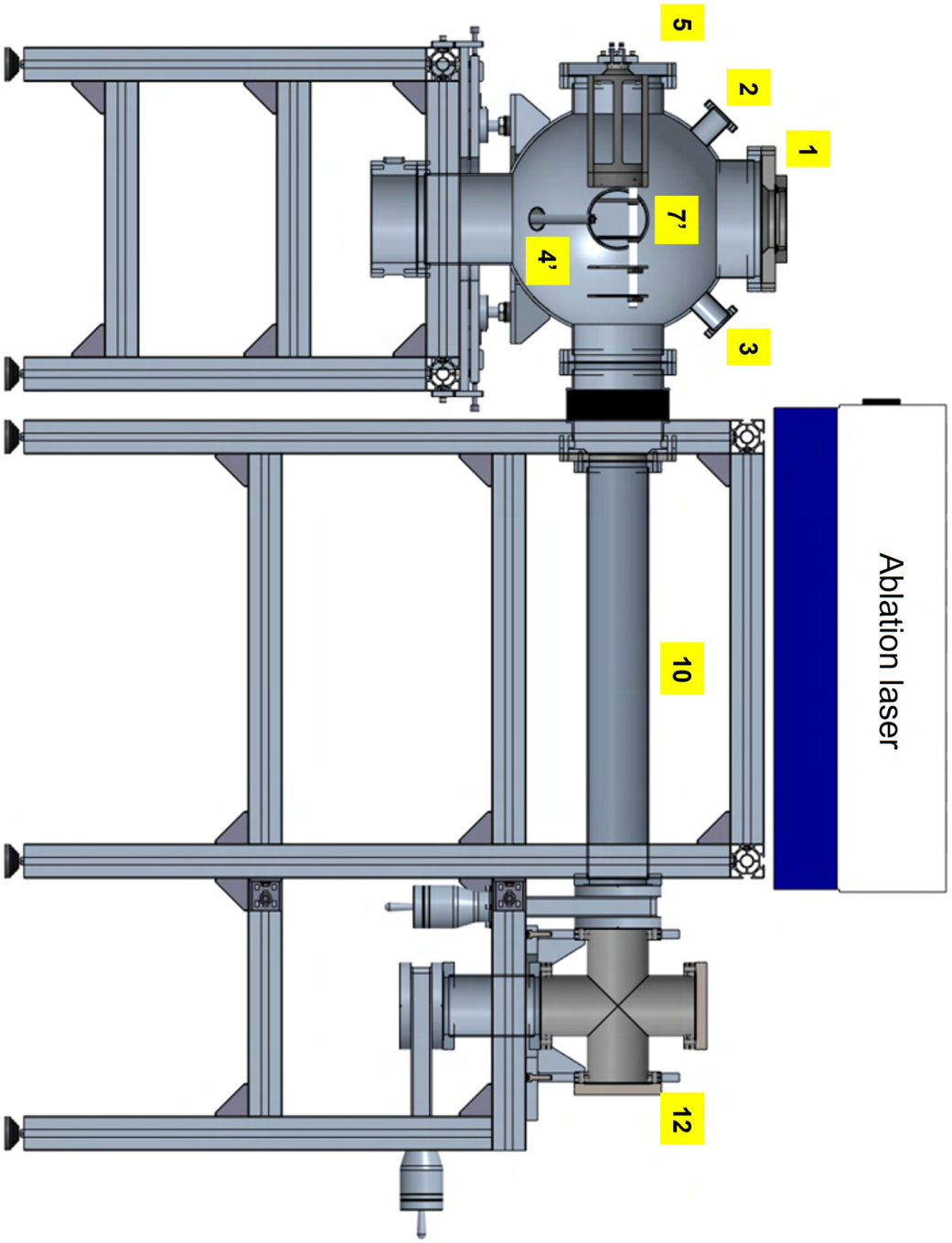

Figure 6.3: Side sectioned view: CAD model of the new TOF-MS in the online laser lab.

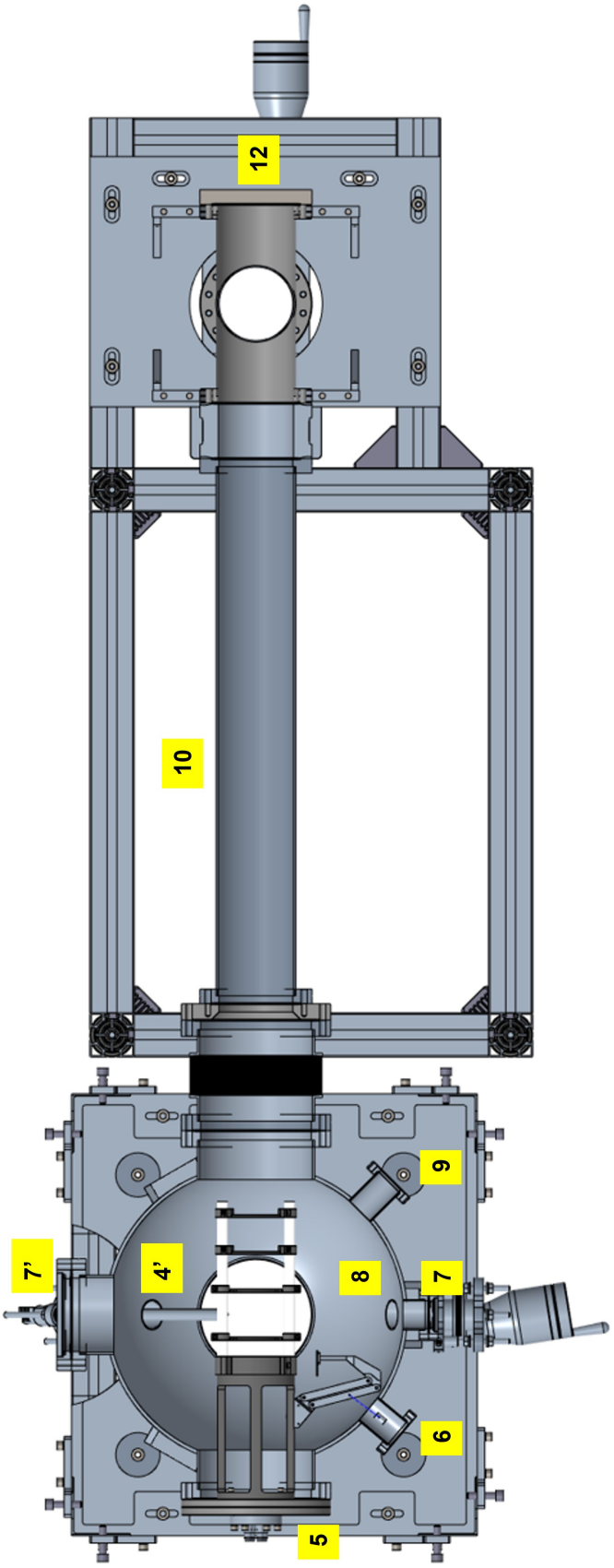

Figure 6.4: Top sectioned view: CAD model of the new TOF-MS in the online laser lab.

components: repeller, extractor, lens and zero grid (connected to zero potential), are the main parts of the ToF electrostatic ion optic system. This system extracts ions formed by the laser(s) in the center of the ToF reaction chamber. The center of the spherical chamber is, by design, aligned in the mid-point between the repeller and the extractor. It is discussed in detail in Section 6.4.

6.3 Atomic Beam Unit

Two sources of atomic beam/vapor are present in the system. The first is an ablation target system which will produce an atomic vapor in the vertical direction, orthogonal to the axis of ion extraction. The second source is an effusion cell which is aligned 45° with respect to the axis of ablation and also, orthogonal to the ion extraction axis.

6.3.1 Ablation target system

When a solid target is hit by a powerful, focused laser beam, a hot atomic plume can be produced. This plume is produced orthogonal to the surface of contact on the solid target.

In our reaction chamber, a homemade ablation target system will be placed through the port "8", as shown in Figure 6.5. Three different target materials can be loaded in the three vertical chimneys indicated by the red arrows. The solid target materials will be placed at the bottom of the chimneys which have an axial hole for passing the focused ablation laser coming through the entrance window "1" and eventually providing a path for the release of the atomic vapor in the vertically upward direction.

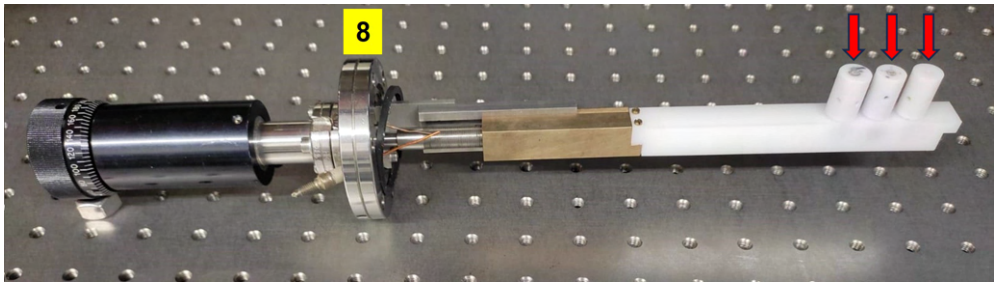

Figure 6.5: Ablation target system with three possibilities of loading three different elements. It is placed inside the chamber through port 8.

The size and shape of the target material and placement inside the target holder/chimney are shown in Figure 4.6 and 4.7. The nominal size of the target

is around 5 mm in diameter and 1 mm thick.

6.3.2 Effusion cell

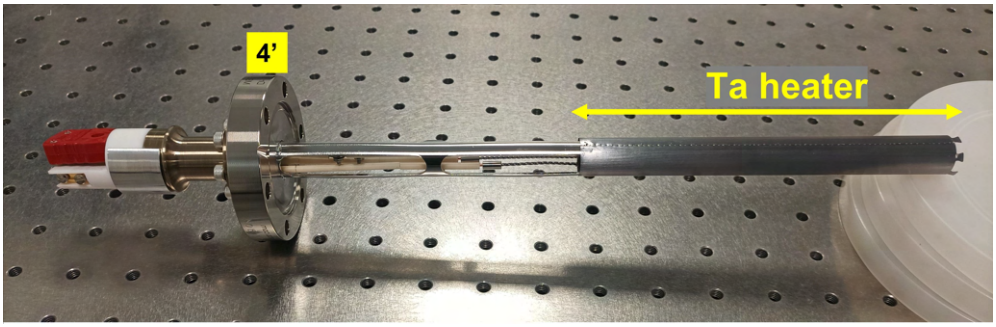

Figure 6.6: Effusion cell WEZ40-5-16-D16-standard, to be connected through port 4' of the reaction chamber. The right end has an opening through which the crucible is placed inside the Ta heater.

The effusion cell has been purchased from *MBE Componenten*. The cell is a standard WEZ40-5-16-D16 model, as shown in Figure 6.6. Main specifications about the effusion cell are listed below:

- Mounting flange DN40CF (Outer diameter 2.75")
- 5 cc crucible
- Ta-wire filament (standard)
- Type C WRe 5/26% thermocouple
- Maximum temperature 1400 °C (outgassing 1500°C)
- Electrical parameter: 150W/9A
- Dimensions under UHV: Outer diameter 16mm, length 280 mm

The effusion cell is inserted into the reaction chamber with the orifice of the crucible pointing towards the center of the sphere. A bellow (the yellow part), shown in Figure 6.7, is used to regulate the angular and longitudinal position of the effusion cell with respect to the center of the system. This regulation is essential as the density of the atomic jet coming out from the effusion cell decreases with the distance, and so the distance of the orifice needs to be experimentally optimized for a good TOF signal. At the same time, the orifice cannot be placed

very close to the center of the sphere because it could interfere with the electrostatic field between the electrodes of the ion optic system, especially between the repeller and the extractor.

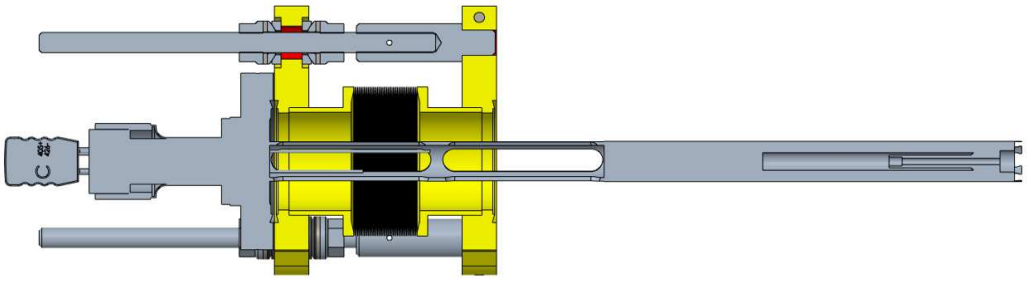

Figure 6.7: Sectioned CAD view of the effusion cell. The yellow component represents the bellow which is used for the regulation of the orientation and the position of the effusion cell inside the chamber.

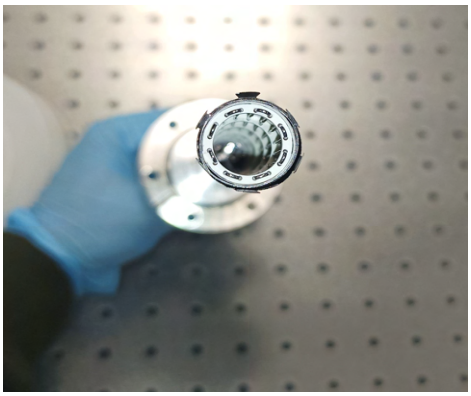

Figure 6.8: Inner view of the heater with Ta filaments

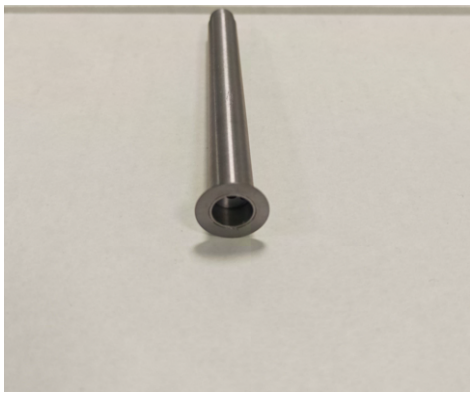

Figure 6.9: Ta crucible with collimated beam insert

Figure 6.8 provides a better view of the inside of the tantalum heater filaments. The tantalum crucible, shown in Figure 6.9, can be filled with the element or compound of interest, in the form of powder or small pieces. The crucible is then placed inside the tantalum heater, which once heated releases vapour of the element or the compound present in the crucible.

To perform an initial calibration of the heating of the effusion cell, the heating cycle was performed without the tantalum crucible placed inside the heater. Fig-

ure 6.10 shows the heated glowing tantalum filaments as seen from the viewport "4".

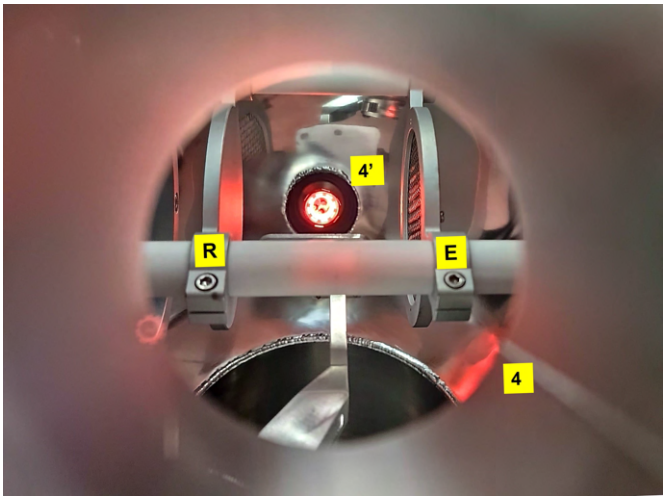

Figure 6.10: Heating of the effusion cell without the crucible. 4 is a view port, 4' is the port of the effusion cell, and R and E represent the repeller and the extractor grid of the ion optic system.

Table 6.2 presents the calibration data of the heating of the effusion cell performed with different DC voltage applied. A maximum voltage of 25 V can be applied to the cell and it should raise the temperature of the heater to 1350-1400°C. However, for the initial tests we operate it below 1000°C.

Table 6.2: Calibration of the effusion cell heating

Voltage (V)	Current (A)	Temperature (°C)
3.0	1.48	273.8
6.0	2.29	546.2
9.0	2.95	717.6
10.0	3.16	770.6
12.0	3.55	864.6
15.0	4.16	986.5

One of the biggest limitations to high-resolution spectroscopy is the Doppler broadening, which arises due to the velocity distribution of the atoms along the direction of the excitation laser. To avoid the Doppler contribution, a special insert is placed inside the crucible to provide a collimated beam from the effusion cell. The specifications of this collimated beam insert are:

- Length 105 mm
- Diameter 10 mm
- Tube 90 mm × hole 2.5 mm

6.4 Dis-mountable Ion Optics System

The ions formed at the center of the reaction chamber by the laser-atom interaction need to be extracted and directed towards the detector. An electrostatic ion optic system, shown in Figure 6.11 , is placed inside the reaction chamber for this purpose. By design, the mid-point between the repeller R and the extractor E is aligned to the center of the reaction chamber. The whole ion optic system is built on a common Macor® support and is attached to one flange, which will be connected to the port "5" of the reaction chamber.

The fact that the whole system can be dismounted provides the convenience of making fixes or changes to the position of the electrodes, by taking it out of the reaction chamber.

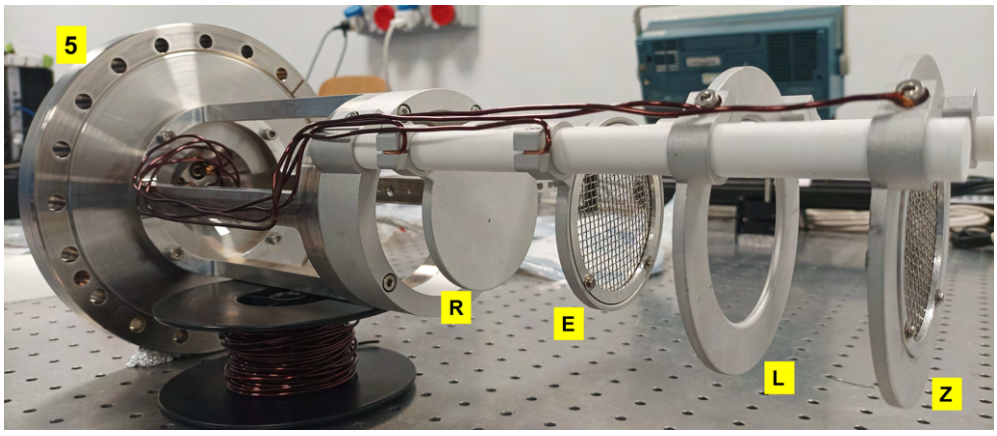

Figure 6.11: Fully dis-mountable ion optics system. R, E, L, and Z represents the repeller, the extractor grid, a circular electrostatic lens, and the zero grid, respectively. It is placed inside the reaction chamber through port 5.

The nominal voltages that will be applied to the individual electrodes, the dimensions, and the positions of the electrodes with respect to the center of the reaction chamber are provided in Table 6.3. The SIMION® simulation for the flight of samarium ions in the TOF-MS with the indicated parameters of the ion optics is shown in Figure 6.12.

Table 6.3: Ion optics parameter. Negative distance signifies in the opposite direction of ion extraction.

Electrode	Voltage (kV)	Diameter (mm)	Distance from the center of the chamber (mm)
R	5	70	-32.5
E	4	70	32.5
L	4	Inner: 70 Outer: 98	85
Z	0	70	132.5

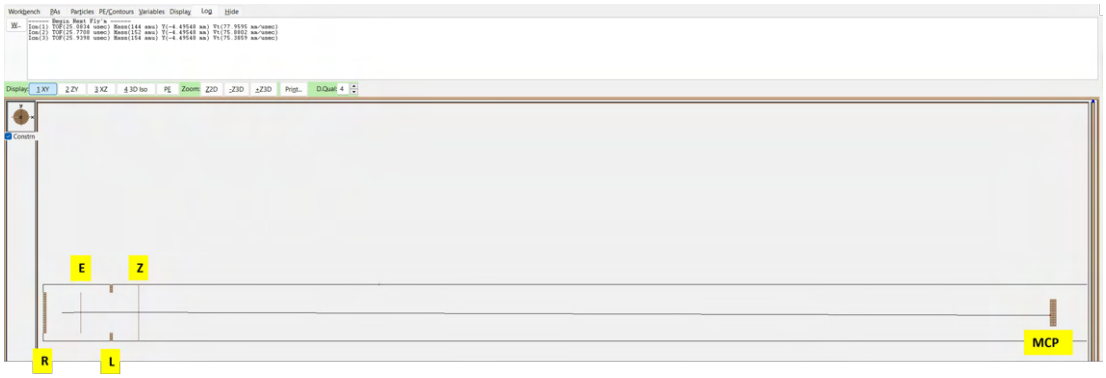

Figure 6.12: SIMION® simulation of the flight of samarium ions with the ion optics parameters indicated in Table 6.3.

6.5 Laser Screen

Most elements require more than one laser to achieve photo-ionization. The multiple laser beams need to overlap temporally and spatially with the atomic vapor. Overlapping the laser beams spatially in the center of the spherical reaction chamber is not a straight-forward process if the laser beams have the slightest angular separation between them.

A movable screen "S" is placed in the center of the reaction chamber to check the position of the excitation laser beams, see Figure 6.13. Having the screen in this position helps in centering the laser beams and to overlap on each other precisely. Once the laser beams are aligned in such way, the screen is moved away from the axis of the ion extraction system to avoid interference with the electric field, as shown in Figure 6.14. This mechanical adjustment can be easily controlled from outside the chamber by a translational movement of the cable

attached to the screen. It can be clearly seen from Figure 6.4 how this mechanical control is provided through the port "6".

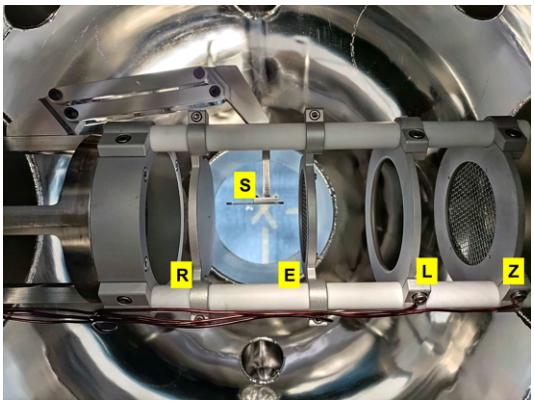

Figure 6.13: Electrode system with the laser screen "S" in; folded towards the axis of the electrodes

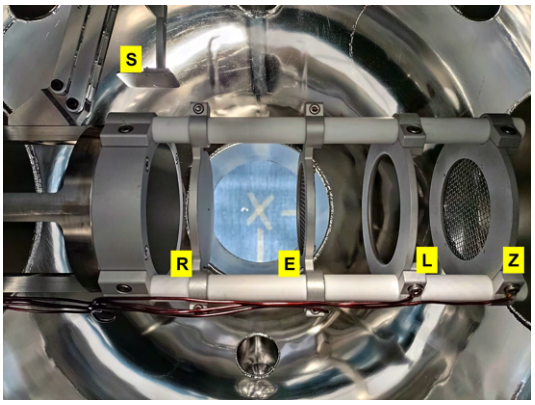

Figure 6.14: Electrode system with the laser screen "S" out; folded away from the axis of the electrodes

6.6 Detector

A microchannel plate (MCP) detector is used for the detection of the ions in our system. An MCP is a 2D component used to detect ions and amplify single particles or photons in vacuum. It is made up of countless millions of separate microchannels that communicate with one another in parallel through the MCP. The channels are structured in the MCP at a little oblique angle (referred to as a "bias angle") rather than running straight across. Every microchannel functions as a separate electron multiplier.

When charged particles (such as electrons or ions) or photons (light particles) enter the microchannels of the MCP, they collide with the walls of these channels. These collisions cause electrons to be emitted from the channel walls due to a phenomenon called secondary electron emission.

The emitted secondary electrons are accelerated by the high voltage applied across the MCP. As these secondary electrons travel down the microchannels, they collide with more channel walls, releasing additional electrons in the process. This creates a cascade or multiplication effect, leading to significant amplification of the original signal.

At the end of the MCP, the multiplied signal is collected and can be detected using various methods, such as an anode that measures the resulting electrical current. This highly amplified signal makes MCP detectors extremely sensitive

and capable of detecting even single ions.

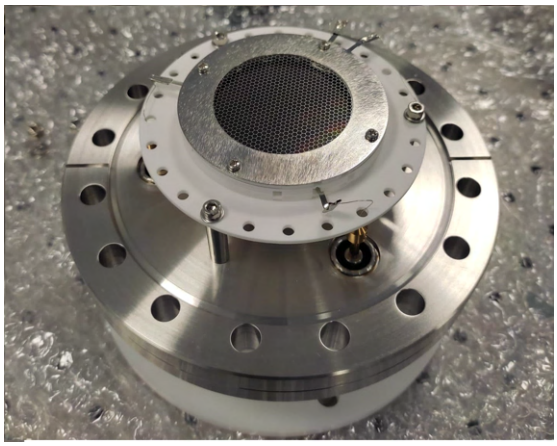

Figure 6.15: MCP-050-D-L-A-F-G-60 detector from Tectra GmbH

Figure 6.15 shows the MCP detector purchased from *Tectra GmbH*. Detailed information regarding the assembly we ordered and other types can be found on [72]. Some important specifications of our detector are provided in Table 6.4. The detector is already in place in the TOF-MS.

Table 6.4: Specification of the MCP detector

MCP Outer Diameter	50 mm
Anode Diameter	45 mm
Assembly	Chevron
Channel Length to Diameter Ratio	60:1
Max. Voltage (MCP Out - MCP In)	2.4 kV
Max. Voltage (Anode - MCP Out)	0.5 kV

6.7 Laser-Atom Interaction Region

The system is designed to have the interaction region of the laser beams and the atomic vapor at the center of the reaction chamber. Figure 6.17 shows the interaction of the excitation laser beams with the atomic vapor from the effusion cell, with a 45° angular separation.

If the ablation plume is used as the source of atom, a vertically rising atomic vapor will be obtained. This would provide an orthogonal (90°) intersection of the excitation laser beams and the atomic vapor. This, however, does not avoid the Doppler broadening because the ablation plume expands horizontally as it grows

away from the surface of the target, giving rise to a conical shape. It means that even if the excitation lasers are orthogonal to the main axis of plume growth, it interacts with the horizontal component of the atomic velocity regardless.

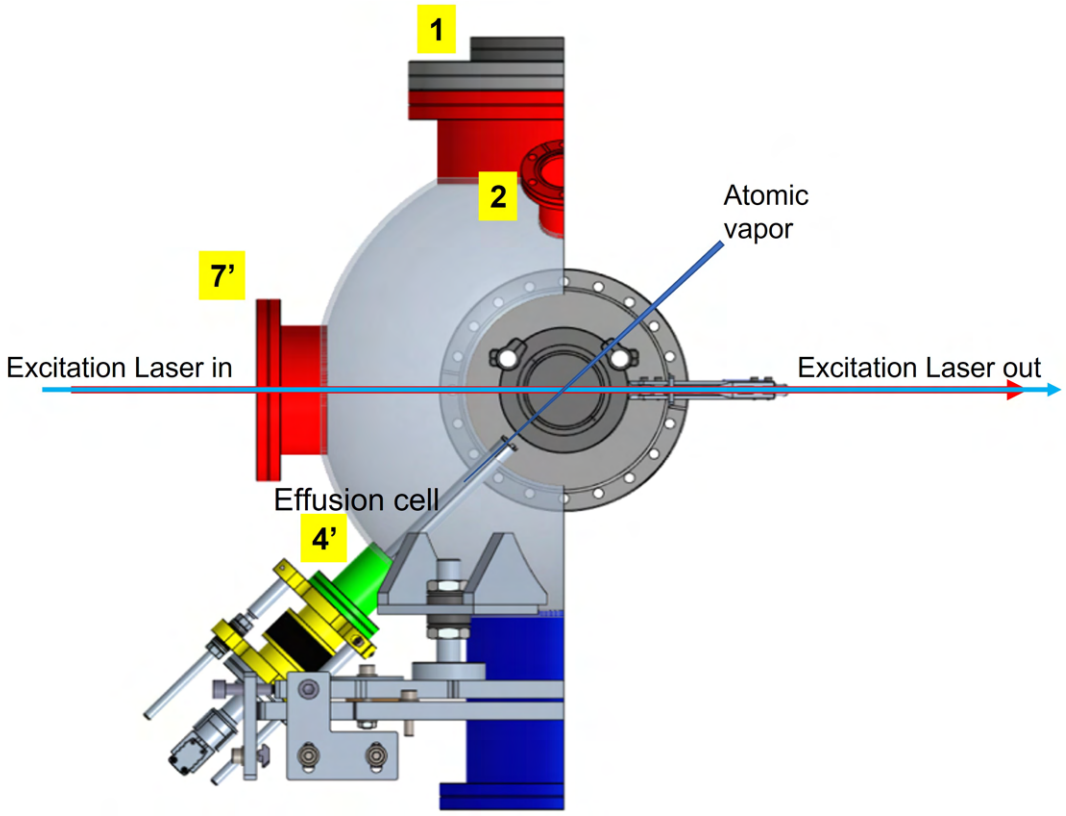

Figure 6.16: Section view of the reaction chamber showing the effusion plume (atomic vapor) and its interaction with the excitation lasers.

In this configuration of the laser-atom interaction, scheme development for the resonance photo-ionization of elements can be performed regardless. If high resolution spectroscopy is the goal, the Doppler broadening needs to be suppressed. This is discussed in the next sub-section.

6.7.1 Orthogonal injection of laser beam

One of the basic approaches to suppress Doppler broadening in a multi-step resonant spectroscopy is to avoid probing the same velocity component of the atoms with the different excitation lasers. This can easily be achieved if the excitation lasers are orthogonal to each other.

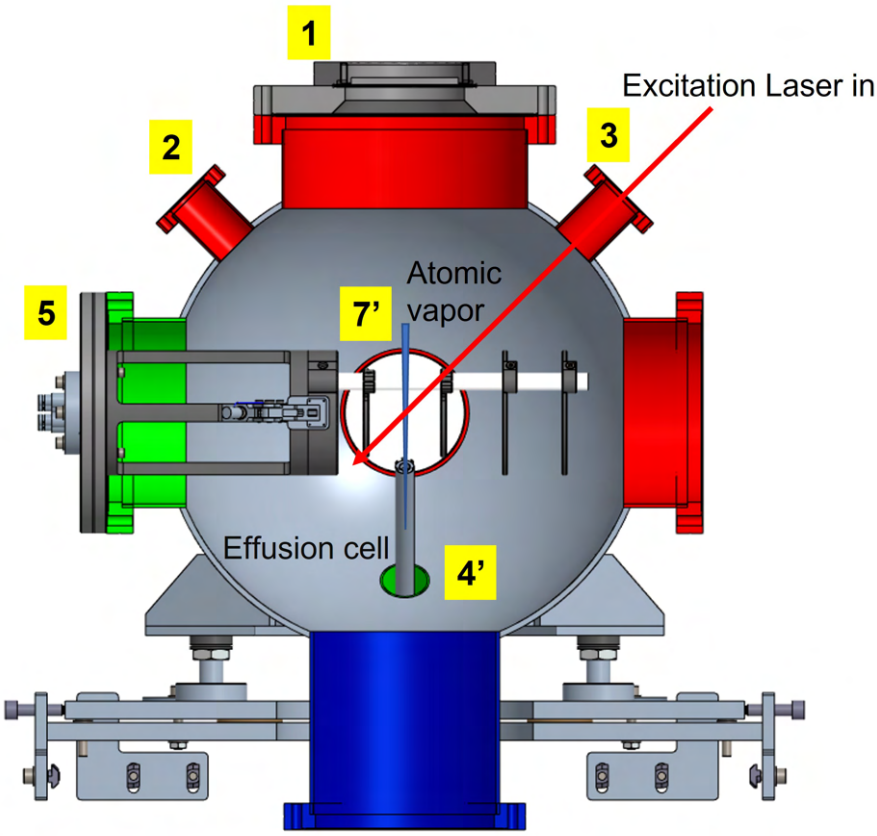

Figure 6.17: Section view of the reaction chamber showing the effusion plume (atomic vapor) and its interaction with the orthogonally injected excitation laser.

Imagine a two-step resonance photo-ionization process. Let us say a resonant laser beam is passing through the entrance window 7' as shown in Figure 6.17. Now, if the other excitation laser is sent into the atomic vapor through the entrance windows 2 or 3, they will be orthogonal to each other. If the laser beam is sent through window 3, it can arrive at the center of the reaction chamber from outside the extraction grid or by passing through the extraction grid itself. If there is any physical blockage to the path of the laser beam by the non-grid part of the extraction grid, the position of the grid can be changed by gliding it on the Macor® support and eventually adjusting the voltages supplied to the electrodes to maintain an efficient ion extraction. This could suppress the Doppler broadening regardless to the atom source: ablation target or effusion cell.

Having the effusion cell as the atom source has an extra advantage. As described in 6.3.2, the effusion cell has an insert that can provide a collimated

atomic beam. This should ensure a narrower resonance profile of the transitions.

6.8 Status of the System

The TOF-MS is completely assembled in the online laser lab. At the moment, a single turbo-molecular pump is used under the reaction chamber, and the whole system is maintained at a pressure of 2-3 $\times$ 10^{-7} mbar. A second turbo-molecular pump will be placed under the MCP chamber to allow separate pumping of the MCP. A valve is present between the tube and the MCP cross-chamber to provide this separation. This valve is placed to ensure that the MCP can stay in vacuum when target change is performed.

The electrical connections have been checked and verified for high-voltage operations. A clear and safe laser pathway has been created for the transport of the laser beams from the Ti:Sa lasers to enter the reaction chamber.

6.9 Future Perspective

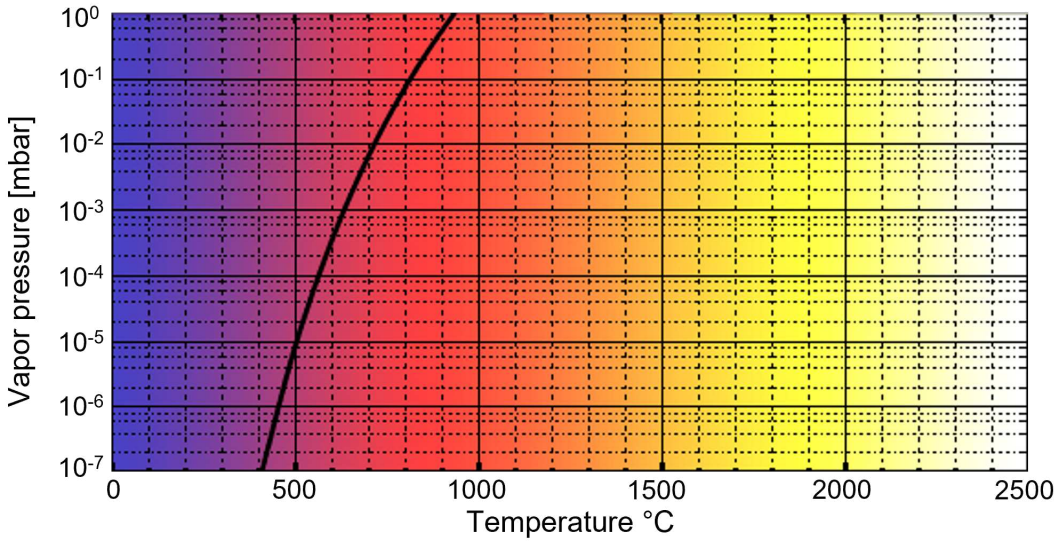

Figure 6.18: Vapor pressure of samarium [www.mbe-komponenten.de]

The first operation of the new TOF-MS will be performed with the photo-ionization of the samarium. Samarium is chosen as the first element because it has five stable isotopes ^{144}Sm, ^{149}Sm, ^{150}Sm, ^{152}Sm and ^{154}Sm, and a single

laser beam at 435.71 nm is sufficient to achieve photo-ionization via double photon absorption [73]. Time of flight signals of the samarium isotopes should give us a clear indication of the time resolution capabilities of the system.

The vapor pressure curve of the samarium is shown in Figure 6.18. It is clear that at the pressure range of 10^{-7} mbar, samarium must be available in the vapor phase upon heating the effusion cell to a temperature of 400°C or above. Powder form or small pieces of samarium will be placed inside the crucible of the effusion cell to obtain the atomic beam of the samarium.

Chapter 7

Conclusion and Outlook

The presented work discusses the principles and study of resonance laser photo-ionization of elements and their application in laser spectroscopy and laser ion sources.

Resonance photo-ionization of silver was performed with two different sources of atoms viz. an ablation plume and a hollow cathode lamp. In a hot environment like ablation plume where Doppler broadening is a major limitation to the resolution of the laser spectroscopy, it was shown that a Doppler-suppressed spectroscopy can be performed by choosing a tiny laser-atom interaction volume. A conventional approach is to provide orthogonal intersection of the laser beams, so that the Doppler-shifted atoms with respect to one laser beam is not Doppler-shifted with respect to the other laser beam. However, a Doppler-suppressed spectroscopy was achieved in this study with an angular separation as low as 8.5° (eight and a half degrees). In the scenario where the laser beams are injected collinearly, Doppler broadening is clearly observed. In this scenario, the effect of the linewidth of one resonant laser on the Doppler-broadened resonance profile of the other transition was studied. The fine structures of the level $4d^{10}6d\ ^2D$ (J=5/2 and J=3/2) were probed as well with a wide frequency scan. Qualitative comparison on the transition probabilities to these fine structure levels from the level $4d^{10}5p^2P^o_{3/2}$ was also performed.

The resonance spectroscopy of silver using a hollow cathode lamp provided very strong evidence of high-lying Rydberg states. These Rydberg states are found to be present around the energy value of 7.56 eV (60945.32 cm^{-1}). These levels are very close to the ionization potential of silver i,e. 7.58 eV (61106.45 cm^{-1}). These levels are planned to be re-visited in the future work to identify them using lasers of finer linewidths.

At Offline 2 ISOLDE, CERN, a thorough characterization of the SPES laser

ion source has been performed for the first time. The thermal and electrical properties of the source were analyzed and shown to be very stable. One of the most important features of a laser ion source is the chemical selectivity it can provide. It exploits the finger-print like electronic levels of each element and provides a very high purity ion beam which the surface ion sources or the plasma ion sources cannot provide. Through the study of the time structure of the extracted ion beams, a direct relation between the movement of the ions and the electrostatic axial field along the length of the ion source has been established. The laser enhancement of the ion yields in relation to the ion source temperature and the ion load has been investigated. At lower temperatures of the ion source, the laser enhancement ratio shows a higher value but decreases rapidly with increasing ion load in the ion source. At higher ion source temperature, the ratio maintains a relatively constant value up to a high ion load of 1.1 µA, which is explained by the excess thermionic electron emission at higher temperatures. The resonance laser ionization efficiency of 27.2% for gallium was also measured. Furthermore, it was also shown that the surface ionization efficiency value and the laser ionization efficiency are directly related to each other with the laser enhancement ratio.

Last but not the least, a new TOF-MS has been designed and assembled in the online laser lab at the SPES facility at INFN-LNL. High voltage test, vacuum test and calibration of the effusion cell have been performed. The system should aid in performing more scheme development for resonance photo-ionization of elements of interests for the SPES project. Several excitation laser entrance windows have been implemented in the reaction chamber to allow Doppler-free spectroscopy as well.

Appendix A

Laser enhancement ratios measured during the efficiency measurements

Table A.1: Measured laser enhancement ratios (LERs) during the efficiency measurements

No.	LERs	Mean LER
1	56.1	
2	48.8	
3	54.8	
4	61.5	
5	57.5	
6	55.2	
7	60.5	55.5 (4.5)
8	52.8	
9	57.5	
10	51.2	
11	47.7	
12	60.2	
13	61.4	
14	54.2	

Bibliography

[1] D Scarpa, E Mariotti, O S Khwairakpam, V Parenti, A Buono, P Nicolosi, M Calderolla, A Khanbekyan, M Ballan, L Centofante, S Corradetti, G Lilli, M Manzolaro, A Monetti, L Morselli, and A Andrighetto. New solid state laser system for SPES: Selective production of exotic species project at laboratori nazionali di legnaro. *Rev. Sci. Instrum.*, 93(8):083001, August 2022. https://doi.org/10.1063/5.0078913.

[2] Marco Durante and Katia Parodi. Radioactive beams in particle therapy: Past, present, and future. *Front. Phys.*, 8:00326, August 2020. https://doi.org/10.3389/fphy.2020.00326.

[3] Isao Tanihata. Nuclear physics with RIB's: How it all started. *Eur. Phys. J. Plus*, 131(4), April 2016. https://doi.org/10.1016/S0168-583X(96)01018-X.

[4] Faïrouz Hammache and Nicolas de Séréville. Transfer reactions as a tool in nuclear astrophysics. *Front. Phys.*, 8, March 2021. https://doi.org/10.3389/fphy.2020.602920.

[5] F Gramegna, P.V. Duppen, A Vitturi, and S Pirrone. Nuclear physics with stable and radioactive ion beams. *Ios Press, Inc., 2019*, 201, 2019.

[6] B. Marsh. Resonance ionization laser ion sources. *Proceedings of the CAS–CERN Accelerator School: Ion Sources, Senec, Slovakia, 29 May – 8 June 2012*, pages 203–254. http://dx.doi.org/10.5170/CERN-2013-007.

[7] Aligna system. https://tem-messtechnik.de/en/products/active-beam-stabilization/#overview. Accessed: 2023-03-11.

[8] M Manzolaro, F D'Agostini, A Monetti, and A Andrighetto. The SPES surface ionization source. *Rev. Sci. Instrum.*, 88(9):093302, September 2017. https://doi.org/10.1063/1.4998246.

[9] Y Jading, R Catherall, V N Fedoseyev, A Jokinen, O C Jonsson, T Kautzsch, I Klöckl, K-L Kratz, E Kugler, J Lettry, V I Mishin, H L Ravn, F Scheerer, O Tengblad, P Van Duppen, W B Walters, and A Wöhr. Production of radioactive ag ion beams with a chemically selective laser ion source. *Nucl. Instrum. Methods Phys. Res. B*, 126(1-4):76–80, April 1997. https://doi.org/10.1016/S0168-583X(96)01018-X.

[10] U Köster. Resonance ionization laser ion sources. *Nucl. Phys. A*, 701(1-4):441–451, April 2002. https://doi.org/10.1016/S0375-9474(01)01625-6.

[11] A Andrighetto, M Tosato, M Ballan, S Corradetti, F Borgna, V Di Marco, G Marzaro, and N Realdon. The ISOLPHARM project: ISOL-based production of radionuclides for medical applications. *J. Radioanal. Nucl. Chem.*, 322(1):73–77, October 2019. https://doi.org/10.1007/s10967-019-06698-0.

[12] Michele Ballan, Marianna Tosato, Marco Verona, Michele Caeran, Francesca Borgna, Elisa Vettorato, Stefano Corradetti, Lisa Zangrando, Massimo Sgaravatto, Marco Verlato, Mattia Asti, Giovanni Marzaro, Francesca Mastrotto, Valerio Di Marco, Devid Maniglio, Alessandra Bisio, Antonella Motta, Alberto Quaranta, Aldo Zenoni, Paolo Pastore, Nicola Realdon, and Alberto Andrighetto. Preliminary evaluation of the production of non-carrier added 111ag as core of a therapeutic radiopharmaceutical in the framework of ISOLPHARM_ag experiment. *Applied Radiation and Isotopes*, 164:109258, October 2020.

[13] Klaus D. A. Wendt et al. Laser based techniques for ultra trace isotope production, spectroscopy and detection. *Hyperfine Interactions*, 162:147–157, 2006. https://doi.org/10.1007/s10751-005-9219-8.

[14] Jim Al-Khalili and Ernst Roeckl, editors. *The euroschool lectures on physics with exotic beams, vol. II.* Lecture Notes in Physics. Springer, Berlin, Germany, 2006 edition, July 2006. http://dx.doi.org/10.1007/b11743651.

[15] Jim Al-Khalili and Ernst Roeckl, editors. *The euroschool lectures on physics with exotic beams, vol. II.* Lecture Notes in Physics. Springer, Berlin, Germany, 2006 edition, July 2006.

[16] É Ya Zandberg and N I Ionov. SURFACE IONIZATION. *Soviet Physics Uspekhi*, 2(2):255–281, February 1959.

[17] T. K. Sato, M. Asai, A. Borschevsky, T. Stora, N. Sato, Y. Kaneya, K. Tsukada, Ch. E. Düllmann, K. Eberhardt, E. Eliav, S. Ichikawa, U. Kaldor, J. V. Kratz, S. Miyashita, Y. Nagame, K. Ooe, A. Osa, D. Renisch, J. Runke, M. Schädel, P. Thörle-Pospiech, A. Toyoshima, and N. Trautmann. Measurement of the first ionization potential of lawrencium, element 103. *Nature*, 520(7546):209–211, April 2015.

[18] R Kirchner. On the thermoionization in hot cavities. *Nucl. Instrum. Methods Phys. Res. A*, 292(2):203–208, July 1990.

[19] Fabio Schwellnus, Klaus Blaum, Christopher Geppert, Tina Gottwald, Hans-Jürgen Kluge, Christoph Mattolat, Wilfried Nörtershäuser, Katja Wies, and Klaus Wendt. The laser ion source and trap (LIST) – a highly selective ion source. *Nucl. Instrum. Methods Phys. Res. B*, 266(19-20):4383–4386, October 2008. https://doi.org/10.1016/j.nimb.2008.05.065.

[20] M Manzolaro, A Andrighetto, G Meneghetti, A Monetti, D Scarpa, M Rossignoli, J Vasquez, S Corradetti, M Calderolla, and G Prete. Ongoing characterization of the forced electron beam induced arc discharge ion source for the selective production of exotic species facility. *Rev. Sci. Instrum.*, 85(2):02B918, February 2014. https://doi.org/10.1063/1.4857175.

[21] R. Kirchner. Ion sources for radioactive beams and related problems (review) (invited). *Review of Scientific Instruments*, 67(3):928–933, March 1996.

[22] Valentin Fedosseev, Katerina Chrysalidis, Thomas Day Goodacre, Bruce Marsh, Sebastian Rothe, Christoph Seiffert, and Klaus Wendt. Ion beam production and study of radioactive isotopes with the laser ion source at ISOLDE. *Journal of Physics G: Nuclear and Particle Physics*, 44(8):084006, July 2017.

[23] J. Lassen, R. Li, S. Raeder, X. Zhao, T. Dekker, H. Heggen, P. Kunz, C. D. P. Levy, M. Mostamand, A. Teigelhöfer, and F. Ames. Current developments with TRIUMF's titanium-sapphire laser based resonance ionization laser ion source. *Hyperfine Interactions*, 238(1), 2017.

[24] Vladilen Stepanovich Letokhov. *Laser Photoionization Spectroscopy*. Academic Press, San Diego, CA, March 1987. https://doi.org/10.1016/B978-0-12-444320-4.X5001-8.

[25] G. S. Hurst and M. G. Payne. *Principles and applications of resonance ionisation spectroscopy*. Adam Hilger, Bristol, 1988.

[26] S Rothe, T Day Goodacre, D V Fedorov, V N Fedosseev, B A Marsh, P L Molkanov, R E Rossel, M D Seliverstov, M Veinhard, and K D A Wendt. Laser ion beam production at CERN-ISOLDE: New features – more possibilities. *Nucl. Instrum. Methods Phys. Res. B*, 376:91–96, June 2016. https://doi.org/10.1016/j.nimb.2016.02.024.

[27] V N Fedosseev, Yu Kudryavtsev, and V I Mishin. Resonance laser ionization of atoms for nuclear physics. *Phys. Scr.*, 85(5):058104, May 2012. https://dx.doi.org/10.1088/0031-8949/85/05/058104.

[28] N Lecesne, R Alvès-Condé, E Coterreau, F De Oliveira, M Dubois, J L Flambard, H Franberg, T Gottwald, P Jardin, J Lassen, F Le Blanc, R Leroy, C Mattolat, A Olivier, J Y Pacquet, A Pichard, S Rothe, M G Saint-Laurent, and K Wendt. GISELE: a resonant ionization laser ion source for the production of radioactive ions at GANIL. *Rev. Sci. Instrum.*, 81(2):02A910, February 2010. https://doi.org/10.1063/1.3279301.

[29] V. N. Fedoseyev, F. Albus, R. Kirchner, O. Klepper, H. J. Kluge, V. I. Mishin, G. Passler, E. Roeckl, F. Scheerer, K. Schmidt, and N. Trautmann. Study of short-lived tin isotopes with a laser ion source. In *AIP Conference Proceedings*. AIP, 1995.

[30] G.D. Alkhazov, L.Kh. Batist, A.A. Bykov, V.D. Vitman, V.S. Letokhov, V.I. Mishin, V.N. Panteleyev, S.K. Sekatsky, and V.N. Fedoseyev. Application of a high efficiency selective laser ion source at the IRIS facility. *Nuclear Instruments and Methods in Physics Research Section A: Accelerators, Spectrometers, Detectors and Associated Equipment*, 306(1-2):400–402, August 1991.

[31] C Grüning, G Huber, P Klopp, J V Kratz, P Kunz, G Passler, N Trautmann, A Waldek, and K Wendt. Resonance ionization mass spectrometry for ultratrace analysis of plutonium with a new solid state laser system. *Int. J. Mass Spectrom.*, 235(2):171–178, July 2004. https://doi.org/10.1016/j.ijms.2004.04.013.

[32] I D Moore, A Nieminen, J Billowes, P Campbell, Ch Geppert, A Jokinen, T Kessler, B Marsh, H Penttilä, S Rinta-Antila, B Tordoff, K D A Wendt, and J Äystö. Development of a laser ion source at IGISOL. *J. Phys. G Nucl. Part. Phys.*, 31(10):S1499–S1502, October 2005. https://dx.doi.org/10.1088/0954-3899/31/10/020.

[33] Yu A Kudryavtsev, J Andrzejewski, N Bijnens, S Franchoo, M Huyse, A Piechaczek, J Szerypo, I Reusen, P Van Duppen, L Vermeeren, J Wauters, and A Wöhr. Laser ion source for the leuven isotope separator On-Line. *Rev. Sci. Instrum.*, 67(3):938–940, March 1996. https://doi.org/10.1063/1.1146778.

[34] T Sonoda, H Iimura, M Reponen, M Wada, I Katayama, V Sonnenschein, T Takamatsu, H Tomita, and T M Kojima. The laser and optical system for the RIBF-PALIS experiment. *Nucl. Instrum. Methods Phys. Res. A*, 877:118–123, January 2018. https://doi.org/10.1016/j.nima.2017.09.055.

[35] J Lassen, P Bricault, M Dombsky, J P Lavoie, Ch Geppert, and K Wendt. Resonant ionization laser ion source project at TRIUMF. In *Laser 2004*, pages 69–75. Springer-Verlag, 2006. https://doi.org/10.1007/3-540-30926-8_8.

[36] T F Gallagher, S A Edelstein, and R M Hill. Radiative lifetimes of the S and D Rydberg levels of Na. *Phys. Rev. A Gen. Phys.*, 11(5):1504–1506, May 1975. https://doi.org/10.1103/PhysRevA.11.1504.

[37] J J Olivero and R L Longbothum. Empirical fits to the voigt line width: A brief review. *Journal of Quantitative Spectroscopy and Radiative Transfer.*, 17(2):233–236, 1977.

[38] Wolfgang Demtröder. *Laser Spectroscopy*. Springer Berlin Heidelberg, 2003.

[39] F J Duarte and L W Hillman. Dye laser principles, with applications. 1990.

[40] P. F. Moulton. Spectroscopic and laser characteristics of ti:al2o3. *J. Opt. Soc. Am. B*, 3(1):125–133, Jan 1986.

[41] Nist. https://physics.nist.gov/PhysRefData/ASD/lines_form.html. Accessed: 2022-10-28.

[42] M Reponen, T Kessler, I D Moore, S Rothe, and J Äystö. A hot cavity laser ion source at IGISOL. *Eur. Phys. J. A*, 42(3), December 2009. https://doi.org/10.1140/epja/i2009-10830-6.

[43] Christopher Geppert. Laser systems for on-line laser ion sources. *Nucl. Instrum. Methods Phys. Res. B*, 266(19-20):4354–4361, October 2008. https://doi.org/10.1016/j.nimb.2008.05.036.

[44] V N Fedoseyev, The ISOLDE Collaboration, Y Jading, O C Jonsson, R Kirchner, K-L Kratz, M Krieg, E Kugler, J Lettry, T Mehren, V I Mishin, H L Ravn, T Rauscher, F Scheerer, O Tengblad, P Van Duppen, and A Wöhr. Study of short-lived silver isotopes with a laser ion source. *Z. Phys. Hadrons Nucl.*, 353(1):9–10, March 1995. https://doi.org/10.1007/BF01297718.

[45] Omorjit Singh Khwairakpam, Emilio Mariotti, Daniele Scarpa, Piergiorgio Nicolosi, Alen Khanbekyan, Salvatore Ferracane, Alberto Arzenton, and Alberto Andrighetto. Resonant laser ionization and fine-structure study of silver in an ablation plume. *Appl. Sci. (Basel)*, 13(1):309, December 2022. https://doi.org/10.3390/app13010309.

[46] U. Brackmann. *Lambdachrome® Laser Dyes*. Lambda Physik GmbH, 2000.

[47] D. Scarpa; et al. Tof diagnostic of tin resonant laser photoionization in spes laser offline laboratory. *JINST*, 11 C 09001, 2016. https://dx.doi.org/10.1088/1748-0221/11/09/C09001.

[48] Simion. https://simion.com/.

[49] R B Green, R A Keller, G G Luther, P K Schenck, and J C Travis. Galvanic detection of optical absorptions in a gas discharge. *Appl. Phys. Lett.*, 29(11):727–729, December 1976.

[50] J E M Goldsmith and J E Lawler. Optogalvanic spectroscopy. *Contemp. Phys.*, 22(2):235–248, March 1981.

[51] Beniamino Barbieri, Nicolò Beverini, and Antonio Sasso. Optogalvanic spectroscopy. *Rev. Mod. Phys.*, 62(3):603–644, July 1990.

[52] M N Reddy. Laser optogalvanic spectroscopy: Experimental details and potential applications in R and D. *Def. Sci. J.*, 44(4):279–293, January 1994.

[53] O.S. Khwairakpam, E. Mariotti, D. Scarpa, P. Nicolosi, A. Khanbekyan, A. Arzenton, S. Ferracane, and A. Andrighetto. Laser photo-ionization study of ^{nat}ag using opto-galvanic signal at SPES offline laser lab. *Journal of Instrumentation*, 17(12):C12009, December 2022.

[54] G D Alkhazov, V S Letokhov, V I Mishin, Panteleyev V N, V I Romanov, S K Sekatsky, and V N Fedoseyev. Highly effective z-selective photoionization of atoms in a hot metallic cavity followed by electrostatic confinement of the ions. *Pis'ma Zh. Techn. Fiz.*, 15(63):6, 1989.

[55] V.I. Mishin, V.N. Fedoseyev, H.-J. Kluge, V.S. Letokhov, H.L. Ravn, F. Scheerer, Y. Shirakabe, S. Sundell, and O. Tengblad. Chemically selective laser ion-source for the CERN-ISOLDE on-line mass separator facility. *Nuclear Instruments and Methods in Physics Research Section B: Beam Interactions with Materials and Atoms*, 73(4):550–560, April 1993.

[56] E. J. Prime, J. Lassen, T. Achtzehn, D. Albers, P. Bricault, T. Cocolios, M. Dombsky, F. Labrecque, J. P. Lavoie, M. R. Pearson, T. Stubbe, N. Lecesne, Ch. Geppert, and K. D. A. Wendt. TRIUMF resonant ionization laser ion source. *Hyperfine Interactions*, 171(1-3):127–134, 2006.

[57] Y. Liu, C.U. Jost, A.J. Mendez II, D.W. Stracener, C.L. Williams, C.J. Gross, R.K. Grzywacz, M. Madurga, K. Miernik, D. Miller, S. Padgett, S.V. Paulauskas, K.P. Rykaczewski, and M. Wolinska-Cichocka. On-line commissioning of the HRIBF resonant ionization laser ion source. *Nuclear Instruments and Methods in Physics Research Section B: Beam Interactions with Materials and Atoms*, 298:5–12, 2013.

[58] M Huyse. Ionization in a hot cavity. *Nucl. Instrum. Methods Phys. Res.*, 215(1-2):1–5, September 1983.

[59] F Schwellnus, R Catherall, B Crepieux, V N Fedosseev, B A Marsh, Ch Mattolat, M Menna, F K Österdahl, S Raeder, T Stora, and K Wendt. Study of low work function materials for hot cavity resonance ionization laser ion sources. *Nucl. Instrum. Methods Phys. Res. B*, 267(10):1856–1861, May 2009.

[60] H Kawano, T Takahashi, Y Tagashira, H Mine, and M Moriyama. Work function of refractory metals and its dependence upon working conditions. *Appl. Surf. Sci.*, 146(1-4):105–108, May 1999.

[61] M Manzolaro, F D'Agostini, A Monetti, and A Andrighetto. The SPES surface ionization source. *Rev. Sci. Instrum.*, 88(9):093302, September 2017.

[62] S. Warren, T. Giles, C.M. Pequeno, and A. Ringvall-Moberg. Offline 2, ISOLDE's target, laser and beams development facility. *Nuclear Instruments and Methods in Physics Research Section B: Beam Interactions with Materials and Atoms*, 463:115–118, January 2020.

[63] M. Au, C. Bernerd, Y. Nel Vila Gracia, M. Athanasakis-Kaklamanakis, J. Ballof, M. Bissell, K. Chrysalidis, R. Heinke, L. Le, R. Mancheva, B. Marsh, J. Rolewska, M. Schuett, T. Venenciano, S.G. Wilkins, Ch.E. Düllmann, and S. Rothe. Developments at CERN-ISOLDE's OFFLINE 2

mass separator facility for studies of molecular ion beams. *Nuclear Instruments and Methods in Physics Research Section B: Beam Interactions with Materials and Atoms*, 541:144–147, August 2023.

[64] Maximilian Schuett, Mia Au, Mark Bissell, Niels Bidault, Alexandros Koliatos, Line Le, Nikolay Azaryan, Reinhard Heinke, Katerina Chrysalidis, and Sebastian Rothe. Developments at the CERN-ISOLDE offline 2 mass separator. *Nuclear Instruments and Methods in Physics Research Section B: Beam Interactions with Materials and Atoms*, 541:82–85, August 2023.

[65] D. Stresau, K. Hunter, W. Sheils, P. Raffin, and Y. Benari. A new class of robust sub-nanosecond tof detectors with high dynamic range. *54th ASMS Conference on Mass Spectroscopy, Seattle, Washington*, 2006.

[66] V.N. Fedosseev, L.-E. Berg, N. Lebas, O.J. Launila, M. Lindroos, R. Losito, B.A. Marsh, F.K. Österdahl, T. Pauchard, G. Tranströmer, and J. Vannesjö. ISOLDE RILIS: New beams, new facilities. *Nuclear Instruments and Methods in Physics Research Section B: Beam Interactions with Materials and Atoms*, 266(19-20):4378–4382, October 2008.

[67] S Rothe, B A Marsh, C Mattolat, V N Fedosseev, and K Wendt. A complementary laser system for ISOLDE RILIS. *Journal of Physics: Conference Series*, 312(5):052020, September 2011.

[68] J. Lettry, R. Catherall, G. J. Focker, O. C. Jonsson, E. Kugler, H. Ravn, C. Tamburella, V. Fedoseyev, V. I. Mishin, G. Huber, V. Sebastian, M. Koizumi, and U. Köster and. Recent developments of the ISOLDE laser ion source. *Review of Scientific Instruments*, 69(2):761–763, February 1998.

[69] V. N. Fedoseyev, G. Huber, Ulli Köster, Jacques Lettry, V. I. Mishin, H. L. Ravn, and V. Sebastian. The isolde laser ion source for exotic nuclei. *Hyperfine Interactions*, 127:409–416, 2000.

[70] Y Liu, C Baktash, J R Beene, C C Havener, H F Krause, D R Schultz, D W Stracener, C R Vane, Ch Geppert, T Kessler, K Wies, and K Wendt. Time profiles of ions produced in a hot-cavity resonant ionization laser ion source. *Nucl. Instrum. Methods Phys. Res. B*, 269(23):2771–2780, December 2011.

[71] B. A. Marsh, L.-E. Berg, D. V. Fedorov, V. N. Fedosseev, O. J. Launila, M. Lindroos, R. Losito, F. K. Österdahl, T. Pauchard, I. T. Pohjalainen, U. Sassenberg, M. D. Seliverstov, A. M. Sjödin, and G. Tranströmer. The

ISOLDE RILIS pump laser upgrade and the LARIS laboratory. *Hyperfine Interactions*, 196(1-3):129–141, February 2010.

[72] https://tectra.de/analytics/microchannel-plates/. Accessed: 2023-08-07.

[73] Rilis database. http://riliselements.web.cern.ch/. Accessed: 2023-01-07.

Appendix B

List of publications

B.1 Journal Articles

1. *The SPES Laser Ion Source: Time Structure, Laser Enhancement and Efficiency Measurements with Gallium at ISOLDE Offline 2.* O.S. Khwairakpam et al., Preprint submitted to Nuclear Instr. and Methods in Physics Research Sec. B

2. *Nuclear physics midterm plan at Legnaro National Laboratories (LNL).* M. Ballan et al., The European Physical Journal Plus, 138 (8), 709 (2023). DOI: 10.1140/epjp/s13360-023-04249-x

3. *Low energy radioactive ion beams at SPES for nuclear physics and medical applications.* A. Andrighetto et al., NIMB: Beam Interactions with Materials and Atoms, 541, 236-239 (2023). DOI: 10.1016/j.nimb.2023.05.044

4. *Remote handling of radioactive targets at the SPES facility.* G. Lilli et al., Il Nuovo Cimento (2023). DOI: 10.1393/ncc/i2023-23032-y

5. *Resonant Laser Ionization and Fine-Structure Study of Silver in an Ablation Plume.* O.S. Khwairakpam et al., Appl. Sci. 13(1), 309 (2023). DOI: 10.3390/app13010309

6. *New solid state laser system for SPES: Selective Production of Exotic Species project at Laboratori Nazionali di Legnaro.* D. Scarpa et al., Rev. Sci. Instrum. 93, 083001 (2022). DOI: 10.1063/5.0078913

B.2 Conference Proceedings

1. *The SPES Laser Ion Source: Time Structure and Laser Enhancement Measurements with Sm^+ beam.* O.S. Khwairakpam et al., Submitted to IOP Journal of Physics: Conference Series (JPCS)

2. *Benchmark evaluation of a single frequency continuous wave OPO seeded pulsed dye amplifier for high-resolution laser spectroscopy.* M. Urquiza-González et al., Proc. SPIE 12399 (2023). DOI: 10.1117/12.2646665

3. *Laser Photo-ionization study of ^{nat}Ag using Opto-galvanic signal at SPES offline laser lab.* O.S. Khwairakpam et al., JINST 17 C12009 (2022). DOI: 10.1088/1748-0221/17/12/C12009

4. *A new production method of high specific activity radionuclides towards innovative radiopharmaceuticals: The Isolpharm Project.* E. Vettorato et al., RAD Conf. Proc. 6, 1–4 (2022). DOI: 10.21175/RadProc.2022.02